

UNIVERSIDADE FEDERAL DE SANTA CATARINA
DEPARTAMENTO DE ENGENHARIA DE PRODUÇÃO E SISTEMAS
PROGRAMA DE PÓS-GRADUAÇÃO EM ENGENHARIA DE PRODUÇÃO

*Computer Generation and Application of 3-D
Reconstructed Porous Structure: From 2-D
Images to the Prediction of Permeability*

A Thesis Submitted to Federal University of Santa Catarina
in Partial Fulfillment of the Requirements for the Degree of
Doctor in Production Engineering

LIANG Zhirong

Florianópolis, SC

August, 1997

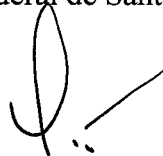
Computer Generation and Application of 3-D Reconstructed Porous Structure: From 2-D Images to the Prediction of Permeability

Liang Zhirong

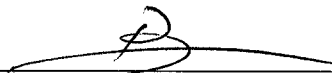
Esta tese foi julgada adequada para a obtenção do título de

Doutor em Engenharia de Produção

e aprovada em sua forma final pelo Programa de Pós-Graduação em Engenharia de Produção da Universidade Federal de Santa Catarina.



Prof. Paulo Cesar Philippi, Dr. Ing.
Orientador

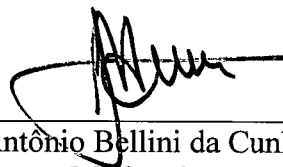


Prof. Ricardo Miranda Barcia, Ph.D.
Coordenador do Programa

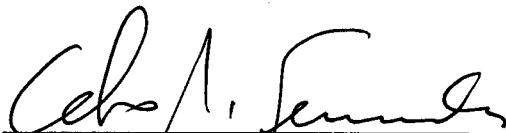
Banca Examinadora:



Prof. Paulo Cesar Philippi, Dr. Ing.
Orientador



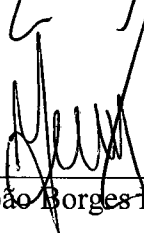
Prof. José Antônio Bellini da Cunha Neto, Dr.
Moderador



Eng. Celso Peres Fernandes, Dr.



Prof. Jean-François Dañan, Docteur d'Etat
Examinador Externo



Prof. João Borges Laurindo, Dr.



Eng. Régis Kruef Romeu, Dr.
Examinador Externo

Florianópolis, 15 de agosto de 1995

To my wife

Guo Qinghui

and

To my daughter

Lu

To my parents

Liang Chengfang and Wei Fengying

ACKNOWLEDGEMENTS

To Prof. Dr. Paulo Cesar Philippi, for all his generous guidance, support and friendship.

To Dr. Celso Peres Fernandes, Dr. Fabio Santana Magnani and Dr. Nathan Mendes, for their interesting and stimulating discussions and friendship.

To Dr. Jean-Paul Laurent and Prof. Dr. Jean-Francois Daïan, from Laboratoire D'Etude des Transferts En Hydrologie et Environnement, Grenoble, France, for the participation of my qualification examination and defense, respectively, and useful suggestions.

To Dr. Régis Krueel Romeu, from CENPES/PETROBRAS, for his participation of my defense and useful suggestions.

To Prof. Dr. José Antônio Bellini da Cunha Neto, Prof. Dr. João Borges Laurindo and Dr. Celso Peres Fernandes, for their participation of my defense and useful suggestions.

To CAPES (Coordenação de Aperfeiçoamento do Pessoal de Nível Superior), for financial support during my study.

To PPGEP/UFSC (Programa de Pós-Graduação em Engenharia de Produção) and LMPT/UFSC (Laboratório de Meios Porosos e Propriedades Termofísicas de Materiais), for all supports during my study.

To CENPES/PETROBRAS (Centro de Pesquisas e Desenvolvimento Leopoldo A. Miguez de Mello), for providing the images of Berea sandstone and mercury intrusion curves.

To all my colleagues of LMPT, especially to Prof. Dr. José Antônio Bellini da Cunha Neto, Prof. Dr. Vicente de Paulo Nicolau, Dr. Saulo Güths, Aldomar Pedrini, André Duarte Bueno, Romeu André Pieritz, Thomas Tschoepke Soares, Roberto Gaiser, Claudia Lavina Martins, Luís Orlando Emerich dos Santos, Anastacio da Silva Jr. and Rogério Vilain, for their help and friendship.

LIST OF CONTENTS

LIST OF FIGURES	ix
LIST OF TABLES	xiv
NOMENCLATURE	xvi
RESUMO	xviii
ABSTRACT	xix
1. INTRODUCTION	1
1.1. Problems Involving Porous Media.....	1
1.2. General Reviews	2
1.3. Outline of This Work	7
2. IMAGE ANALYSIS TECHNIQUES FOR CHARACTERIZATION OF POROUS STRUCTURE	10
2.1. Introduction	10
2.2. Image Acquisition and Segmentation	11
2.3. Fourier Transform and Its Properties.....	13
2.4. Characterization of 2-D Thin Sections of Porous Media.....	18
2.5. Skeleton of 2-D Porous Media	23
2.5.1. A 2-D Thinning Algorithm	24
2.5.2. A 2-D Skeletonizing Algorithm	25
3. RECONSTRUCTION OF 3-D POROUS MEDIA	30
3.1. Introduction	30
3.2. General Concepts.....	31
3.3. JQA Method.....	32

3.3.1. Linear Filter	32
3.3.2. Nonlinear Filter	33
3.4. New Method Based on Fourier Transform	35
3.4.1. Principle	35
3.4.2. Reconstruction Process of 3-D Porous Media	36
3.5. Examples and Discussions	42
3.5.1. Comparison of the Results with JQA Method.....	44
3.5.2. Effects of Reconstruction Parameters on the Results.....	45
3.5.3. Effects of Phase Angle on the Results.....	49
4. VISUALIZATION AND CHARACTERIZATION OF 3-D POROUS STRUCTURE	52
4.1. Introduction	52
4.2. Visualization of the 3-D Porous Structure	53
4.3. The Skeleton of 3-D Object.....	58
4.3.1. Basic Concepts for 3-D Discrete Topology.....	58
4.3.2. Thinning Algorithm	59
4.3.3. Examples	62
4.4. Graph of 3-D Porous Structure (Skeleton).....	65
4.5. "Pore Size" Distribution and Hydraulic Radius.....	66
5. SIMULATION OF PERMEABILITY IN 3-D POROUS MEDIA	70
5.1. Introduction	70
5.2. Review on Simulation of Permeability.....	71
5.2.1. Deterministic Permeability Model.....	72
5.2.2. Network Permeability Model.....	74
5.2.3. Empirical permeability model	77
5.3. Prediction of Absolute Permeability	78
5.4. Example.....	81
6. RESULTS AND DISCUSSIONS	84
6.1. Introduction	84

6.2. Description of Whole Process to Predict Permeability	85
6.2.1. Sample Selection and Analysis.....	85
6.2.2. Reconstruction of 3-D Porous Structure for Berea Sandstone	87
6.2.3. Prediction of Permeability.....	98
6.3. Results for More Samples	103
6.4. Discussions.....	121
6.4.1. Permeability as Function of Porosity and Autocorrelation Function .	121
6.4.2. Graph of Pore Structure.....	123
6.4.3. Comparison of Permeability with Empirical Correlations	124
7. CONCLUSIONS	128
7.1. Conclusions	128
7.2. Future Works.....	130
APPENDIX A	131
APPENDIX B	133
APPENDIX C	137
REFERENCES	144

LIST OF FIGURES

Figure 1.1	Process for predicting absolute permeability in porous media.	8
Figure 2.1	Schematic procedures of image production methodology.	12
Figure 2.2	Digital image of a thin section of a 500 mD Berea sandstone.	14
Figure 2.3	Binary image from the image of Figure 2.2.	14
Figure 2.4	Size effect on the power spectrum.	16
Figure 2.5	Shape affect on power spectrum.	17
Figure 2.6	Autocorrelation functions in two directions and their average for Figure 2.3.	20
Figure 2.7	Surface display of power spectrum for Figure 2.3.	21
Figure 2.8	Gray level representation of the power spectrum for the porous section presented in Figure 2.3.	21
Figure 2.9	Surface display of 2-D autocorrelation function for the porous section shown in Figure 2.3.	22
Figure 2.10	Illustrations for obtaining the isotropic autocorrelation function from discrete values for a particular image.	22
Figure 2.11	Comparison of autocorrelation function.	23
Figure 2.12	The eight neighbors of a pixel p.	24
Figure 2.13	A pixel p with $N(p)=4$ and $s(p)=3$	25
Figure 2.14	The result of thinning algorithm.	26
Figure 2.15	Bold labels satisfy one among three conditions.	28
Figure 2.16	The result of skeletonizing algorithm.	29

Figure 3.1	Comparison of R_Z as a function of R_Y between numerical and analytical values at $\epsilon=0.5$	37
Figure 3.2	Arrangement of the complex Fourier coefficients in 2-D.....	39
Figure 3.3	Arrangement of the complex Fourier coefficients in 3-D.....	41
Figure 3.4	A plane section of the Fontainebleau Sandstone GF2.....	42
Figure 3.5	Experimental $R_Z(u)$	43
Figure 3.6	A reconstructed cross section for GF2 sample.....	43
Figure 3.7	Comparison of $C_Z(u)$ between this work and Adler et al. (1990).	45
Figure 3.8	Effects of n and ζ on autocorrelation functions	47
Figure 3.9	Effects of N on autocorrelation function.....	48
Figure 3.10	Comparison of normalized autocovariance function for different seeds.	50
Figure 3.11	Cross sections generated by different phase angle distributions.....	50
Figure 4.1	Isosurface of a reconstructed porous medium for sample GF2.....	55
Figure 4.2	Isosurface of a reconstructed porous medium in Figure 4.1 rotated 60 degrees.....	55
Figure 4.3	Slice display of a reconstructed porous medium in Figure 4.1 by three orthogonal direction.	56
Figure 4.4	Cutout display of a reconstructed porous medium in Figure 4.1	56
Figure 4.5	Block display of a reconstructed porous medium in Figure 4.1.....	57
Figure 4.6	Oblique slice display of a reconstructed porous medium in Figure 4.1 by any direction.....	57
Figure 4.7	6-adjacent, diagonally adjacent and diametrically adjacent paths.	58
Figure 4.8	The x-, y- and z-axis, and the arrangement of each orientation.....	60
Figure 4.9	Three deleting templates of the parallel thinning algorithm.	61
Figure 4.10	Thinning of a simple object.....	63
Figure 4.11	Another example.	64

Figure 4.12	Skeleton of the reconstructed porous structure in Figure 4.1 for sample GF2.....	65
Figure 4.13	A 3-D irregular shape.....	68
Figure 4.14	Normal planes at two points of Figure 4.13.....	68
Figure 4.15	Skeleton and its normal plane of Figure 4.10.....	69
Figure 5.1	A piece of a pore space-solid interface.....	73
Figure 5.2	Semi-regular network model of a 2-D porous medium.....	74
Figure 5.3	Schematic sequence of operations in analyzing permeability.....	76
Figure 5.4	Construction for calculating the permeability of a random network.....	76
Figure 5.5	Bundle of uniform capillary tubes model of identical diameter for the periodically constricted tube model.....	78
Figure 5.6	The 2-D graph representation of pore space (skeleton).....	79
Figure 5.7	A graph of 3-D Fontainebleau sandstone skeleton.....	82
Figure 6.1	Two half segments of Figure 2.3.....	85
Figure 6.2	Comparison of normalized autocovariance function for Berea 320220.....	86
Figure 6.3	The autocorrelation function of Berea 320220.....	87
Figure 6.4	Pore size distribution function for sample Berea 320220.....	88
Figure 6.5	Normalized autocovariance function $R_Z(u)$ and the corresponding $R_Y(u)$	88
Figure 6.6	Normalized autocovariance function of Berea 320220 for different n	89
Figure 6.7	Normalized autocovariance function of Berea 320220 for different N	90
Figure 6.8	Normalized autocovariance function of Berea 320220 for different realizations.....	91
Figure 6.9	Comparison of autocorrelation function between the sample and the reconstructed porous structure.....	92
Figure 6.10	A sample reconstruction of porous structure.....	93
Figure 6.11	Isosurface of 3-D pore structure after removal of isolated solids.....	94

Figure 6.12	Comparison of autocorrelation function between reconstructed and after removal of isolated components.....	94
Figure 6.13	A cutout display of the reconstructed porous structure in Figure 6.11.	95
Figure 6.14	An oblique slice display of the reconstructed porous structure in Figure 6.11.....	95
Figure 6.15	A block display of the reconstructed porous structure in Figure 6.11.	96
Figure 6.16	Comparison of pore size distribution function between the sample and the 2-D cross sections of reconstructed porous structure.....	96
Figure 6.17	Pore size distribution for 3-D reconstructed porous structure of Berea 320220.....	97
Figure 6.18	Graph of the reconstructed porous structure for Berea 320220 in Figure 6.11.....	97
Figure 6.19	Slice display in three direction of Figure 6.18.	98
Figure 6.20	Simulation of fluid flow on the graph of pore space in a porous structure.....	99
Figure 6.21	Digital image of a plane section of 200 mD Berea sandstone and its binary image.	105
Figure 6.22	Digital image of a plane section of 500 mD Berea sandstone and its binary image.	106
Figure 6.23	Digital image of a plane section of 500 mD Berea sandstone and its binary image.	107
Figure 6.24	Digital image of a plane section of 500 mD Berea sandstone and its binary image.	108
Figure 6.25	Power spectrum of Figure 6.21 (b).....	109
Figure 6.26	Power spectrum of Figure 6.22 (b).....	109
Figure 6.27	Power spectrum of Figure 6.23 (b).....	110
Figure 6.28	Power spectrum of Figure 6.24 (b).....	110
Figure 6.29	Normalized autocovariance function for all samples.....	113
Figure 6.30	Pore size distribution function for all samples.....	113

Figure 6.31	Comparison of autocorrelation functions between reconstructed porous structures and samples: (a) Berea 26 (b) Berea 310259 (c) Berea 318238 (d) Berea 32216.....	115
Figure 6.32	The reconstructed porous structures for four samples: (a) Berea 26 (b) Berea 310259 (c) Berea 318238 (d) Berea 32216.....	117
Figure 6.33	3-D graph of pore space for reconstructed porous structures for four samples: (a) Berea 26 (b) Berea 310259 (c) Berea 318238 (d) Berea 32216. ...	119
Figure 6.34	A display of the final stage of thinning in 2-D case.....	124
Figure 6.35	Capillary pressure of mercury intrusion for 200 mD and 500 mD Berea sandstones.....	125
Figure 6.36	Distribution of pore diameters for 200 mD and 500 mD Berea sandstones.	125
Figure B.1	Right-handed coordinate system and positive rotations about the coordinate axes.....	133
Figure C.1	Procedure of calculating of porosity and correlation function from 2-D images.....	138
Figure C.2	Procedure of reconstruction of 3-D pore structure.....	139
Figure C.3	Procedure of skeletonization.....	140
Figure C.4	Procedure of classification of skeleton.....	142
Figure C.5	Procedure of predicting permeability.....	143

LIST OF TABLES

Table 3.1	Statistical properties of reconstructed porous media and comparison with results of Adler et al.	44
Table 3.2	Effects of n and ζ on porosity	47
Table 3.3	Effects of N on porosity	48
Table 3.4	Effects of random generator on the results.....	49
Table 5.1	Results of predicted permeability.....	82
Table 5.2	Comparison of predicted permeability in three directions.	83
Table 5.3	Comparison of predicted permeability with experimental and Adler et al.'s results.	83
Table 6.1	Effects of n on porosity	89
Table 6.2	Effects of N on porosity	90
Table 6.3	Effects of random generator on porosity.....	91
Table 6.4	Comparison of predicted permeability in three directions for 500mD Berea sandstone 320220.	99
Table 6.5	Numerical results of prediction of permeability for Berea 320220.....	101
Table 6.6	Effects of n on permeability for Berea 320220.	102
Table 6.7	Effects of ζ on permeability for Berea 320220	102
Table 6.8	Effects of N on prediction of permeability for Berea 320220.....	103
Table 6.9	Effects of different configurations on permeability for Berea 320220	103
Table 6.10	Porosity ε and porosity of half image ε_h for all samples.....	104
Table 6.11	Normalized autocovariance function for all samples.....	111

Table 6.12	Comparison of porosity ϵ of reconstructed porous structures for all samples with the original.....	114
Table 6.13	Numerical results when predicting permeability for 200mD and 500 mD Berea sandstone samples.....	121
Table 6.14	Relation of permeability with porosity and correlation length.	122
Table 6.15	Comparison of the result for 200 mD Berea sandstone with empirical permeability correlation.	126
Table 6.16	Comparison of the result for 500 mD Berea sandstone with empirical permeability correlation	126
Table B.1	Summary of rotation matrices about the three coordination axes.....	134
Table B.2	Reflection matrices.....	135

NOMENCLATURE

A	normal cross-sectional area, L^2, m^2
B_m	coefficient in Eq. (3.20)
$C(\mathbf{u})$	autocorrelation function
D	diameter, L, m
D_b	breakthrough diameter, L, m
d	distance
d_H	hydraulic diameter, L, m
\hat{f}_i	imaginary component of Fourier transform
\hat{f}_r	real component of Fourier transform
f_x, f_y	frequency variables
g	hydraulic conductance, $L^4/t/m, m^4/s/kg$
H_m	Hermite polynomial
K	permeability, L^2, mD
L	length, L, m
N	reconstructed parameter
n	reconstructed parameter
P	pressure, $m/Lt^2, Pa$
P_{cb}	breakthrough capillary pressure, $m/Lt^2, Pa$
$P(y)$	standard normal density function
Q	volumetric flow rate, $L^3/t, m^3/s$
R	radius, L, m
R_Z, R_Y	normalized autocovariance function
X	non-correlated Gaussian field
Y	correlated Gaussian field
Z	phase function

r_H	hydraulic radius, L, m
r_m	radius of curvature, L, m
v	velocity, L/t, m/s

Greek Letters

α	length per pixel, L, μm
β	relaxation parameter
ε	porosity
Φ	phase angle
λ	correlation length, L, μm
μ	viscosity, m/Lt, Ns/m^2
θ	contact angle
σ	interfacial tension, $\text{m/L}^2\text{t}^2$, N/m
ζ	reconstructed parameter

Other symbols

\mathfrak{F}	Fourier transform
\wp	power spectrum

Subscripts

c	capillary
i	node i
j	node j
L	link

RESUMO

GERAÇÃO EM COMPUTADOR E APLICAÇÃO DE ESTRUTURAS POROSAS 3-D RECONSTRUÍDAS: DE IMAGENS 2-D À PREVISÃO DE PERMEABILIDADE

Várias técnicas de análise de imagem e reconhecimento de padrões, tal como teoria de processos estocásticos, transformada de Fourier, morfologia matemática e esqueleto, são aplicadas para simulações sobre meios porosos 3-D, no presente trabalho. O método da Gaussiana truncada, usando a transformada de Fourier, é proposto para gerar a estrutura porosa 3-D a partir de imagens 2-D de amostras. Esta estrutura gerada, possui a mesma porosidade e função de autocorrelação da amostra real em estudo. O gráfico do espaço poroso 3-D (esqueleto) proporciona um meio de visualização da rede porosa e dá informações tanto visuais como quantitativas sobre a conectividade do espaço poroso, o número de coordenação para cada nó e raio hidráulico local. O esqueleto é extraído usando um algoritmo que conserva a conectividade, i.e., o esqueleto e a estrutura original de poros têm a mesma topologia. Uma vez obtido o esqueleto, a simulação do escoamento de fluido é executado diretamente sobre este. Designa-se uma resistência hidráulica a cada ligação, e calcula-se uma pressão para cada nó. Calcula-se o fluxo total volumétrico pela rede e então a permeabilidade absoluta está determinada para o esqueleto. A permeabilidade predita para arenitos Berea está em bom acordo com o valor experimental e as correlações empíricas.

Palavras Chaves: Análise de imagem, meios porosos, permeabilidade

ABSTRACT

Various techniques of image analysis and pattern recognition, such as stochastic theory, Fourier transform, mathematical morphology and thinning, etc., are applied to simulate 3-D porous media in the present work. The truncated Gaussian method using Fourier transform is proposed to generate the 3-D porous structure from 2-D images of pore casts. It possesses the same porosity and autocorrelation function as the real sample in study. The graph of 3-D pore space (skeleton) provides a way of visualizing the pore network. It is extracted using a thinning algorithm, which preserves connectivity, i.e., this network and original pore structure have the same topology. It gives both visual and quantitative information about the connectivity of pore space, the coordination numbers for every node and local hydraulic radius. Once the network of pore structure is obtained, fluid flow simulation is performed directly on it. Resistance to flow is calculated for each link. A fluid pressure is calculated at each node, and total volumetric flux through the network is computed. Then the absolute permeability is estimated from the corresponding network. The predicted permeability for Berea sandstone rocks is in good agreement with the experimental value and empirical correlation.

Keywords: Image analysis, porous media, permeability

1. INTRODUCTION

1.1. PROBLEMS INVOLVING POROUS MEDIA

Flow and transport processes in porous media arise in many diverse fields of science and engineering, ranging from agricultural, biomedical, civil, ceramic, chemical, and petroleum engineering to food and soil sciences and powder metallurgy (Dullien, 1992; Sahimi, 1993). For example, classical research areas of chemical engineering concerned with porous media include filtration, drying and multiphase flow in packed beds. In petroleum industry, often only a relatively small fraction of oil in a reservoir can be recovered with traditional recovery techniques. The most common method of enhancing oil recovery is the injection of water at strategic location to displace the oil toward the production wells.

In all these phenomena one has to deal with the complex pore structure of the medium and how it affects the distribution, flow, or displacement, or dispersion (i.e., mixing) of one fluid in another. Each process can, in itself, be very complex. For example, displacement of one fluid by another can be carried out by many different mechanisms, which may involve heat and mass transfer, thermodynamic phase behavior and phase change, and the interaction of various forces such as viscous, buoyancy and capillary forces. If the solid matrix of the porous media is deformable, its porous structure may change during flow or any other phenomena. If the fluid is reactive, or if it carries solid particles of various shapes, sizes and electrical charges, the pore structure of the medium may change due to the reaction of the fluids with the pore surface, or the physicochemical interaction between the particles and the pore surface. Almost all studies of flow, dispersion, and displacement process in porous media are motivated by one question. How are the effective macroscopic transport parameters influenced by the microscopic geometric structure of the medium? Therefore, a quantitative geometric characterization of the complex porous microstructure and calculation of effective macroscopic transport properties from the geometric characterization and the equations of

motion for the phenomenon of interest are two important aspects in the study of porous media.

Sedimentary rocks can be treated as porous media. The existence of a high permeable void or pore space distinguishes reservoir rocks from other rocks. The structure and geometry of the pore space and its complementary solid matrix determine several macroscopic properties of the rocks such as absolute and relative permeability, capillary pressure and formation factor. A quantitative description of the structure and geometry of the pore space is therefore an important part of reservoir characterization. The problem of predicting macroscopic rock properties from the underlying microscopic structure and pore-scale physics has been the subject of extensive investigation.

In section 1.2, we review the recent works on the two important aspects in the study of porous media: geometric characterization of the complex porous microstructure and calculation of fluid permeability from it. Then an outline of this work is given in section 1.3.

1.2. GENERAL REVIEWS

At least two levels of description can be distinguished in the analysis of the various phenomena: microscopic and macroscopic. The microscopic level corresponds to the knowledge of the value of the fields at every point. The macroscopic level for this class of media is obtained by averaging the relevant microscopic fields over a sufficiently large sample. Engineers are usually interested in this macroscopic level. For example, in flow problems, the permeability relates the volumetric flow rate to the macroscopic pressure drop.

Two classes of disordered porous media are usually considered: homogeneous porous media and heterogeneous porous media. In the first class are porous media that are microscopically disordered but macroscopically homogeneous. Provided that they are large enough, such porous media are characterized by well-defined and unique pore-space properties, such as porosity and pore-size distribution, and size-independent transport properties such as diffusivity, conductivity, and permeability. Porous media which are macroscopically heterogeneous, in the sense that there are large-scale spatial variations in their properties when one samples different regions of their pore space, are in the second class. For the sake of simplicity, this work is restricted to homogeneous porous media.

Sahimi (1993) classified the models for flow, dispersion and displacement process in the porous media as continuum models and discrete models. Continuum models represent the classical engineering approach to describing materials of complex and irregular geometry, characterized by several length scales. The physical laws that govern fluid transport are well understood at the microscopic level. One could write down differential equations for momentum, mass and heat, and the associated initial and boundary conditions at the fluid solid interface. However, as the interface in real porous media is very irregular, practical and economical techniques are not available for solving such boundary value problems. Past theoretical attempts to derive macroscopic transport coefficients from the microstructure of porous media entailed a simplified representation of the pore space, often as a bundle of capillary tubes. These models have been widely applied because of their convenience and familiarity to the engineers. But they do have some limitations. For example, they are not well suited for describing effect of the pore space inter-connectivity and long range correlation in the system.

The discrete models are free of these limitations. These models have been advanced to describe phenomena at the microscopic level and extended to describe various phenomena at the macroscopic level. These discrete models are mostly based on a network representation of the porous media in which larger pores (pore bodies) are connected by narrower pores (pore throats). Network models represent the most important and widely used class of geometric models for porous media (Hilfer, 1996). They are not only used in theoretical calculations but also in the form of micromodels in experimental observations. A network is a graph consisting of a set of nodes or sites connected by a set of links or bonds. The nodes of the network could for example represent the centers of pore bodies. The links represent connections between them. The nodes can be chosen deterministically as for the sites of a regular lattice or randomly as in the realization of a Poisson or other stochastic point process. Similarly, the links connecting different nodes may be chosen according to some deterministic or random procedure. Finally the nodes are dressed with convex sets such as spheres representing pore bodies, and the links are dressed with tubes providing a connecting path between the pore bodies. A simple ordered network model consists of a regular lattice with spheres of equal radius centered at its nodes that are connected through cylindrical tubes of equal diameter. Very often the diameters of spheres and tubes in a regular network model are chosen at random. The original idea of network of a pore space is rather old, but it was only in the early 80s that systematic and rigorous procedures were developed to map, in principle,

any disordered rock onto an equivalent random network of bonds and site. Once this mapping is complete one can study a given phenomena in porous media in great details (Sahimi, 1993). Dullien (1992) reviewed the details of various pore-scale processes, including detailed descriptions of many aspects of network models. The most important features of pore network geometry and topology that affect fluid distribution and flow in reservoir rocks are the pore throat and pore body size distributions, the pore body-to-pore throat size aspect ratio and the pore body coordination number (Ioannidis and Chatzis, 1993). These data have been tentatively assumed in the previous works. The extension of these techniques to real porous media has been complicated by the difficulty in describing the complex 3-D pore structure of real porous rocks. Information about the pore structure of reservoir rocks is often obtained from mercury intrusion, sorption isotherm and image analysis of thin section images. Mercury intrusion and sorption isotherm data provide statistical information about the pore throat size distribution. Or more correctly, the distribution of the volumes that may be invaded within specified pore throat sizes. Advanced techniques such as micro-computed tomography (Hazlett, 1995) and serial sectioning (Koplik *et al.*, 1984; Kwiecien *et al.*, 1990) do provide a detailed description of the 3-D pore structures of rocks. These techniques are, however, expensive and not readily available.

Recently, image analysis methods used over pictures of highly polished surfaces of porous materials, taken with an electron scanning microscope or optical microscope, have been used to describe the porous structure, to obtain equivalent lattice models of real porous structure, to analyze transport phenomena on these models, and to predict the transport coefficients (e.g. Adler *et al.*, 1990; Philippi *et al.*, 1994; Philippi and Souza, 1995). Opening (2-D and 3-D) and median line graphics (2-D) techniques were developed by Pieritz (1994), Fernandes (1994) and Magnani (1996). One of the most interesting results of image analysis in the study of porous media is the reconstruction of porous media, which involves the generation of 3-D porous structure possessing the same statistical properties as the real porous structure under study. The general objective of reconstructed porous media is to mimic more closely the geometry of real media. This reconstruction process is attractive for a number of reasons. The most important is the versatility of the process since it allows the combination of many different structures. The other advantage is that the method enables us to create numerical samples with the desired properties. The various field equations can be numerically solved, and the macroscopic tensors characteristic of the media can be calculated. The principle of this method is composed of three major steps. The first involves the measurement

of any salient geometric features. Different features can be chosen for various materials. Usually the porosity and autocorrelation function of the pore space are measured for homogeneous porous media. The second step is the reconstruction process. Random samples of porous media are generated in such a way that, on average, they possess the same statistical properties as the real samples in study. Once these samples are generated, in the third step, all transports can be studied at least in principle. Generally, the macroscopic quantity of interest is obtained by a spatial integration of the local field. For instance, the determination of permeability necessitates the resolution of the Stokes equations of motion and the spatial integration of the velocity field. Adler *et al.* (1990) used the method that consists of the full resolution of the field equations inside the reconstructed sample with adequate boundary conditions. The method is statistical in character, and samples of porous media are generated at will. The permeability of each sample is determined and averaged over a large number of samples. This method has been applied to previously the prediction of important petrophysical and reservoir engineering properties, such as permeability (Adler *et al.*, 1990; Bentz and Martys, 1994) and formation factor (Ioannidis *et al.*, 1995) with reasonable success. Joshi (1974), Quiblier (1984), Adler *et al.* (1990) and Fernandes (1994) have extensively studied the reconstruction operation (here we refer to it as JQA method). A random and discrete field $Z(\mathbf{x})$ is devised from a non-correlated Gaussian field $X(\mathbf{x})$ in two steps: a linear filter $X(\mathbf{x}) \rightarrow Y(\mathbf{x})$ and a nonlinear filter $Y(\mathbf{x}) \rightarrow Z(\mathbf{x})$. Here $Y(\mathbf{x})$ is a correlated Gaussian field. By assuming isotropy, 3-D pore structure can thus be constructed from 2-D porous sections, conserving porosity and autocorrelation function. An alternative way to carry out linear filter is to generate $Y(\mathbf{x})$ using Fourier transform (Adler, 1992). From a computational point of view, the use of the fast Fourier transform algorithm, instead of laborious solution of nonlinear equation, makes the Fourier transform superior to the JQA method. However, application of the Fourier transform method in 3-D is restricted by resident memory requirements of computers. Ioannidis *et al.* (1995) combined the two above methods to generate porous media of larger sizes, for example, up to 400^3 voxels on a typical engineering workstation. Furthermore, Yao *et al.* (1993) compared the moments of order larger than two of the phase function for real and reconstructed porous media. For a Vosges sandstone 3-D sample, it is shown that these high-order moments (up to fourth order) are very close in the real and in the reconstructed materials.

Other authors used thin sections to determine characteristic geometric quantities. Lin and Cohen (1982) and Koplik *et al.* (1984) used serial sections of the medium to determine an

equivalent capillary network. Koplik *et al.* (1984) used effective-medium theory to calculate the permeability and conductivity of the equivalent network obtained from image analysis. Berryman and Blair (1986) used image processing techniques to obtain two-point spatial correlation functions. The porosity and specific surface area may be estimated directly from measured two-point spatial correlation functions. The measured values of porosity and image specific surface were combined with known values of electrical formation factors to estimate fluid permeability using one version of the Kozeny-Carman empirical relation. Thovert *et al.* (1993) proposed various algorithms, based on pseudo-diffusion processes, to determine the connected and percolation components of the pore space. The graph of the pore space was obtained by two different methods; the most efficient is based on homotopic thinning. The topological characteristics, such as the number of loops, were derived. Systematic applications of these algorithms were illustrated on computer reconstruction of various Fontainebleau sandstones. Daïan (1992; 1994) proposed multi-scale geometrical reconstruction of porous structures, which conserves both the pore size distribution and autocorrelation function. Fernandes (1994) and Fernandes *et al.* (1996) improved this model to simulate invasion process in porous media. Xu (1995) also modeled mercury intrusion in this structure and computed the transport properties using the real space renormalization method. A connectivity function was defined by Fernandes *et al.* (1996). The multi-scale model can conserve the pore space connected at a large scale. But the JQA method yields values for connectivity function closer to the original sample than the multi-scale reconstruction (Fernandes *et al.*, 1997). Magnani (1996) developed a 3-D opening technique to determine equilibrium interfaces in the reconstructed porous medium that was generated by using the JQA method. The simulated capillary pressure curve of mercury intrusion for a Berea sandstone sample is in good agreement with the experimental one. Bakke and Øren (1996) generated 3-D pore structures based on numerical modeling of the main sandstone-forming geological processes, which are simulated in sand grain sedimentation, compaction and diagenesis steps. Petrographical analysis provides the necessary input for the modeling, which is grain size distribution of the thin section. The 3-D pore space network of the modeled sandstone is extracted from its complementary mineral matrix network using 3-D image analysis techniques. A scale-independent invasion percolation based analysis determines the spatial continuity of the pore network in the X, Y, and Z directions. A 3-D pore network which is representative of a strongly water wet Bentheimer sandstone is

generated and used as input to a two-phase network flow simulator. Computed absolute and relative permeabilities are in good agreement with those determined experimentally.

1.3. OUTLINE OF THIS WORK

The flow behavior in real porous media depends strongly on the geometrical and topological characteristics of the pore space; i.e., on the sizes and shapes of the pores, the sizes and shapes of the connections between the pores, the order in which the pores and connections of different size and shape are connected, and the degree of interconnection (coordination number). From the review in section 1.2, the present network models are all based on some information about pore structure, such as pore body and throat size distribution and coordination numbers. These data are almost assumed in the previous works (e.g., Ioannidis and Chatzis, 1993). Although Bakke and Øren (1996) generated 3-D pore network and obtained its skeleton, they also used it to obtain some information of pore structure as input to a two-phase network flow simulator. Pieritz (1994) used the median line graph to obtain the pore site and bond as well as coordination number distribution from black (pore) and white (matrix) pictures of 2-D polished section of porous materials. However, the statement that 2-D observations in thin section are representative for the 3-D sample is only valid for areal and volumetrical considerations, but not for the geometrical measurements, especially for the connectivity. Thovert *et al.* (1993) used thinning algorithms to obtain the graph of the 3-D pore structure and derived the topological characteristics, such as the number of loops. However, as discussed by Bakke and Øren (1996), visual examination showed that in some complex voxel junctions, the algorithms introduced artificial holes in the pore network skeleton. This can be quite catastrophic for fluid flow purposes because it may result in the addition of artificial hydraulic circuits and wrong coordination numbers for the pore nodes. Recently, Ma (1994; 1995) proposed a 3-D fully parallel thinning algorithm, which preserves connectivity, i.e., an object and its skeleton have the same topology. It enables the network to preserve the same connectivity as the pore space. Reconstruction of 3-D porous media from 2-D thin section image is an important method for characterizing the porous media, as discussed in section 1.2. But the present JQA method is time consuming. Following the works in LMPT (Laboratory of Porous Media and Thermophysical Properties of Materials, Federal University of Santa Catarina, Brazil), the object of this work is by using

image analysis techniques to develop a fast reconstruction method and predict the transport properties, such as absolute permeability for porous rocks.

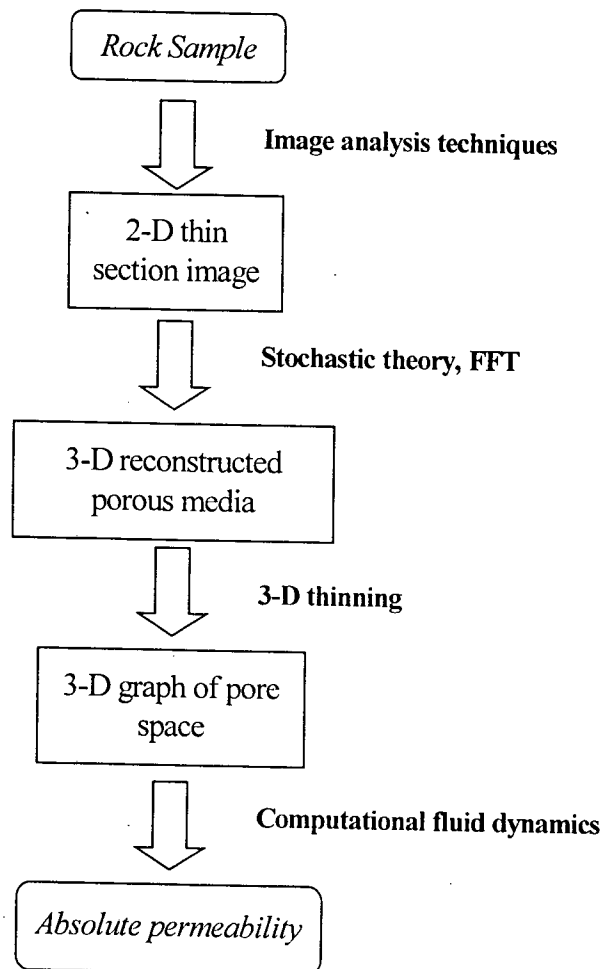


Figure 1.1 - Process for predicting absolute permeability in porous media.

A procedure for predicting the absolute permeability for a rock sample in this work is shown in Figure 1.1. At first, the 2-D thin section image is acquired and segmented by image analysis techniques. The porosity and autocorrelation function (or normalized autocovariance function) of 2-D thin section image are calculated by using Fourier transform. Then 3-D pore structure is generated, which possesses the same porosity and autocorrelation function as the

real sample in study. The reconstruction process of 3-D porous media based on Fourier transforms method is proposed as follows:

- 1) Calculating normalized autocovariance function $R_Y(\mathbf{u})$ of a Gaussian field $Y(\mathbf{x})$ from the measured normalized autocovariance function $R_Z(\mathbf{u})$;
- 2) Making the Fourier transform of $R_Y(\mathbf{u})$ to obtain power spectrum of $Y(\mathbf{x})$;
- 3) The Fourier spectrum of $Y(\mathbf{x})$ is the square root of the power spectrum;
- 4) Phase angle is taken at random;
- 5) Generating complex Fourier coefficients of $Y(\mathbf{x})$;
- 6) Making the inverse Fourier transform to get $Y(\mathbf{x})$;
- 7) Using truncated method to obtain the 3-D binary (pore and solid) function $Z(\mathbf{x})$.

After the reconstructed porous medium is generated, the graph of 3-D pore space (skeleton) can be obtained by using a thinning algorithm, which preserves connectivity. Using the graph of 3-D pore space, one can obtain the main flow path for a single flow, which is classified into nodes and links. The local cross-sectional area and perimeter normal to the flow direction in every point of each link point can be recorded to predict the absolute permeability. Resistance to flow may be estimated for each link. A fluid pressure is calculated at each pore node, and total volumetric flux through the network is computed. Then absolute permeability can be predicted from the corresponding network for the samples.

In chapter 2 we introduce image analysis techniques and use Fourier transform to get statistical properties such as porosity and autocorrelation function for a sample. A new method for reconstructing 3-D porous media based on Fourier transforms is proposed and discussed in chapter 3. In chapter 4, we represent the 3-D thinning algorithm and visualization of 3-D object. Then the graph (skeleton) of 3-D reconstructed porous medium is obtained by using thinning algorithm. The simulation and prediction of permeability are discussed in chapter 5. In chapter 6 the results for several rock samples are given and discussed. At last, conclusions are summarized and some works for the future are suggested in chapter 7.

2. IMAGE ANALYSIS TECHNIQUES FOR CHARACTERIZATION OF POROUS STRUCTURE

2.1. INTRODUCTION

Image analysis is a process of discovering, identifying, and understanding patterns that are relevant to the performance of an image-based task. Gonzalez and Woods (1992) divided the spectrum of techniques in image analysis into three basic areas. They are (1) low-level processing (*image acquisition, preprocessing*), (2) intermediate-level processing (*segmentation, representation and description*), and (3) high-level processing (*recognition and interpretation*). The use of these techniques depends mainly on the problem being solved. In this work, we use image analysis techniques for characterization of porous structure.

Lin and Cohen (1982) were among the first to analyze the structure of a real porous medium, using epoxy impregnation techniques. The sample was polished and various serial section slices are recorded. Then the 3-D pore space was reconstructed manually. Various quantities such as the porosity, the connectivity and the mean grain diameter were derived from these data. The same technique was used by Koplik *et al.* (1984). The electrical conductivity and fluid flow permeability in a disordered random medium were calculated from the microstructure of the pore space. Berryman and Blair (1986) analyzed scanning electron microscope image of cross sections of several porous specimens using image analysis technique. The porosity and specific surface area for various materials were calculated from correlation function. These values were combined with known value of electrical formation factor to estimate fluid permeability using an empirical correlation. Recently, the use of high-speed computers, together with advanced methods of image acquisition and analysis makes the works in this field faster and more accurate. Recent development in statistical theory makes it feasible to generate realistic 3-D models of porous rocks using information extracted from 2-D images of sections through pore casts (Quiblier, 1984; Adler *et al.*, 1990; Fernandes, 1994; Ioannidis *et al.*, 1995). These advancements enable the acquisition of virtual

serial sections for subsequent pore space characterization, i. e., measurement of geometrical and topological parameters of the pore space (Kwiecien *et al.*, 1990; Thovert *et al.*, 1993). Mathematical morphology is a consistent approach for characterization of data fields (Serra, 1982), being both a method of image analysis and a method of measurement. Quenard *et al.* (1992) used an approach based on mathematical morphology for simulation of sorption isotherm in a random porous medium. Opening (2-D and 3-D) and median line graphics (2-D) methods (Pieritz, 1994; Fernandes, 1994; Magnani, 1996) enable the statistical investigation of porous sections, the simulation of invasion process, and the determination of equilibrium configuration in porous media. Digital 2-D Fourier transforms have been applied to several image and signal analysis tasks. In most cases, the objective has been to filter an image or to recognize a known pattern from an image. It is possible to generate petrographic images from thin sections and qualify the spatial arrangement of selected rock components (mineral grains and pores) using 2-D Fourier transform. Prince and Ehrlich (1990) presented the fundamental framework of 2-D Fourier analysis to characterize the type and degree of spatial order in an image for sandstones. This type of analysis provides a means to quantify and analyze the spatial arrangement of rock components. One of the most desirable properties of Fourier transform is its reversibility. Using selected components of the power spectrum, the inverse transform can be used to build synthetic images, which highlight those petrologic components that most affect the power spectrum.

In section 2.2, we introduce the procedures of image acquisition and segmentation for a rock sample. The definition of Fourier transform and the properties of power spectrum are described in section 2.3. In section 2.4, the main statistical properties such as porosity and autocorrelation function for 2-D thin section image are calculated using Fourier transform and compared with the previous simple method. These data are important for the reconstruction of 3-D porous media and prediction of permeability. In section 2.5, two algorithms for 2-D skeleton are represented to obtain the 2-D graph of the pore space.

2.2. IMAGE ACQUISITION AND SEGMENTATION

The method to obtain digital images of the porous media usually consists of the following steps (Philippi *et al.*, 1994; Philippi and Souza, 1995), as shown in Figure 2.1. Samples of the porous media are vacuum-impregnated with a resin mixed with ethyl alcohol, which are then polished. A scanning electron microscope is used at the emissive mode to give

high-contrast images of the pore space and the solid matrix. Various images with different magnifications are produced and digitized with a raster scanning digitizer (HP IIC Scanner). The resulting digital images are then processed using digital image segmentation techniques to obtain an image of zeros and ones that closely approximate the solid matrix and pore space of the working image. In general, autonomous segmentation is an important step, but one of the most difficult tasks in image analysis. It is not the object of this work. Several methods for the segmentation of colored and gray-level images have been developed by Philippi and Fernandes (1995).

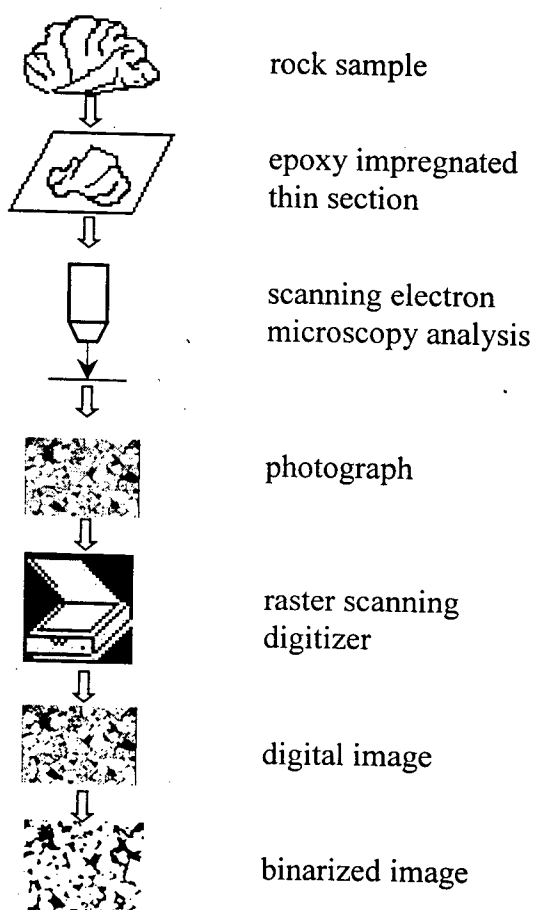


Figure 2.1 - Schematic procedures of image production methodology.

Figure 2.2 shows digital image of a thin section of the material 500 mD Berea sandstone, which is 609×458 pixels with magnification of $50\times$. Each pixel corresponds to 2.6 microns. The experimental porosity obtained by mercury intrusion is approximately 0.225. This image is a color image obtained by using optical microscopy in CENPES,

PETROBRAS. In Figure 2.2, the black parts may be oils or calcinated materials, and these parts are considered as solid matrix in binarization process. The color image was segmented using the method based on the union of object boundary and image HUE histogram information (Philippi and Fernandes, 1995). Figure 2.3 shows the corresponding binary image, in which black and white represent pore and solid phase, respectively.

2.3. FOURIER TRANSFORM AND ITS PROPERTIES

Linear transformations, particularly the Fourier transforms, are important tools for image analysis and processing. In the two-dimensional case the discrete Fourier transform pair (Gonzalez and Woods, 1992) is:

$$\mathfrak{F}(f(x, y)) = \hat{f}(f_x, f_y) = \frac{1}{MN} \sum_{x=0}^{M-1} \sum_{y=0}^{N-1} f(x, y) \exp[-j2\pi(\frac{xf_x}{M} + \frac{yf_y}{N})], \quad (2.1)$$

for $f_x=0, 1, 2, \dots, M-1, f_y=0, 1, 2, \dots, N-1, j=\sqrt{-1}$ and

$$f(x, y) = \mathfrak{F}^{-1}(\hat{f}(f_x, f_y)) = \sum_{f_x=0}^{M-1} \sum_{f_y=0}^{N-1} \hat{f}(f_x, f_y) \exp[j2\pi(\frac{xf_x}{M} + \frac{yf_y}{N})], \quad (2.2)$$

for $x=0, 1, 2, \dots, M-1, y=0, 1, 2, \dots, N-1$.

For an image of a two-dimensional porous section, the Fourier transform is generally complex,

$$\hat{f}(f_x, f_y) = \hat{f}_r(f_x, f_y) + j\hat{f}_i(f_x, f_y), \quad (2.3)$$

where $\hat{f}_r(f_x, f_y)$ and $\hat{f}_i(f_x, f_y)$ are the real and imaginary components of $\hat{f}(f_x, f_y)$, respectively.

It is often convenient to express Eq. (2.3) in exponential form, i.e.:

$$\hat{f}(f_x, f_y) = |\hat{f}(f_x, f_y)| e^{j\phi(f_x, f_y)}, \quad (2.4)$$

where

$$|\hat{f}(f_x, f_y)| = [\hat{f}_r^2(f_x, f_y) + \hat{f}_i^2(f_x, f_y)]^{1/2}, \quad (2.5)$$

and

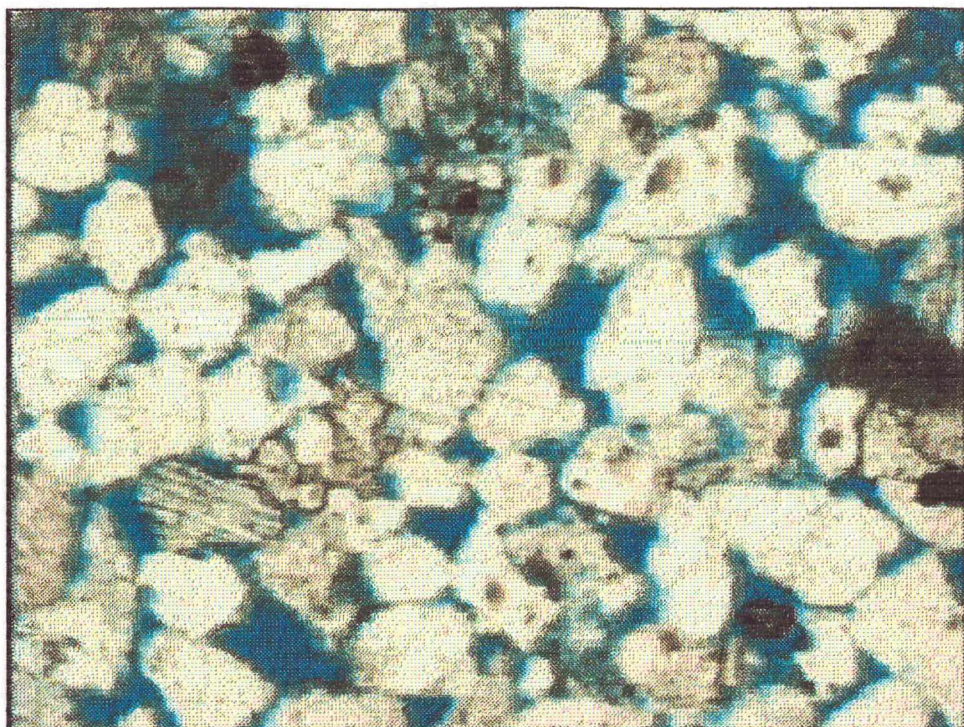


Figure 2.2 - Digital image of a thin section of a 500 mD Berea sandstone, which is 609×458 pixels (magnification = $50 \times$).

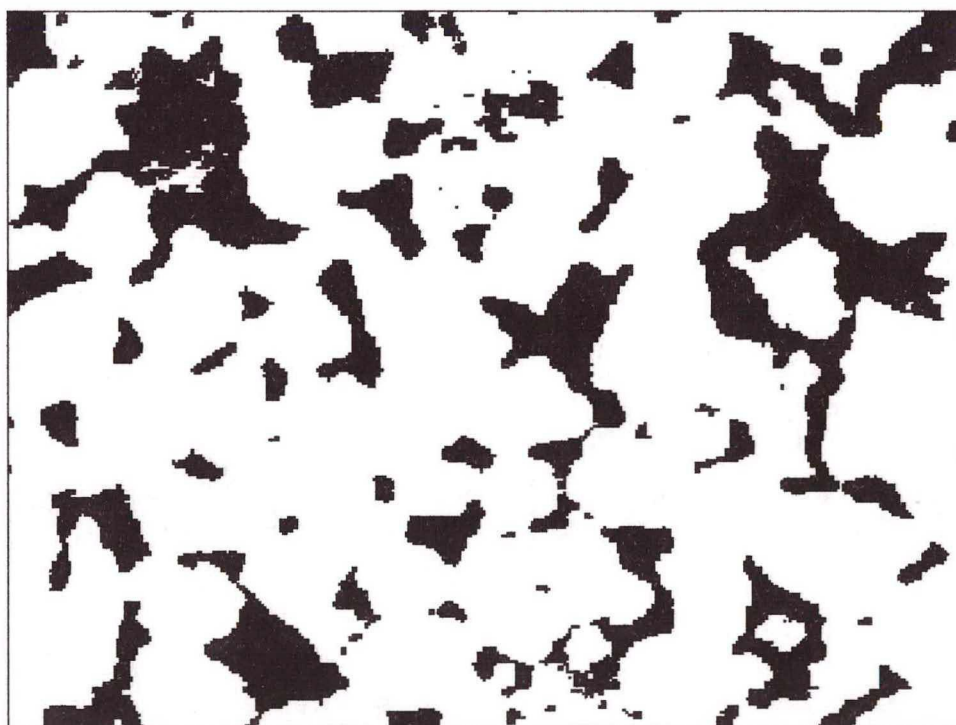


Figure 2.3 - Binary image from the image of Figure 2.2, in which black and white represent pore and solid phase, respectively.

$$\Phi(f_x, f_y) = \arctg\left[\frac{\hat{f}_i(f_x, f_y)}{\hat{f}_r(f_x, f_y)}\right]. \quad (2.6)$$

The magnitude function $|\hat{f}(f_x, f_y)|$ is called the *Fourier spectrum* of $f(x,y)$ and $\Phi(f_x, f_y)$ its *phase angle*. The square of the Fourier spectrum,

$$\wp(f) = |\hat{f}(f_x, f_y)|^2 = \hat{f}_r^2(f_x, f_y) + \hat{f}_i^2(f_x, f_y), \quad (2.7)$$

is commonly referred to as the *power spectrum* of $f(x,y)$. The term *spectral density* is also commonly used to denote the power spectrum. The variables f_x and f_y appearing in the Fourier transform are often called *frequency variables*.

The discrete Fourier transform has a number of mathematical properties, which can be used to simplify problems or which lead to useful application. The following properties will be used in this work.

(1). *Power spectra* contain information related to the spatial arrangement of objects as well as information related to the size and shape of the objects. An image containing large objects tends to concentrate power in the fundamental frequencies, i.e., the axes $f_x=0$ and $f_y=0$. Figure 2.4 shows the power spectrum of two different images illustrating this property. For each point belonging to the transformed image, power spectrum value is represented by a gray level value between 0 and 255. As the size of the objects is reduced, power spectrum distribution becomes more decentralized. Shape also affects the distribution of power spectrum \wp . Figure 2.5 shows two images containing objects of approximately the same size, but with different shapes. Square shapes generate power in the $(0, f_y)$ and $(f_x, 0)$ directions, consistent with the orientation of the square edges. Power spectrum produced by circles distributes in a circular pattern.

(2). The Fourier transform of a real function $\mathfrak{F}(f)$ is a *hermitian* function, i.e., the real part of $\mathfrak{F}(f)$ is even and the imaginary part is odd. This can be expressed as symmetries of the coefficients that are specific for 1-D, 2-D and 3-D cases (see Pardo-Igúzquiza and Chica-Olmo, 1993). For example, Fourier transform of a real function for 1-D case is

$$\hat{f}(f) = \hat{f}_r(f) + j \hat{f}_i(f). \quad (2.8)$$

$\hat{f}_r(f)$ must be even:

$$\hat{f}_r(f) = \hat{f}_r(-f). \quad (2.9)$$

$\hat{f}_i(f)$ must be odd:

$$\hat{f}_i(f) = -\hat{f}_i(-f). \quad (2.10)$$

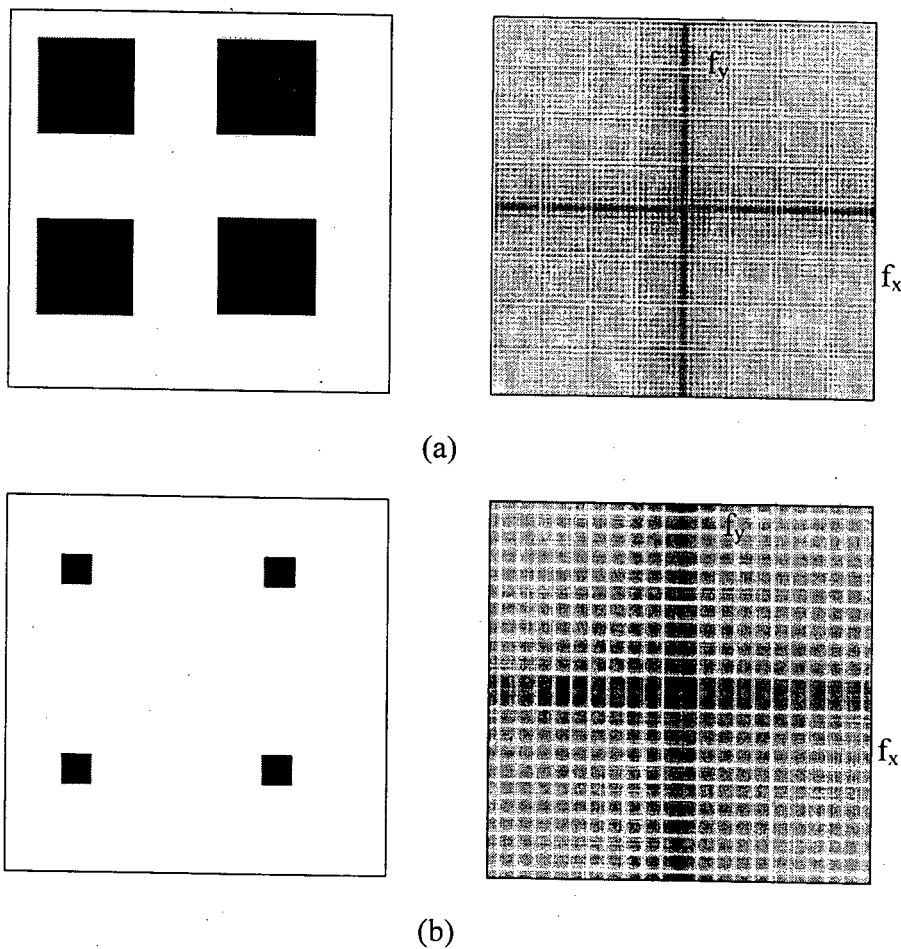


Figure 2.4 - Size effect on the power spectrum (a) image of large objects and its power spectrum (b) image of small objects and its power spectrum.

(3). Given two functions f and g , and their Fourier transforms \hat{f} and \hat{g} , we can form two combinations of special interests. The *convolution* of two functions, denoted $f * g$, is defined for 2-D discrete case by

$$f * g = \frac{1}{MN} \sum_i \sum_j f(i, j) g(i - x, j - y). \quad (2.11)$$

where M and N are the domain size of functions f and g and periodic boundaries are used to define $g(i-x, j-y)$ when $(i-x, j-y)$ extends beyond $M \times N$ dimensional domain. It turns out that the convolution $f * g$ is one member of a Fourier transform pair:

$$f * g \Leftrightarrow \hat{f} \cdot \hat{g}. \quad (2.12)$$

where \Leftrightarrow indicates the Fourier transform pair. Eq. (2.12) is called *convolution theorem*, i.e., the Fourier transform of convolution is just the product of the individual Fourier transforms.

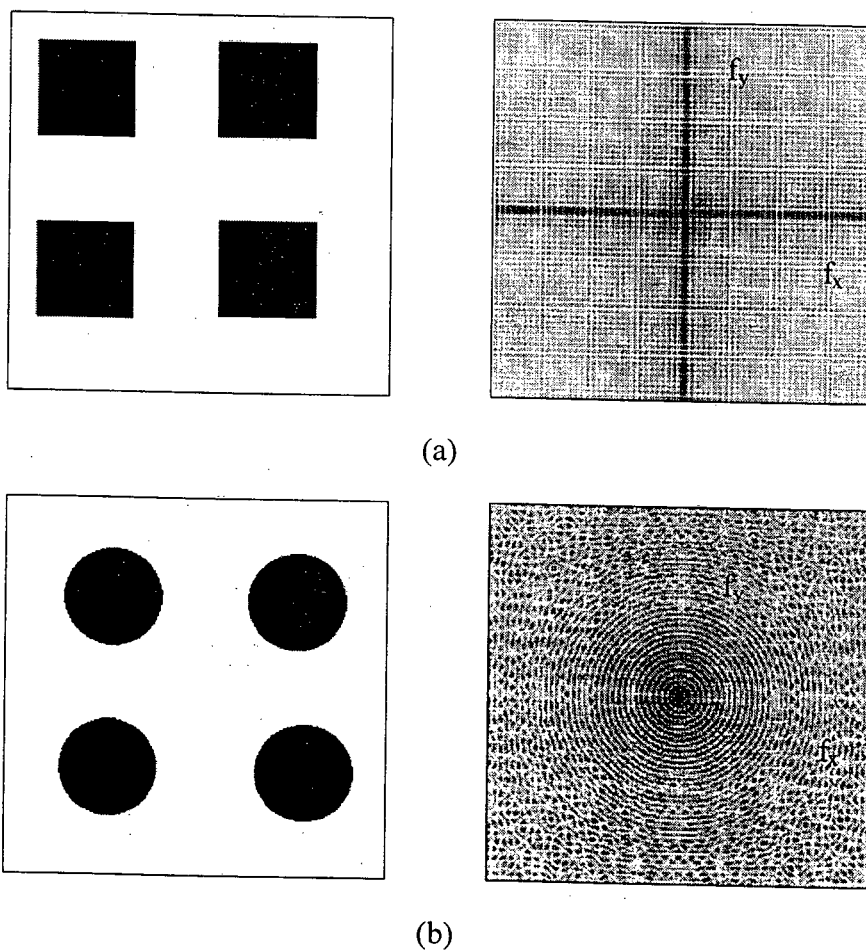


Figure 2.5 - Shape affect on power spectrum (a) image of square objects and its power spectrum (b) image of circle objects and its power spectrum.

The *correlation* of two functions f and g , denoted $f \circ g$, is defined for 2-D discrete case by

$$f \circ g = \frac{1}{MN} \sum_i \sum_j f^*(i, j) g(i+x, j+y). \quad (2.13)$$

where periodic boundaries are also used to define $g(i+x, j+y)$ when $(i+x, j+y)$ extends beyond the $M \times N$ dimensional domain of $f(x, y)$ and $g(x, y)$. It turns out that the function $f \circ g$ is also one member of a Fourier transform pair:

$$f \circ g \Leftrightarrow \hat{f}^* \cdot \hat{g}. \quad (2.14)$$

where $*$ indicates the complex conjugate. Eq. (2.14) is called *correlation theorem*, i.e., the result of multiplying the Fourier transform of one function by the complex conjugate of other is the Fourier transform of their correlation. Particularly, the Fourier transform of the autocorrelation of a function f is the power spectrum $\wp(f)$:

$$f \circ f \Leftrightarrow |\hat{f}|^2. \quad (2.15)$$

This result is the so-called *Wiener-Khinchin theorem*.

2.4. CHARACTERIZATION OF 2-D THIN SECTIONS OF POROUS MEDIA

In porous materials, one can theoretically distinguish between the solid and pore phase. The pore space of porous media can be characterized by the phase function $Z(\mathbf{x})$ as follows:

$$Z(\mathbf{x}) = \begin{cases} 1 & \text{when } \mathbf{x} \text{ belongs to the pore space} \\ 0 & \text{otherwise} \end{cases}, \quad (2.16)$$

where \mathbf{x} denotes the position with respect to an arbitrary origin.

Due to different definitions of statistical properties in the literatures, we first define the porosity, the autocorrelation function, and the normalized autocovariance function. The porosity ε and the autocorrelation function $C_Z(\mathbf{u})$ can be defined using statistical averages (which will be denoted by an overbar):

$$\varepsilon = \overline{Z(\mathbf{x})}, \quad (2.17)$$

$$C_z(\mathbf{u}) = \overline{Z(\mathbf{x})Z(\mathbf{x} + \mathbf{u})}, \quad (2.18)$$

where \mathbf{u} is a displacement in the plane of the porous section. Similarly, the normalized autocovariance function can be defined as

$$R_z(\mathbf{u}) = \frac{[\overline{Z(\mathbf{x}) - \varepsilon}] \cdot [\overline{Z(\mathbf{x} + \mathbf{u}) - \varepsilon}]}{(\varepsilon - \varepsilon^2)}. \quad (2.19)$$

Porosity ε is obviously a positive quantity between zero and one. It can be shown that a function $C_z(\mathbf{u})$ is an autocorrelation function if all its Fourier components are non-negative (Papoulis, 1965). When the material is supposed to be homogeneous, the statistical averages can be replaced by volume averages. When it is supposed to be isotropic, $R_z(\mathbf{u})$ only depends upon displacement \mathbf{u} and these volume averages can be replaced by surface averages; hence the use of thin sections is justified.

One simple method to calculate the porosity, the autocorrelation function and normalized autocovariance function was used by Adler *et al.* (1990) and Philippi *et al.* (1994). Let S be a section of a porous medium, given by a 2-D binary representation like the one shown in Figure 2.3, porous phase is represented in black and the solid matrix in white. The binary image S is divided into two halves S_1 and S_2 . Hence,

$$S = S_1 \cup S_2, S_1 \cap S_2 = \emptyset. \quad (2.20)$$

The porosity is simply defined as the proportion of pore space contained in a given section. In order to get an idea of the homogeneity of the sample, this ratio is measured twice, i.e. on S and S_1 . The corresponding values are denoted ε and ε_h . The constant character of the porosity is one of the criteria to select a thin section or not. In the sample case of Figure 2.3, ε and ε_h are 0.2214 and 0.2229, respectively. The effects of sample homogeneity on reconstruction of 3-D porous medium and prediction of permeability will be discussed in details in chapter 6. In order to calculate $R_z(\mathbf{u})$, S_1 is first translated by a distance \mathbf{u} along the x -axis; it yields $S_1(+\mathbf{u})$. The spatial average indicated in Eq. (2.18) is calculated as the proportion of pore space in an intersection of images $S_1(+\mathbf{u}) \cap S$. This gives the autocorrelation function. To get $R_z(\mathbf{u})$, the other operations indicated in the Eq. (2.19) are then performed algebraically. Figure 2.6 shows the autocorrelation functions in two directions and their average for the sample image shown in Figure 2.3.

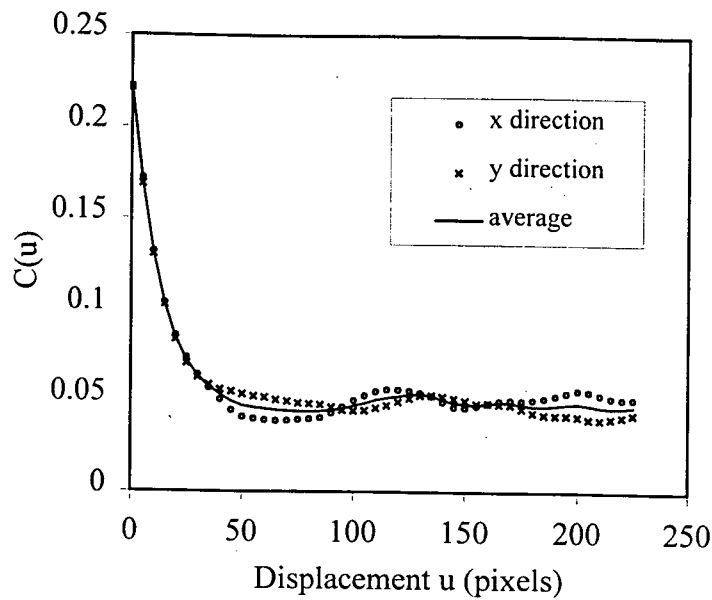


Figure 2.6 - Autocorrelation functions in two directions and their average for Figure 2.3.

From Figure 2.6, one can see that the autocorrelation functions in two directions are almost the same for short displacements. But for large displacements they are very different. This may be due to poor statistics for large displacements. Although we have assumed statistical homogeneity and isotropy, these assumptions will be only approximately satisfied for any particular image. For an image $Z(x,y)$, using the definition of Fourier transform, $\mathfrak{Z}(Z)$ and the Wiener-Khinchin theorem, the Fourier transform of the autocorrelation function is also the power spectrum of $Z(x,y)$. In order to improve the above simple method, the Fourier transform of the images of porous sections is used to characterize the porous media. In this way, the Fourier transform of phase function $Z(x,y)$ at $(0,0)$ is the porosity ϵ ,

$$\hat{Z}(0,0) = \frac{1}{MN} \sum_{x=0}^{M-1} \sum_{y=0}^{N-1} Z(x,y) = \epsilon. \quad (2.21)$$

A 2-D discrete version of Eq. (2.18) is:

$$C(x,y) = \frac{1}{M \times N} \sum_i \sum_j Z(i,j) \cdot Z(i+x,j+y), \quad (2.22)$$

where M and N are image sizes and periodic boundaries are used to define $Z(i+x, j+y)$ when $(i+x, j+y)$ extends beyond the $M \times N$ two dimensional image. The autocorrelation function can be obtained rapidly using Fourier transform methods. Figure 2.7 and Figure 2.8 show.

respectively, a surface display and a gray level representation of the power spectrum for the binary image in Figure 2.3. The autocorrelation function is inverse Fourier transform of the power spectrum. A surface display of 2-D autocorrelation function is shown in Figure 2.9.

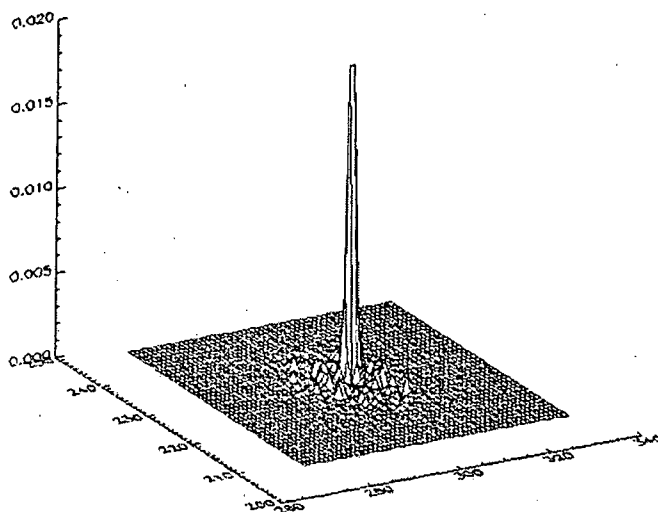


Figure 2.7 - Surface display of power spectrum for Figure 2.3.

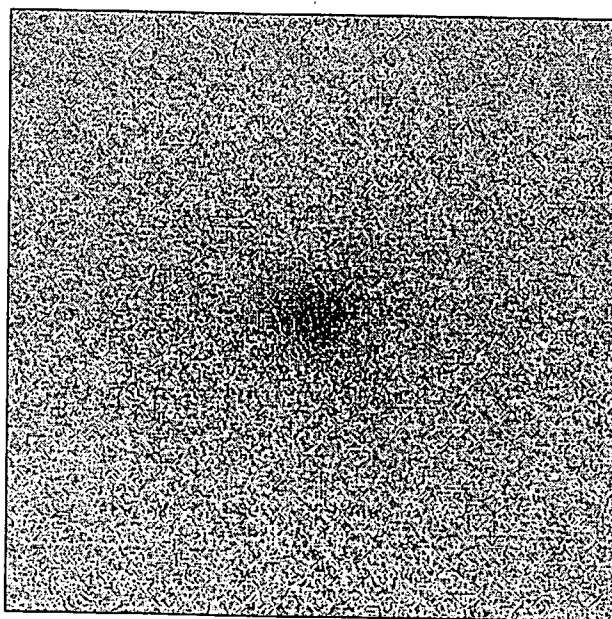


Figure 2.8 - Gray level representation of the power spectrum for the porous section presented in Figure 2.3.

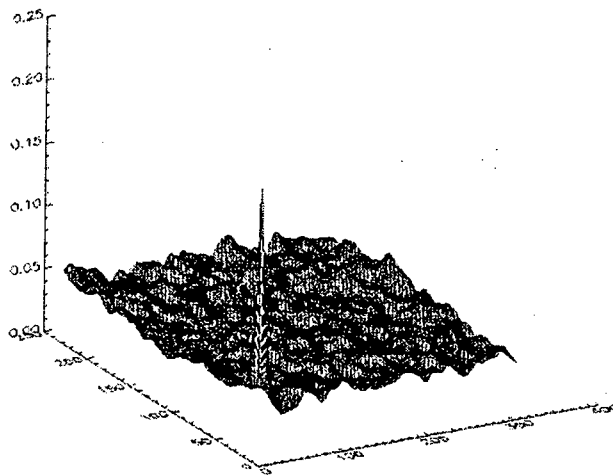


Figure 2.9 - Surface display of 2-D autocorrelation function for the porous section shown in Figure 2.3.

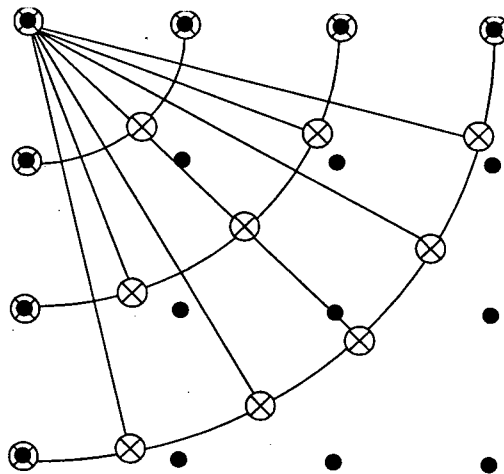


Figure 2.10 - Illustrations for obtaining the isotropic autocorrelation function from discrete values for a particular image.

Given the two dimensional $C(x,y)$, one can obtain the desired one dimensional (isotropic) autocorrelation function $C(u)$ by averaging over the $C(x,y)$ values at a fixed radius u (Berryman and Blair, 1986). Except for the cases $(0,u)$ and $(u,0)$, $C(x,y)$ will not generally be known at the points of interest (see Figure 2.10). Therefore we define the function

$$\bar{C}(u, \theta) \equiv C(u \cos \theta, u \sin \theta), \quad (2.23)$$

where $u \sin \theta$ and $u \cos \theta$ are not both integers, the value of the right-hand side of Eq. (2.23) is defined as the bilinear interpolation from the lattice value $C(x, y)$. Then the isotropic average of autocorrelation function is given by

$$C(u) = \frac{1}{2u+1} \sum_{i=0}^{2u} \bar{C}(u, \frac{\pi i}{4u}). \quad (2.24)$$

Figure 2.11 shows the autocorrelation function obtained from the above equation and comparison with the previous simple method. The fluctuations due to periodicity are drastically reduced, when $C(u)$ is calculated using Fourier transform. As it is apparent from Figure 2.11, $C(u)$ is almost monotonically decreasing with u .

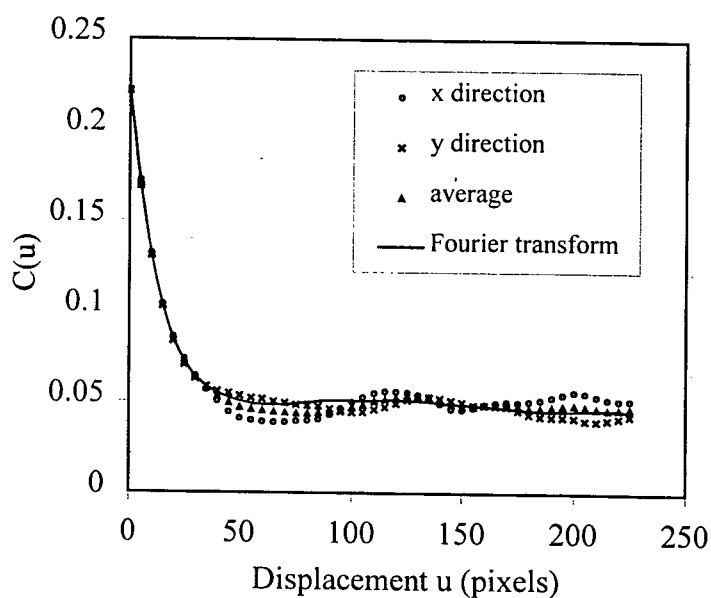


Figure 2.11 - Comparison of autocorrelation functions obtained by Fourier transform and simple method.

2.5. SKELETON OF 2-D POROUS MEDIA

An important approach to representing the structural shape of a plane region (for example, a region can be the pore for an image of porous media) is to reduce it to a graph. This reduction may be accomplished by obtaining the skeleton of the region by a thinning or skeletonizing algorithm. Thinning procedures play a central role in a broad range of problems

in image processing. Serra (1982) and Adler (1992) defined the skeleton of the pore space as the set of points (voxels) at equal distance from two or more points of the solid wall. The skeleton may thus be thought of as a spatial representation of the center line of pore space. This spatial center line will contain points where two or more lines meet. These meeting points are the network nodes (approximate center of pore bodies) which are connected to other nodes by links or pore throats. Pieritz (1994) used median line graphics technique and obtained the site and bond distributions from 2-D thin section images of porous materials. In 2-D image analysis, skeleton extraction from binary images is carried out by means of various algorithms. The important property of thinning is that it does not change the picture topology. Basically there are two types of methods: (1) thinning - iteratively deleting contour points of a region and (2) skeletonizing - depending on the definition of a distance. Although 2-D skeleton can not represent 3-D properties, the concept is basis for 3-D skeleton. In this section, the basic concepts and above two typical algorithms are introduced.

2.5.1. A 2-D Thinning Algorithm

An algorithm for thinning binary region by Zhang and Suen (1984) is used here. Pore points are assumed to have value 1 and solid points to have value 0. They are denoted as $B=\{1\}$ and $\bar{B}=\{0\}$, respectively. The method consists of successive passes of two basic steps applied to the contour points of the given image, where a contour point is any pixel with value 1 and having at least one 8-neighbour value 0. With reference to the 8-neighbourhood definition shown in Figure 2.12, step 1 flags a contour point p for deletion if the following conditions are satisfied:

$$(a) \quad 2 \leq N(p) \leq 6$$

$$(b) \quad s(p)=1$$

$$(c) \quad n_3 \cdot n_5 \cdot n_7 = 0$$

$$(d) \quad n_5 \cdot n_7 \cdot n_1 = 0$$

n_2	n_3	n_4
n_1	p	n_5
n_8	n_7	n_6

where $N(p)=\sum_{i=1}^8 n_i$, $s(p)$ is the number of 0-1 transitions in the ordered sequence of n_1, \dots, n_8 .

Figure 2.12- The eight neighbors of a pixel p .

For example, $N(p)=4$ and $s(p)=3$
in Figure 2.13.

In step 2, conditions (a) and (b) remain the same, but conditions (c) and (d) are changed to:

0	0	1
1	p	0
1	0	1

Figure 2.13 - A pixel p with $N(p)=4$ and $s(p)=3$.

$$(c') \quad n_3 \cdot n_5 \cdot n_1 = 0$$

$$(d') \quad n_3 \cdot n_7 \cdot n_1 = 0$$

Step 1 is applied to every border pixel in the binary image under consideration. If one or more of conditions (a) - (d) are violated, the value of the point in question is not changed. If all conditions are satisfied the point is marked for deletion. However, the point is not deleted until all border points have been processed. This delay prevents changing the structure of the data during execution of the algorithm. After step 1 has been applied to all border points, those that were marked are deleted (changed to 0). Then step 2 is applied to the resulting data in exactly the same manner as step 1. Thus one iteration of the thinning algorithm consists of (1) applying step 1 to mark border points for deletion; (2) deleting the marked points; (3) applying step 2 to mark the remaining border; (4) deleting the marked points.

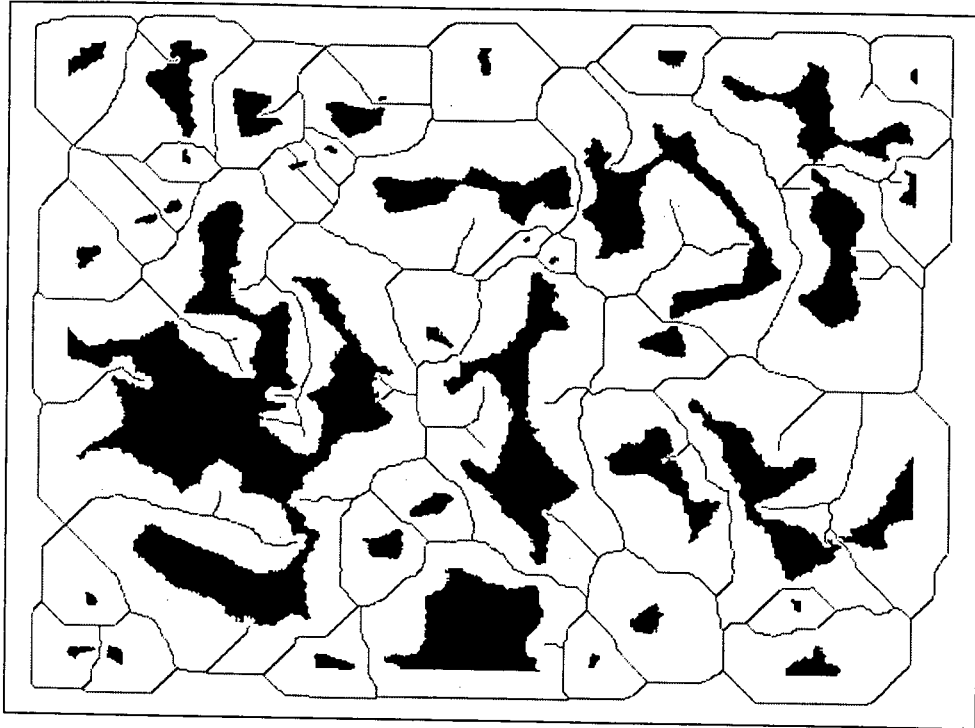
This procedure is applied iteratively until no further points are deleted, at which time the algorithm terminates, yielding the skeleton of the image. Figure 2.14 shows the result of thinning algorithm (a) skeleton and (b) its backbone.

2.5.2. A 2-D Skeletonizing Algorithm

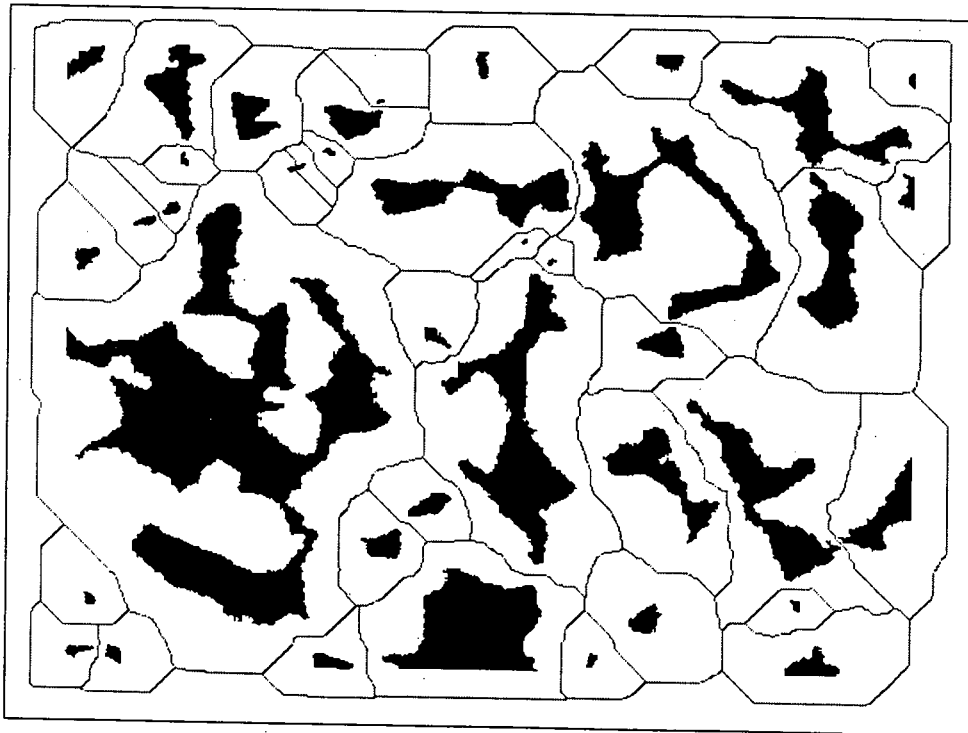
Another method to extract the skeleton (Sanniti di Baja, 1994) is according to a d_{34} distance transform. The maximal centers and saddle pixels are parallel-wise detected. Since they do not generally group into a connected set, further skeletal pixels are found by growing connected paths.

1. d_{34} distance transform:

The d_{34} distance transform of $B=\{1\}$ with respect to $\bar{B}=\{0\}$ is a multi-valued set whose pixels are labeled according to their d_{34} from \bar{B} .



(a)



(b)

Figure 2.14 - The result of thinning algorithm: (a) skeleton and (b) its backbone.

To obtain the d_{34} distance transform, two raster scans through the image, performed in forward and backward fashion, respectively, are sufficient. During both of these scans, sequential operations are performed on every pixel p in B . In this work, the sequence forward-backward is considered, and the local operations:

$$b_1(p) = \min(n_1+3, n_2+4, n_3+3, n_4+4)$$

$$b_2(p) = \min(p, n_5+3, n_6+4, n_7+3, n_8+4)$$

are computed, respectively, within the first and the second raster scan.

2. Median axis (Maximal center):

Each pixel p can be interpreted as the center of disc of radius R_p , which includes all the black pixels whose distance from p is less than p . A disc of radius R_p not completely included in the disc of radius R_q centered on any neighbor q of p is called a maximal disc. A pixel p belongs to the median axis if it is the center of a maximal disc of radius R_p . A pixel p on the d_{34} distance transform is median axis if, after the labels 6 and 3 have been changed into 5 and 1 respectively, it is

$$n_i < p+3 \text{ for every odd-neighbor } n_i$$

and

$$n_i < p+4 \text{ for every even-neighbor } n_i.$$

3. Saddle pixel:

A pixel p in the d_{34} distance transform is termed a saddle pixel, if in $N(p)$ there exist two 4-connected components of pixels with smaller labels, and one or two 8-connected components of pixels with larger labels. Any pixel p , which is not a median axis, is marked as a saddle pixel if any of the following conditions holds:

- i. In $N(p)$ there is more than one 8-connected component of pixels labeled more than p (Figure 2.15 (a)).
- ii. In $N(p)$ there is more than one 4-connected component of pixels labeled less than p (Figure 2.15 (b)).
- iii. In $N(p)$ there exists a triple of consecutive neighbors of p (odd-neighbor/even-neighbor/odd-neighbor) which are all labeled 3 (Figure 2.15 (c)).

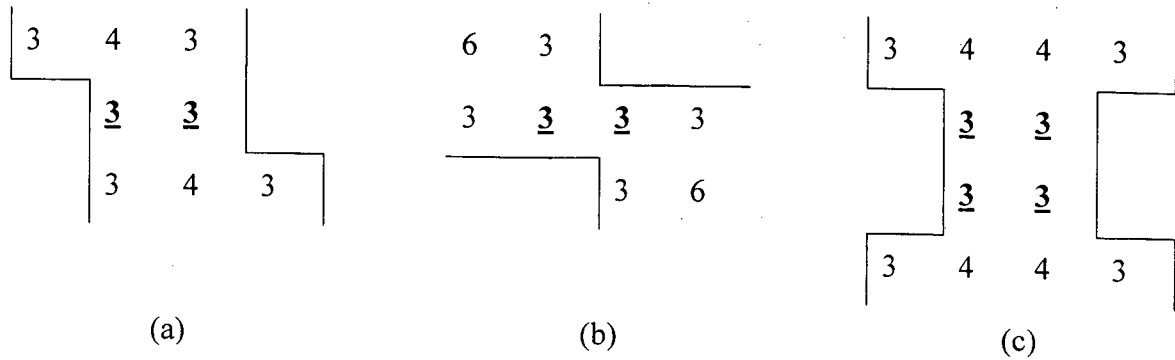


Figure 2.15 - Bold labels satisfy one among three conditions (a) Existence of two 8-connected components of pixels with higher label; (b) Existence of two 4-connected components of pixels with smaller label; (c) Existence of an L-shaped triple of consecutive neighbors labeled 3.

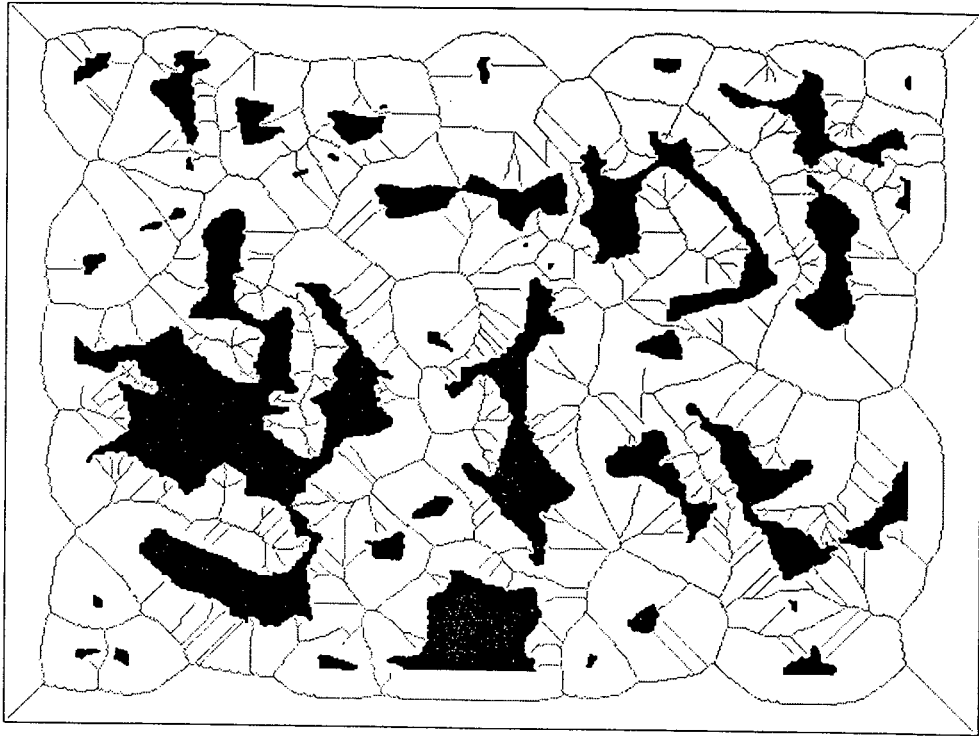
4. Connecting path:

The connecting pixels are identified by growing increasing paths along the direction of the steepest gradient in the d_{34} distance transform, starting from any already marked pixel. The first pixel in the path is the (unmarked) neighbor n_k of a marked pixel p , such that $n_k > p$ and the gradient of q with respect to p is maximum. The gradient is computed as:

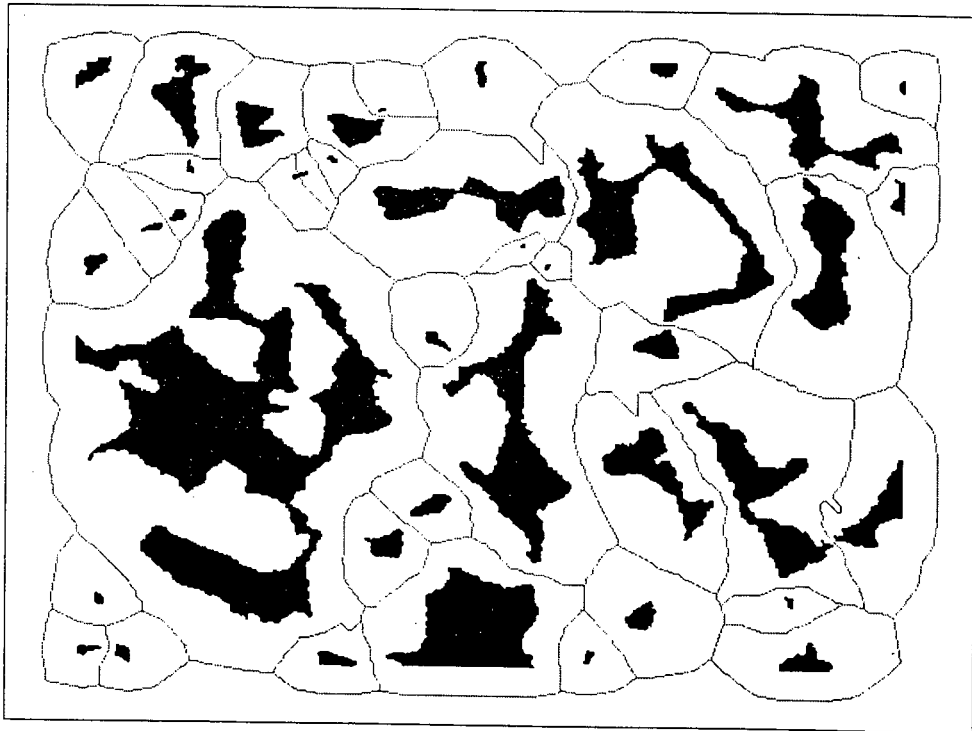
$$\text{grad}(n_k) = \frac{1}{w_m} \times (n_k - p), \quad (2.25)$$

where it is $w_m=3$, for k odd; $w_m=4$ otherwise. The next pixel in the path is similarly found, if any, by analyzing a suitable subset of the neighbors of n_k , selected depending on the direction $p \rightarrow n_k$.

Figure 2.16 gives the result of skeletonizing algorithm (a) skeleton and (b) its backbone. The skeleton can be considered as a network (or graph), which has identical topology as original pore space. The node consists of the end point and branch point. An end point is a pixel of skeleton having a unique 4-connected component of neighbors not in the skeleton. A branch point is a pixel of skeleton, which is not an end point and has more than two neighbors in skeleton. A link point is a pixel of the skeleton, which is neither an end point, nor a branch point. Usually, end points are eliminated and the equivalent network determined; it is also called the backbone of the skeleton. From Figure 2.14 and Figure 2.16, the skeleton obtained by second algorithm has more branches than the first one, but their backbones are very approximate.



(a)



(b)

Figure 2.16 - The result of skeletonizing algorithm: (a) skeleton and (b) its backbone.

3. RECONSTRUCTION OF 3-D POROUS MEDIA

3.1. INTRODUCTION

The stochastic method is based on the idea that an arbitrary complex porous structure can be described by the values of a phase function $Z(\mathbf{x})$ at each point in the porous media (see section 2.4). If the porous structure is statistically homogeneous, then a main assumption, used in the several present works (Quiblier, 1984; Adler *et al.*, 1990; Fernandes, 1994), is to suppose that this structure can be fully described by the porosity ε and autocorrelation function $C(\mathbf{u})$. In this way, the reconstructed porous structure can be generated starting from Gaussian and non correlated field $X(\mathbf{x})$. Linear filter yields a field $Y(\mathbf{x})$ that is still Gaussian but correlated. This field $Y(\mathbf{x})$ is then transformed by nonlinear filter to become a discrete field $Z(\mathbf{x})$ that takes values 0 and 1. This method is very slow for generating large size of reconstructed porous structures. Sometimes it is impossible to resolve some large nonlinear equations. For example, it takes 8 hours or so to generate the 100^3 size in a typical workstation. An alternative way to perform the required linear filtering is to generate $Y(\mathbf{x})$ from $X(\mathbf{x})$ using Fourier transform (Adler, 1992). From a computational point of view, the use of the fast Fourier transform algorithm makes the Fourier transform a more preferred approach than linear filter method. However, application of the Fourier transform method in 3-D is restricted by resident memory requirements of computer.

An existence theorem (Papoulis, 1965) provides an alternative of generating normal field. The truncated Gaussian method based on Fourier transforms is proposed here. The difference between this method and previous work is that the $Y(\mathbf{x})$ is directly generated from its autocorrelation function $R_Y(\mathbf{u})$. It does not need the linear filter and avoids solving the nonlinear equations. Using the fast Fourier transform makes this algorithm more efficient. On the other side, the non-correlated Gaussian field $X(\mathbf{x})$ is not needed. It also reduces the resident memory requirements of computer. Therefore, both operating time and computer memory are improved. This is the advantage of the truncated Gaussian method that uses the

Fourier transform. When the reconstructed porous medium is generated, the transport processes such as invasion of fluids can be simulated, and macroscopic properties such as permeability, capillary pressure, and relative permeability curves can be determined (Adler, 1992; Fernandes, 1994; Magnani, 1996).

Section 3.2 provides the necessary theoretical background. Section 3.3 reviews the reconstruction procedure used by Adler *et al.* (1990) and Fernandes (1994). The new reconstruction method is proposed in section 3.4. Section 3.5 gives an example and discusses the corresponding results and comparison between two methods.

3.2. GENERAL CONCEPTS

The pore space of a porous medium can also be characterized by the phase function $Z(\mathbf{x})$ as follows:

$$Z(\mathbf{x}) = \begin{cases} 1 & \text{when } \mathbf{x} \text{ belongs to the pore space,} \\ 0 & \text{otherwise.} \end{cases} \quad (3.1)$$

The porosity ε , the autocorrelation function $C_Z(\mathbf{u})$, and the normalized autocovariance function $R_Z(\mathbf{u})$ can be defined by the statistical average:

$$\varepsilon = \overline{Z(\mathbf{x})}, \quad (3.2)$$

$$C_Z(\mathbf{u}) = \overline{Z(\mathbf{x})Z(\mathbf{x} + \mathbf{u})}, \quad (3.3)$$

$$R_Z(\mathbf{u}) = \frac{\overline{[Z(\mathbf{x}) - \varepsilon] \cdot [Z(\mathbf{x} + \mathbf{u}) - \varepsilon]}}{[\overline{Z(\mathbf{x}) - \varepsilon}]^2}. \quad (3.4)$$

The objective is to generate a three-dimensional random porous structure with a given porosity and a given autocorrelation function. The medium is homogeneous and isotropic. The idea is to generate a random function of space $Z(\mathbf{x})$ that is one in the pore phase, and zero in the solid phase. $Z(\mathbf{x})$ verifies the two average properties. Porosity is a given positive number smaller than 1. $C_Z(\mathbf{u})$ is a given function of \mathbf{u} that satisfies the general properties of an autocorrelation function.

A porous medium is usually constructed in a discrete manner, which is composed of N^3 small elementary cubes (voxels) with size α . These cubes are filled with either pore or solid phase. Hence, the spatial variables \mathbf{x} and \mathbf{u} take only discrete values. The corresponding trios of integers are denoted by

$$\begin{aligned} \mathbf{x}' &= \mathbf{x} / \alpha = (i, j, k), \\ \mathbf{u}' &= \mathbf{u} / \alpha = (r, s, t), \end{aligned} \quad (3.5)$$

For homogeneous media, the statistical characteristics are independent of position \mathbf{x} in space. Because of homogeneity, the porosity is a constant and $R_Z(\mathbf{u})$ only depends on the vector \mathbf{u} ; that is, each is independent of position \mathbf{x} . In addition, when the porous medium is isotropic, R_Z is a function of only the modulus $u=|\mathbf{u}|$, i.e., $R_Z(\mathbf{u})= R_Z(u)$.

Several statistical methods are found in the literatures to generate discrete random variables that verify Eq. (3.2) - (3.4). Here a truncated Gaussian method is used. Using above concepts, the reconstruction procedure was introduced in 2-D by Joshi (1974) and extended in 3-D by Quiblier (1984) and Adler *et al.* (1990) (JQA method). In the following sections, we first introduce the JQA method. Then a new method is proposed which uses existence theorem and Fourier transforms.

3.3. JQA METHOD

Adler *et al.* (1990) and Fernandes (1994) generated an isotropic medium by a simplified version of an algorithm presented by Quiblier (1984) for generating 3-D porous media. A random and discrete field $Z(\mathbf{x})$ can be devised from a Gaussian fields $X(\mathbf{x})$ when the latter is successively passed through a linear and nonlinear filter.

3.3.1. Linear Filter

First, consider the random field $X(i,j,k)$, where (i,j,k) represents a discrete position in space. The random variables $X(i,j,k)$ are assumed to be normally distributed with a zero mean and a unity variance. The field is non correlated. A linear operator can be defined by an array of coefficients $a(r,s,t)$, where r, s and t belong to a finite cube $[0, Lc]^3$ in Z^3 . Outside this cube, $a(r,s,t)$ is equal to zero. A new random field $Y(i,j,k)$ can be expressed as a linear combination of the random variable $X(i,j,k)$:

$$Y(i, j, k) = \sum_{r,s,t \in [0, Lc]^3} a(r, s, t) X(i + r, j + s, k + t). \quad (3.6)$$

It can be shown that the random variables $Y(i,j,k)$ are Gaussian and centered. Assume, further, that the variance of $Y(i,j,k)$ is equal to one:

$$E\{Y^2(i, j, k)\} = 1. \quad (3.7)$$

Hence, the random variables $Y(i,j,k)$ have a standard normal distribution. Their autocorrelation function $C_Y(\mathbf{u})$ in direction i is

$$C_Y(\mathbf{u}) = E\{Y(i,j,k) \cdot Y(i+u,j,k)\} = \sum_{r,s,t \in [0,L_c]} a(r,s,t)a(r+u,s,t), \quad (3.8)$$

where $u+r$ is determined mod N .

3.3.2. Nonlinear Filter

The porous medium represented by $Z(i,j,k)$ (0 and 1) is extracted from $Y(i,j,k)$ by a nonlinear filter G :

$$Z=G(Y). \quad (3.9)$$

When G is known, the statistical properties of the random field Z can be derived from the properties of Y . Generally, one can determine the normalized autocovariance function $R_Z(\mathbf{u})$ when G and $R_Y(\mathbf{u})$ are known. $R_Z(\mathbf{u})$ can be expressed as follows:

$$R_Z(\mathbf{u}) = \frac{E\{(Z(\mathbf{x}) - E\{Z\})(Z(\mathbf{x} + \mathbf{u}) - E\{Z\})\}}{E\{(Z(\mathbf{x}) - E\{Z\})^2\}}, \quad (3.10)$$

where it is implicitly assumed that the field $Z(\mathbf{x})$ is stationary. Since the random variable $Y(\mathbf{x})$ has a standard normal distribution (with a zero mean and a unity variance), its normalized autocovariance function is the same with its autocorrelation function. Its distribution function $P(y)$ is given by:

$$P(y) = \frac{1}{\sqrt{2\pi}} \int_{-\infty}^y e^{-\frac{y^2}{2}} dy, \quad (3.11)$$

The function G is defined by the following condition. When the random variable Y is equal to y , Z takes the value z :

$$z = \begin{cases} 1 & \text{if } P(y) \leq \varepsilon \\ 0 & \text{otherwise} \end{cases} \quad (3.12)$$

Thus, it is evident that the average value of $Z(\mathbf{x})$ is equal to ε , and that its variance is equal to $\varepsilon - \varepsilon^2$.

The expression of the normalized autocovariance function $R_Z(\mathbf{u})$ of $Z(\mathbf{x})$ as a function of $R_Y(\mathbf{u})$ was derived by Quiblier (1984) and Adler *et al.* (1990). The random vector $Y=(Y(\mathbf{x}), Y(\mathbf{x}+\mathbf{u}))$ is a bivariate Gaussian whose probability density $P_Y(y)$ is given by

$$P_Y(\mathbf{y}) = \frac{1}{2\pi |\mathbf{V}|^{1/2}} \cdot \exp\left[-\frac{1}{2} \cdot \mathbf{y} \cdot \mathbf{V}^{-1} \cdot \mathbf{y}^t\right], \quad (3.13)$$

where \mathbf{V} is the non-negative definite 2×2 covariance matrix

$$\mathbf{V} = \overline{Y(\mathbf{x})Y(\mathbf{x} + \mathbf{u})}. \quad (3.14)$$

The normalized autocovariance function $R_Z(\mathbf{u})$ can be expressed in terms of the function $G(y)$ and of $P_Y(y)$

$$R_Z(\mathbf{u}) = \frac{1}{\varepsilon - \varepsilon^2} \int \int_{-\infty}^{+\infty} G(y_1)G(y_2)P_Y(y_1, y_2)dy_1 dy_2, \quad (3.15)$$

where y_1 and y_2 denote the two components of \mathbf{y} .

In order to evaluate Eq. (3.15), the density $P(y_1, y_2)$ can be expanded in terms of Hermite polynomials which are denoted by $H_m(y)$. After some tedious manipulations, $R_Z(\mathbf{u})$ can be expressed as a series in terms of $R_Y(\mathbf{u})$:

$$R_Z(\mathbf{u}) = \sum_{m=0}^{\infty} B_m^2 R_Y^m(\mathbf{u}). \quad (3.16)$$

where the coefficients B_m are given by

$$B_m = \frac{1}{\sqrt{2\pi m!}} \int_{-\infty}^{+\infty} b(y)e^{-y^2/2} H_m(y) dy, \quad (3.17)$$

together with

$$b(y) = \frac{\varepsilon - 1}{\sqrt{\varepsilon(1 - \varepsilon)}} \text{ if } P(y) \leq \varepsilon, \quad (3.18)$$

$$b(y) = \frac{\varepsilon}{\sqrt{\varepsilon(1 - \varepsilon)}} \text{ if } P(y) > \varepsilon. \quad (3.19)$$

The Hermite polynomials $H_m(y)$ are defined as follows:

$$H_m(y) = (-1)^m e^{y^2/2} \frac{d^m}{dy^m} e^{-y^2/2}. \quad (3.20)$$

When the porosity is given, $R_Y(\mathbf{u})$ can be derived from $R_Z(\mathbf{u})$. This can be solved by numerical method, such as a Newton iterative scheme. When $R_Y(\mathbf{u})$ or $C_Y(\mathbf{u})$ is known, one has to determine the coefficients $a(r, s, t)$ by numerically solving the set of quadratic Equation (see (3.8)). It should be noticed that the solution is not unique and that it is sometimes proved difficult to determine the $a(r, s, t)$.

Once the coefficients $a(r,s,t)$ are known, a porous structure can be reconstructed possessing the same porosity and autocorrelation function. One starts from any arbitrary seed and then generates a set of non-correlated Gaussian variables $X(i,j,k)$. This field is then successively passed through the linear filter Eq. (3.6) and the nonlinear filter Eq.(3.12). The details of this process can be found in the literatures (Adler *et al.*, 1990; Adler, 1992; Fernandes, 1994).

3.4. NEW METHOD BASED ON FOURIER TRANSFORM

3.4.1. Principle

As discussed above, the difficulty of JQA method is to solve the Eq. (3.8). It is a set of nonlinear equations. For L_c larger than 32, it was long, difficult and sometimes impossible to invert the system of Eq. (3.8) numerically (Adler, 1992). Adler (1992) proposed a version using Fourier transform. From a computational point of view, the use of the fast Fourier transform algorithm makes the Fourier transform superior to the JQA method. Application of the Fourier transform method in 3-D is, however, restricted by resident memory requirements. To overcome above problems, an existence theorem (Papoulis, 1965, pp. 350) provides an alternative of generating normal field. The existence theorem is stated as follows:

Given a positive-definite function $R(u)$, i.e., $R(u) \leq R(0)$, $\forall u \in \mathfrak{R}$ and its Fourier transform is positive, we can find a stochastic process having $R(u)$ as its autocorrelation function.

This theorem is usually established by constructing a normal process with $R(u)$. For a Gaussian, normalized field, the autocorrelation function is equal to the normalized autocovariance function. So they will not be distinguished in this work. Given a positive-definite function $R_Y(u)$, one can find a stochastic process $Y(\mathbf{x})$ having $R_Y(u)$ as its autocorrelation function. By definition of Fourier transform and the Wiener-Khinchin theorem (see section 2.3), the Fourier transform of the autocorrelation of a function is the power spectrum of this function, i.e.:

$$\hat{R}_Y(\mathbf{p}) = \mathfrak{F}(R_Y(\mathbf{u})) = |\mathfrak{F}(Y)|^2 = |\hat{Y}|^2. \quad (3.21)$$

Therefore, if the autocorrelation function is known for an arbitrary field $Y(\mathbf{x})$, Fourier transform can be used to generate this field with the same autocorrelation function (Pardo-

Igúzquiza and Chica-Olmo, 1993). In fact, the above equation means that the Fourier transform $\hat{R}_Y(\mathbf{p})$ of $R_Y(\mathbf{u})$ is only related to the magnitude $|\hat{Y}|$ of $\hat{Y} = \mathfrak{F}(Y)$. This means that the phase angle of \hat{Y} does not affect the autocorrelation $\hat{R}_Y(\mathbf{p})$, i.e., any two functions \hat{Y} with the same magnitude $|\hat{Y}|$ and random generated phase angles will give the same autocorrelation $\hat{R}_Y(\mathbf{p})$. In addition to the porosity ε , the only information which must be preserved, in reconstructing, is $R_Y(\mathbf{u})$ or $\hat{R}_Y(\mathbf{p})$. Because this last quantity is only related to $|\hat{Y}|$ and will be necessarily preserved in performing this operation, the phase angle of $\hat{Y} = \mathfrak{F}(Y)$ may be generated at random from a uniform distribution between 0 and 2π . This is the basis of the presently proposed method.

In this way, one first generates the Gauss field $Y(\mathbf{x})$ directly from its autocorrelation function, then uses the truncated method to generate $Z(\mathbf{x})$. The Fourier transform of a real function is hermitian function. Then, its coefficients must be hermitian, this is even real part and odd imaginary part. Using the above properties to calculate the inverse Fourier transform of the complex coefficients, the Gaussian field $Y(\mathbf{x})$ is obtained with the specified autocorrelation model. Finally, $Z(\mathbf{x})$ is generated by truncating $Y(\mathbf{x})$ similarly to nonlinear filter.

3.4.2. Reconstruction Process of 3-D Porous Media

If one wants to generate 3-D porous structure with a $N_x \times N_y \times N_z$ cube from known porosity and autocorrelation function, the reconstruction process based on Fourier Transforms is proposed as follows:

(1) Calculation of $R_Y(\mathbf{u})$ from the measured $R_Z(\mathbf{u})$:

Let's first look at the properties of nonlinear filter given by Eq. (3.16). It follows that

$$R_Z(R_Y, \varepsilon) = R_Z(R_Y, 1 - \varepsilon). \quad (3.22)$$

The limiting case at $\varepsilon=0.5$ is interesting since it can be calculated analytically, which can be shown that (Adler *et al.*, 1990)

$$R_Z = \frac{2}{\pi} \cdot \arcsin(R_Y), \varepsilon = \frac{1}{2}. \quad (3.23)$$

Figure 3.1 represents the comparison of R_Z as a function of R_Y between numerical and analytical values at $\varepsilon=0.5$. It is shown that they are in very good agreement. Therefore, $R_Y(u)$ can be determined numerically. The integral in Eq. (3.16) is evaluated for y ranging from -10 to +10. The series in Eq. (3.17) is limited to a maximum value $m=M$. In the present work, M is assigned to 30 for $R_Y \leq 0.9$. For $R_Y > 0.9$, the following approximate equation is used due to the precision requirement:

$$R_Z = 1 - a_1(1 - R_Y)^{1/2}. \quad (3.24)$$

The constant a_1 depends on the porosity ε . It is determined by comparing the above equation with the numerical data at $R_Y=0.9$. The validity of this equation was checked by Adler *et al.* (1990).

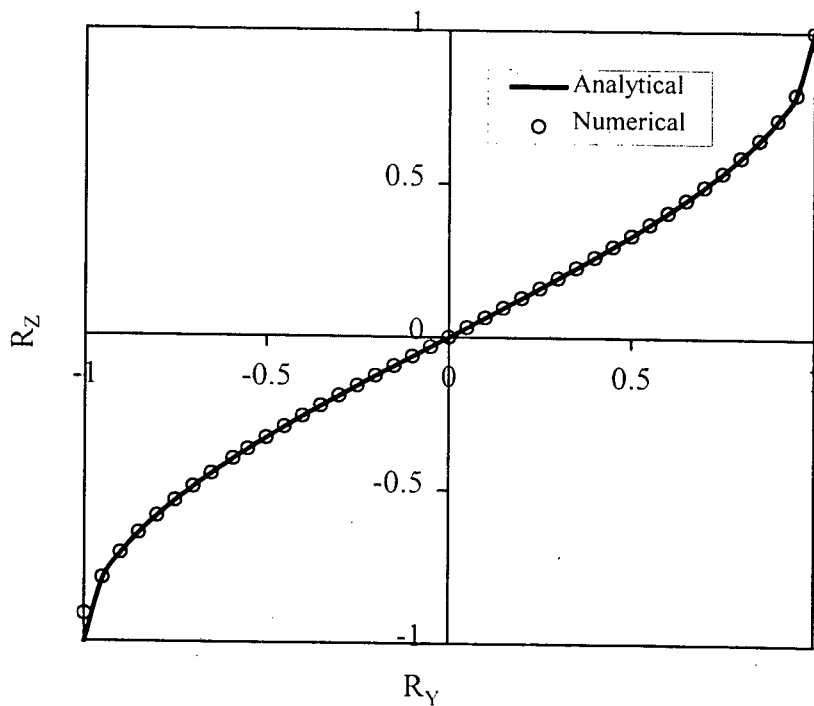


Figure 3.1 - Comparison of R_Z as a function of R_Y between numerical and analytical values at $\varepsilon=0.5$.

For $0 \leq i \leq \frac{N_x}{2}, 0 \leq j \leq \frac{N_y}{2}, 0 \leq k \leq \frac{N_z}{2}$, the 3-D $R_Y(i,j,k)$ is obtained from $R_Y(u)$ using

$R_Y(i,j,k) = R_Y(\sqrt{i^2 + j^2 + k^2}) = R(u)$ and interpolating for non-integer displacements. Otherwise, the symmetric properties of normalized autocovariance function is used due to the isotropic property.

(2) Power spectrum and Fourier spectrum:

By definition, the power spectrum is the Fourier transform of the autocorrelation function. We use an algorithm, which is a nice split-radix, n-dimensional, fast-Fourier transform by Singleton (1969), to calculate the Fourier transform of $R_Y(i,j,k)$. It is shown that this code is significantly faster than the routine represented by Press *et al.* (1986) (e.g., 25 vs. 36 seconds for a 1024×1024 floating point matrix, Beale, 1997). The other advantage is that the size of sample is not limited only as power of two. The algorithm is shown in Appendix A. Fourier spectrum is obtained from the power spectrum, which is the square root of power spectrum.

(3) Phase angle:

The generation of phase angle is taken at random from a uniform distribution between 0 and 2π . We first generate random variables uniformly distributed between 0 and 1 by a random generator (Press *et al.*, 1986). Then the phase angle is equal to the product of them and 2π .

(4) Complex Fourier coefficients:

The Fourier transform $\hat{f}(\mathbf{p})$ of a real function $f(\mathbf{x})$ is a hermitian function. Then, real part is even and imaginary part is odd. Figure 3.2 shows the arrangement of the complex $\hat{f}(i,j)$ of Fourier transform in 2-D. It has been verified by direct computation. In this figure, the different sectors of Fourier coefficients are represented by different Greek letters. The matrix size is $N_x \times N_y$. Sectors α, χ, ψ, η are real and the rest are complex sectors.

This symmetry can be expressed:

$$\text{First row:} \quad \hat{f}(i,0) = \hat{f}^*(N_x-i,0)$$

$$\text{First column:} \quad \hat{f}(0,j) = \hat{f}^*(0, N_y-j)$$

$$\begin{aligned}
N_x/2 \text{ row:} & \quad \hat{f}(i, N_y/2) = \hat{f}^*(N_x-i, N_y/2) \\
N_y/2 \text{ column:} & \quad \hat{f}(N_x/2, j) = \hat{f}^*(N_x/2, N_y-j) \\
\text{Rest of rows and columns:} & \quad \hat{f}(i, j) = \hat{f}^*(N_x-i, N_y-j)
\end{aligned} \tag{3.25}$$

where $i \in [1, N_x/2-1]$, and $j \in [1, N_y/2-1]$.

	0	$N_x/2$	N_x-1
0	α	β	β^*
	δ	ϵ	γ
$N_y/2$	η	ν	ν^*
N_y-1	δ^*	γ^*	ϵ^*

Figure 3.2 - Arrangement of the complex Fourier coefficients in 2-D.
The matrix size is $N_x \times N_y$. *: complex conjugate.

The arrangement of the complex discrete Fourier coefficients for a matrix size $N_x \times N_y \times N_z$ in 3-D is shown in Figure 3.3. It has been verified by direct computation. The different sectors of Fourier coefficients are represented by different Greek letters. At $k=0$ and $k=\frac{N_z}{2}$ there is an arrangement that is the same as the arrangement of coefficients in 2-D shown in Figure 3.2. The coefficients in $k \in [1, \frac{N_z}{2}-1]$ are the complex conjugates of coefficients in $k \in [\frac{N_z}{2}+1, N_z-1]$, according to what is shown in Figure 3.3 and that can be expressed analytically:

$$\begin{aligned}
\hat{f}(0, 0, k) &= \hat{f}^*(0, 0, N_z-k) \\
\hat{f}(0, \frac{N_y}{2}, k) &= \hat{f}^*(0, \frac{N_y}{2}, N_z-k) \\
\hat{f}(\frac{N_x}{2}, 0, k) &= \hat{f}^*(\frac{N_x}{2}, 0, N_z-k) \\
\hat{f}(\frac{N_x}{2}, \frac{N_y}{2}, k) &= \hat{f}^*(\frac{N_x}{2}, \frac{N_y}{2}, N_z-k) \\
\hat{f}(0, j, k) &= \hat{f}^*(0, N_y-j, N_z-k) \\
\hat{f}(0, N_y-j, k) &= \hat{f}^*(0, j, N_z-k) \\
\hat{f}(i, 0, k) &= \hat{f}^*(N_x-i, 0, N_z-k) \\
\hat{f}(N_x-i, 0, k) &= \hat{f}^*(i, 0, N_z-k) \\
\hat{f}(\frac{N_x}{2}, j, k) &= \hat{f}^*(\frac{N_x}{2}, N_y-j, N_z-k) \\
\hat{f}(\frac{N_x}{2}, N_y-j, k) &= \hat{f}^*(\frac{N_x}{2}, j, N_z-k) \\
\hat{f}(i, \frac{N_y}{2}, k) &= \hat{f}^*(N_x-i, \frac{N_y}{2}, N_z-k) \\
\hat{f}(N_x-i, \frac{N_y}{2}, k) &= \hat{f}^*(i, \frac{N_y}{2}, N_z-k) \\
\hat{f}(i, j, k) &= \hat{f}^*(N_x-i, N_y-j, N_z-k) \\
\hat{f}(i, N_y-j, k) &= \hat{f}^*(N_x-i, j, N_z-k) \\
\hat{f}(N_x-i, j, k) &= \hat{f}^*(i, N_y-j, N_z-k) \\
\hat{f}(N_x-i, N_y-j, k) &= \hat{f}^*(i, j, N_z-k).
\end{aligned} \tag{3.26}$$

where $i \in [1, \frac{N_x}{2}-1]$, $j \in [1, \frac{N_y}{2}-1]$ and $k \in [1, \frac{N_z}{2}-1]$.

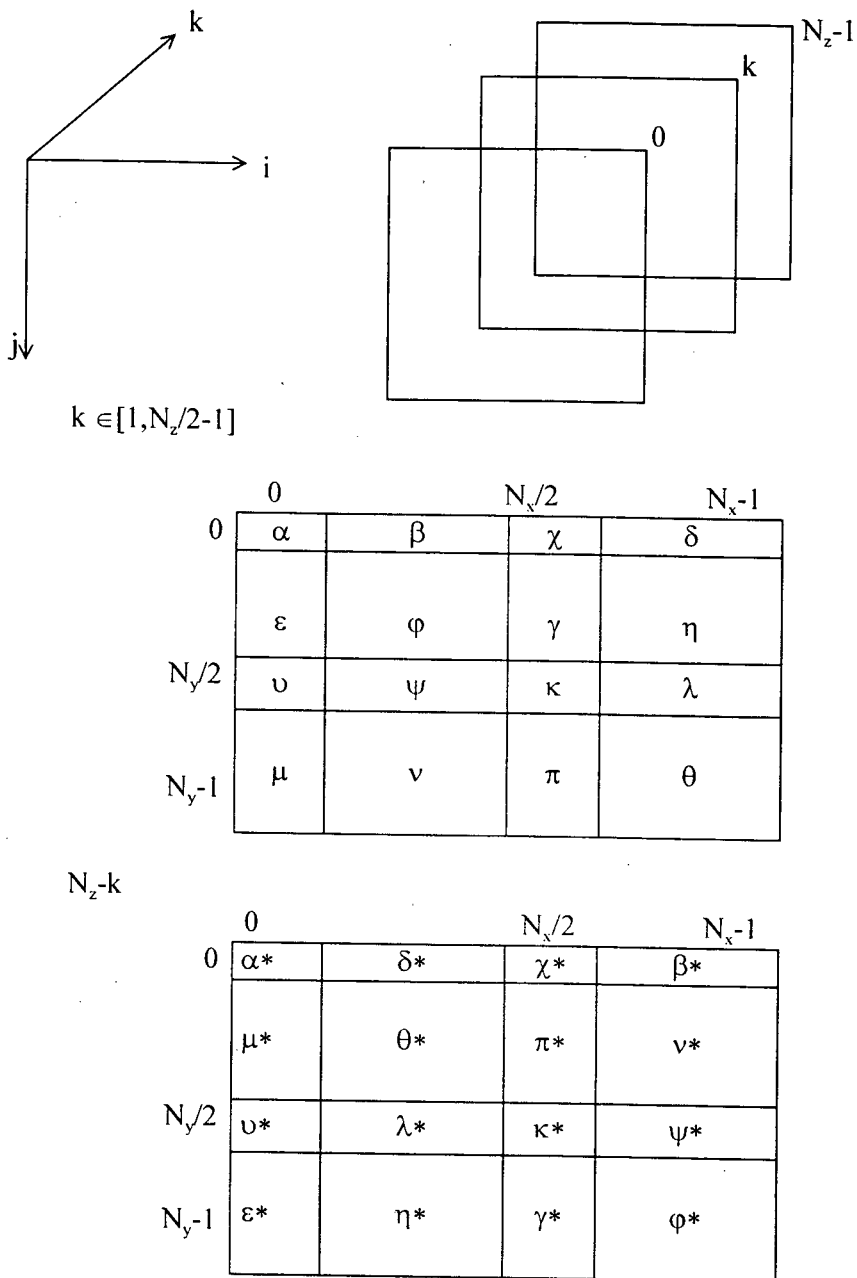


Figure 3.3 - Arrangement of the complex Fourier coefficients in 3-D. The matrix size is $N_x \times N_y \times N_z$. *: complex conjugate.

(6) Inverse Fourier transform:

By calculating the inverse Fourier transform of $\hat{f}(f_x, f_y)$, the discrete Gaussian field $Y(\mathbf{x})$ is obtained with the specified normalized autocovariance function $R_Y(u)$. The inverse

discrete Fourier transform is computed with the above mentioned algorithm of the fast Fourier transform by Singleton (1969).

(7) Nonlinear filter:

Nonlinear filter operation is the same with one used by Adler *et al.* (1990) and Fernandes (1994). $Z(\mathbf{x})$ is obtained using Eq. (3.12).

3.5. EXAMPLES AND DISCUSSIONS

In order to verify the above reconstruction method, a plane section of Fontainebleau sandstone GF2 used by Adler *et al.* (1990) was selected. Figure 3.4 shows a digital picture of this section taken with an electron scanning microscope. Each pixel corresponds to $3.8 \mu\text{m}$. The porosity is 0.25 and the normalized autocovariance function is shown in Figure 3.5 (Adler *et al.*, 1990). The new method proposed in section 3.4 was used to generate 3-D porous structure for GF2 sample. Figure 3.6 shows a cross section of the reconstructed porous structure. It has the same features as the plane section of the real sample (see Figure 3.4).

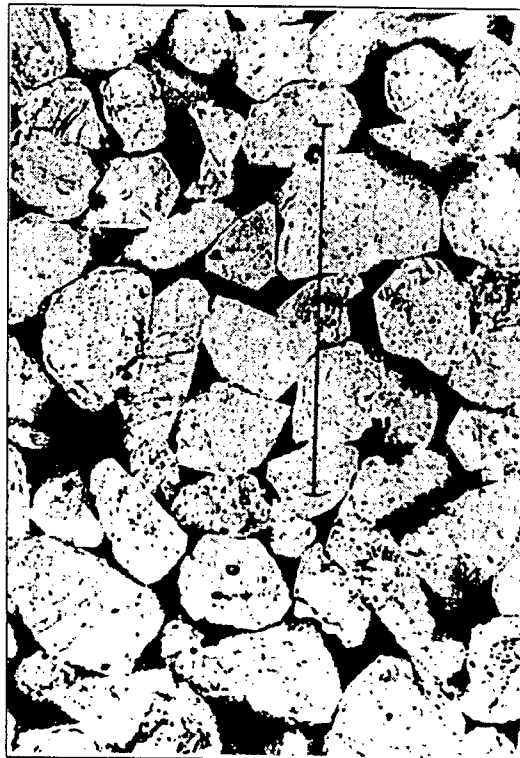


Figure 3.4 - A plane section of the Fontainebleau Sandstone GF2 (Adler *et al.*, 1990). Pore space appears in black.

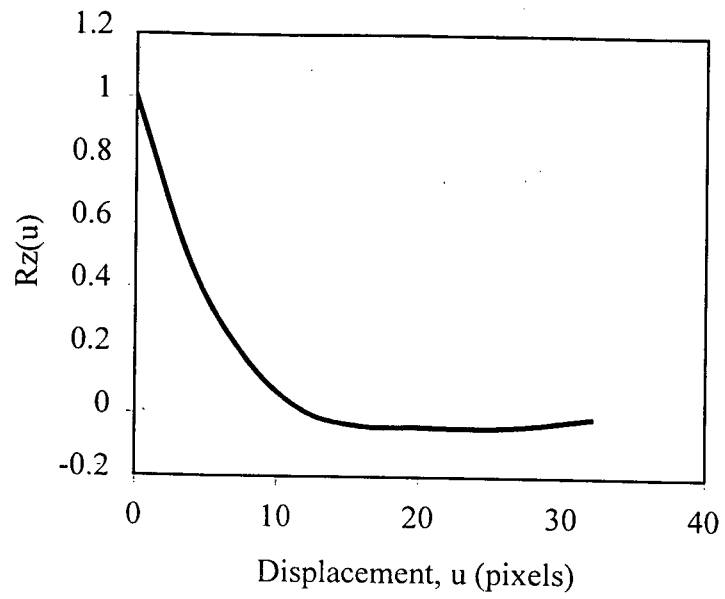


Figure 3.5 - Experimental $R_z(u)$. The length scale α is equal to $3.8 \mu\text{m}$ per pixel.

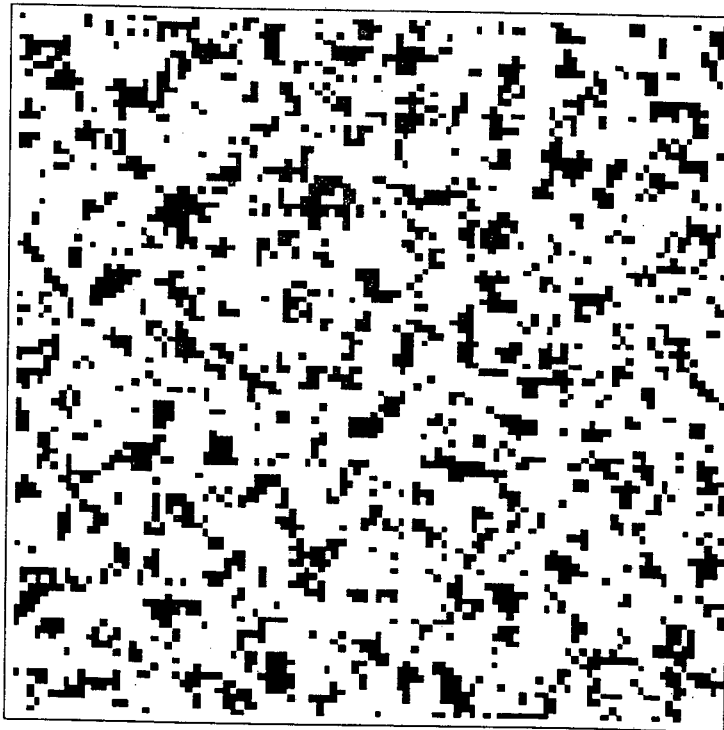


Figure 3.6 - A reconstructed cross section for GF2 sample (size 100×100 , $\varepsilon = 0.25$, $n=4$ and $\zeta=8$).

3.5.1. Comparison of the Results with JQA Method

The statistical properties for the reconstructed porous structure were compared with the results obtained by Adler *et al.* (1990). They are shown in Table 3.1 and Figure 3.7. It can be seen that, in general, the porosity and autocorrelation function reconstructed by new method are better than the previous one. The most important advantage that the new method distinguishes from the old one is time saving. For instance, it takes about 8 hours to generate the 100^3 size in the workstation IBM RISC System /6000-410 by previous JQA method; but it only needs about 5 minutes using new method.

Table 3.1 : Statistical properties of reconstructed porous media and comparison with results of Adler *et al.* (1990). Data are for Image GF2, $\zeta=8$, $n=4$ and $N=20$ (Adler *et al.*, 1990)

Displacements (μm)	Sample C(u)	Reconstructed C(u) for 1 configuration		Reconstructed C(u) for 5 configurations	
		this work	Adler <i>et al.</i> (1990)	this work	Adler <i>et al.</i> (1990)
0	0.2500	0.2510	0.2700	0.2503	0.2500
15.2	0.1497	0.1420	0.1716	0.1422	0.1456
30.4	0.0931	0.0932	0.1150	0.0938	0.0897
45.6	0.0636	0.0688	0.0855	0.0680	0.0644
60.8	0.0554	0.0612	0.0703	0.0609	0.0565
76.0	0.0546	0.0596	0.0612	0.0600	0.0561
91.2	0.0541	0.0577	0.0606	0.0585	0.0539
106.4	0.0561	0.0597	0.0648	0.0597	0.0597
121.6	0.0604	0.0604	0.0717	0.0627	0.0627
$\bar{\varepsilon}$	0.25	0.2510	0.27	0.2503	0.25

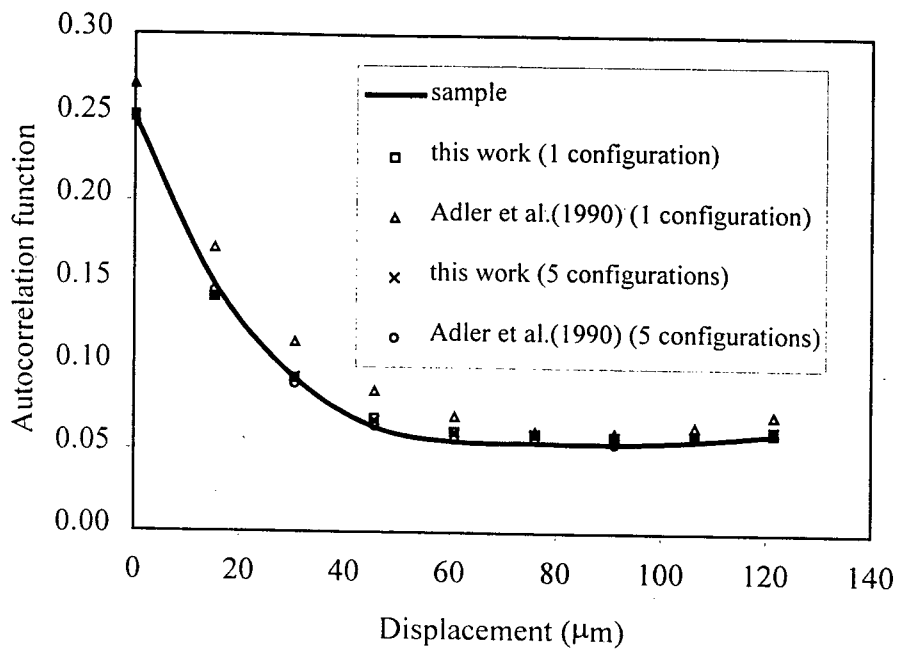


Figure 3.7 - Comparison of $C_z(u)$ between this work and Adler *et al.* (1990). Data are same with Table 3.1.

3.5.2. Effects of Reconstruction Parameters on the Results

For a given section of a porous sample, the correlation length λ is defined by $\lambda = \int_0^{\infty} R_z(u) du$ (Lantuéjoul, 1991; Ioannidis *et al.*, 1996). The length per pixel is noted as α . Due to computer storage limitations, it is not always possible to take into account every point where R_Y was calculated when one uses the original normalized autocovariance function $R_Z(u)$. Usually one point is selected for every n points. If n is larger than 1, it is called amplification factor. Let ζ be the number of points where correlation is to be calculated in reconstructing the porous structure. For instance, $R_Y(u=0)$, $R_Y(u=n)$, $R_Y(u=2n)$,, $R_Y(u=\zeta n)$ are used. A cube is generated when one reconstructs the porous media and usually, the size of cube is $N_x=N_y=N_z=N$. Therefore, the length of a cube L is $n\alpha N$. The role of these parameters n , ζ and N can be summarized as follows:

As the autocorrelation function is even, to prevent any overlap between the negative and positive values of the displacement distance u through the spatial periodicity, L should be larger than $2n\alpha\zeta$, i.e.:

$$L \gg 2n\alpha\zeta, \quad (3.27)$$

or

$$\zeta \ll N/2. \quad (3.28)$$

If $N/2$ is much larger than ζ , one expects statistical fluctuations to diminish. The maximum sample distance $n\alpha\zeta$ must be larger than λ , i.e.

$$\zeta \gg \frac{\lambda}{n\alpha}. \quad (3.29)$$

It is also natural to require that the number of points of the autocorrelation function to be used in reconstructing the porous structure be as large as possible, i.e.:

$$1 \ll \zeta. \quad (3.30)$$

The above conditions can be summarized up by the following inequalities:

$$1 \ll \frac{\lambda}{n\alpha} \ll \zeta \ll N/2. \quad (3.31)$$

Therefore, the larger is the size N , the better is the result. However, increasing N requires larger computer storage capacity and more running time.

In order to illustrate the effects of these parameters, a simple model of normalized autocovariance function for Berea sandstone (Ioannidis *et al.*, 1995)

$$R_z(u) = e^{-u/6}. \quad (3.32)$$

and $\varepsilon=0.225$ was used to reconstruct the porous structure. Table 3.2 and Figure 3.8 show the effects of parameter n and ζ on the porosity and autocorrelation function, respectively. Under the same lengths of reconstructed structure, the best comparison was obtained for the smaller n . Table 3.3 and Figure 3.9 gives the effects of size N on the results. When N increases, the better results are achieved. Table 3.3 also shows running time at the workstation IBM RISC System /6000-410.

Table 3.2 : Effects of n and ζ on porosity ($\epsilon=0.225$ and $nN = 120$).

n	ζ	N	Average of $Z(x)$ (porosity)
1	60	120	0.2265
2	30	60	0.2250
3	20	40	0.2282
4	15	30	0.2220
5	12	24	0.2244
6	10	20	0.2245
7	8	17	0.2220

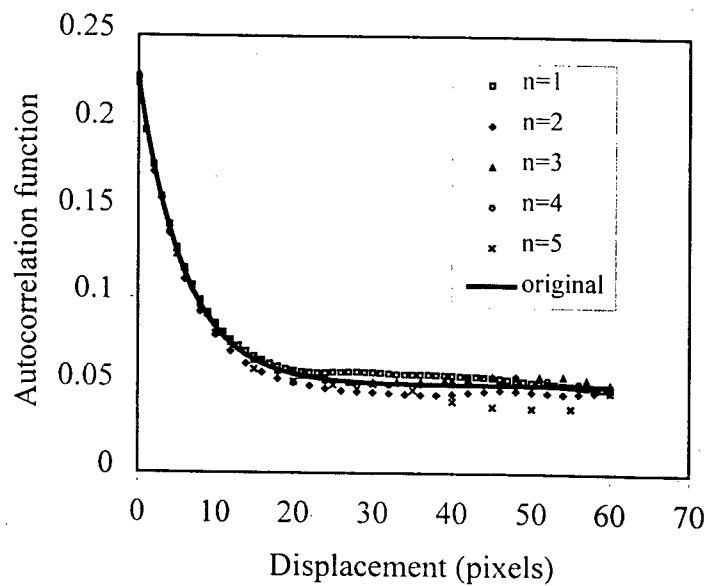
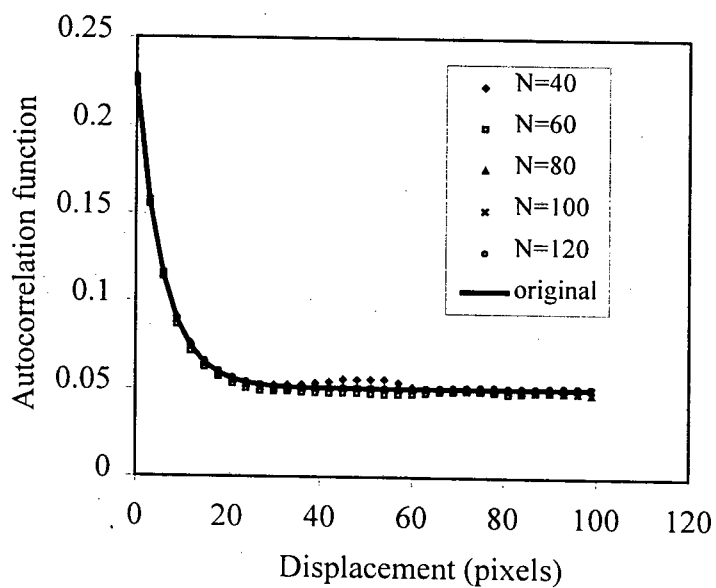
Figure 3.8 - Effects of n and ζ on autocorrelation functions ($\epsilon=0.225$ and $nN = 120$).

Table 3.3 : Effects of N on porosity ($\epsilon=0.225$, $n=3$ and $\zeta=20$).

N	Average of Z(x) (porosity)	CPU time (seconds)
40	0.2282	11
60	0.2250	20
80	0.2264	46
100	0.2244	98
120	0.2251	207

Figure 3.9 - Effects of N on autocorrelation function ($\epsilon=0.225$, $n=3$ and $\zeta=20$).

3.5.3. Effects of Phase Angle on the Results

Phase angles are associated with the position of a spatial waveform in relation to the edge of the image. Since the phase angle is taken at random from an uniform distribution between 0 and 2π , phase angle distribution is controlled by a random generator. As shown in Table 3.4 and Figure 3.10, when the seeds are changed, the porosity and the normalized autocovariance functions of $Z(x)$ are almost constant. Phase angle does not affect the autocorrelation function (see section 3.4.1). So this algorithm is not sensitive to random numbers. Figure 3.11 shows the cross sections generated by different phase angle distributions for the sample GF2. These images possess the similar patterns. The only difference is the position of patterns.

Table 3.4 : Effects of random generator on the results ($\epsilon=0.225$, $n=3$, $\zeta=20$ and $N=60$).

Seed number	Average of $Z(x)$ (porosity)	Running time (seconds)
-100	0.2250	24
-200	0.2254	26
-300	0.2247	26
-400	0.2263	25
-500	0.2246	25
Average	0.2252	25.2

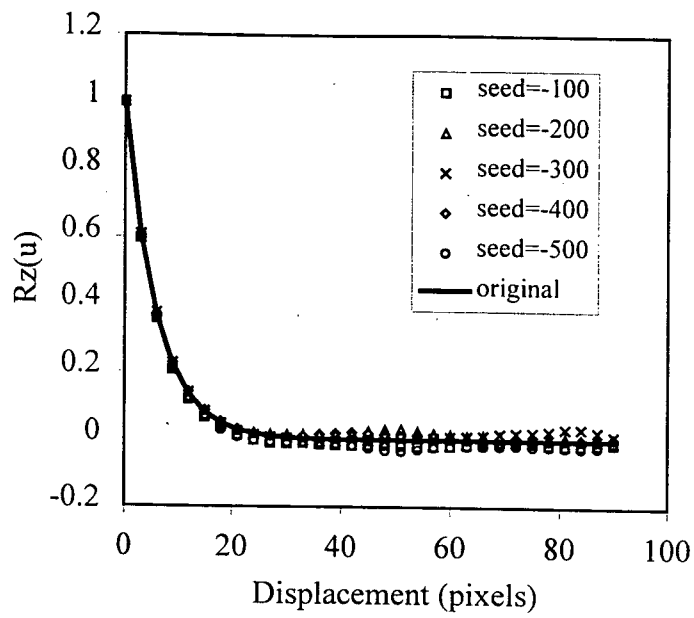
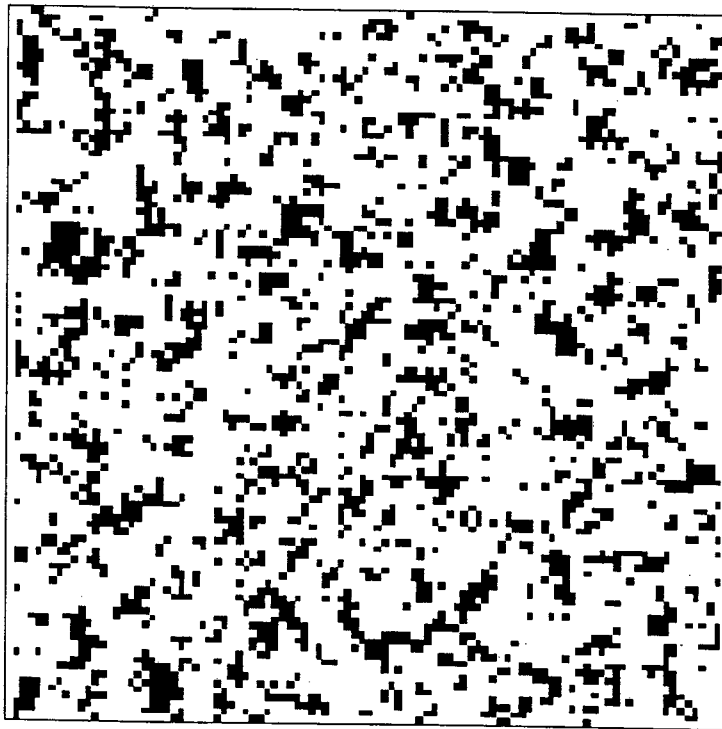
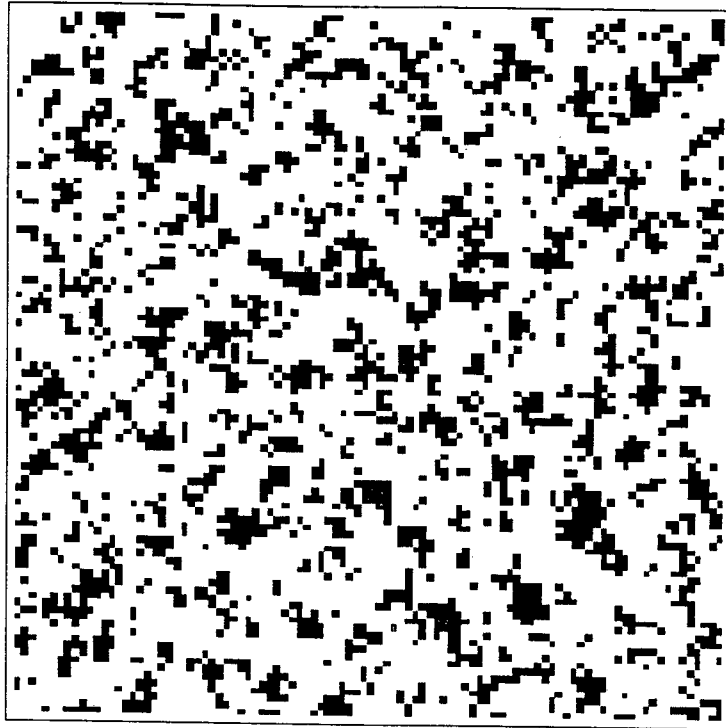


Figure 3.10 - Comparison of normalized autocovariance function for different seeds.

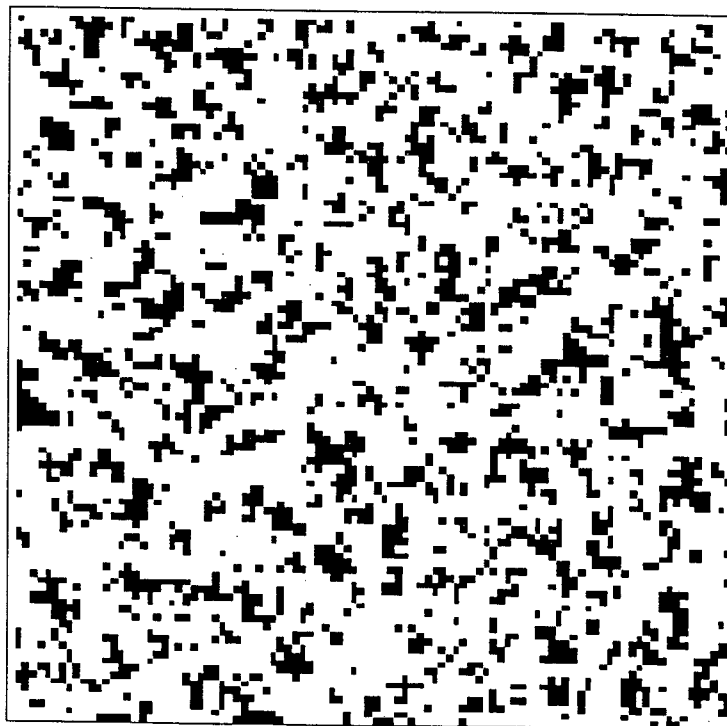


(a)

Figure 3.11 - Cross sections generated by different phase angle distributions (a) seed=-9 (b) seed=-100 (c) seed=-200. Other data are same with Figure 3.6.



(b)



(c)

Figure 3.11 (Continued).

4. VISUALIZATION AND CHARACTERIZATION OF 3-D POROUS STRUCTURE

4.1. INTRODUCTION

As discussed in chapter 1, characterization of 3-D porous structure is an important aspect in the study of porous media. This is difficult because real porous media are three-dimensional and possess a very complex geometry. Moreover, it is desirable to be able to quantify the geometry by a few parameters. The definitions and properties are often divided into two groups (Adler, 1992). The first group consists of the intrinsic properties that do not depend on the geometry of the medium, i.e., on the phase function. The second group depends on a model in which the medium is supposed to be made of grains, and one wants to characterize the size distribution of these grains. Apart from the intrinsic interest, the detailed geometrical structure is helpful for analyzing transport processes through these media. Connectivity is important when flow problems are considered. For instance, dead ends play an important role in diffusional processes, while being irrelevant for permeability on physical grounds.

Most studies of the geometrical properties of porous media have been 2-D section investigations. Although this is known to give reasonable results for size distribution and cross-sectional shapes, it provides no information on connectivity in 3-D. Kwiecien *et al.* (1990) developed a software for partitioning the irregular, interconnected pore space of a porous medium into its constituent pores. The 3-D reconstruction of porous media was carried out from serial section data for a Berea sandstone sample. Output includes the sizes of the individual pores and necks, the order in which the pores and necks are connected, and the degrees of interconnection. Thovert *et al.* (1993) characterized the reconstructed structure of a porous medium and quantified it by a few parameters, such as connected and percolating components, and graph of the pore space. Various algorithms, based on pseudo-diffusion processes, were proposed to determine the connected and percolating components of the pore

space. The graph of the pore space (skeleton) was obtained by the homotopic thinning and skeletonizing algorithms, respectively. The topological characteristics, such as the number of loops, were derived. Systematic applications of these algorithms were illustrated on computer reconstruction of various sandstones.

The skeleton of an object is often obtained by thinning algorithm. Thinning is a preprocessing operation of pattern recognition since a thinned object is easier to trace and hence is easier to recognize. Generally, thinning is a layer-by-layer erosion of an object until only a unit-width skeleton is left. Thinning has been used in 2-D images for recognizing fingerprints, scanned-in letters and characters, etc., and in 3-D images for recognizing DNA structures and human organs, etc. Many 2-D thinning algorithms have been proposed (see chapter 2, e.g., Zhang and Suen, 1984; Sanniti di Baja, 1994). Pieritz (1994) used median line graph technique to characterize 2-D porous sections. However, the proof for a 3-D thinning algorithm to preserve connectivity is much more difficult than in the 2-D case. This problem was solved by Ma (1994). Recently, Ma (1995) used his results and proposed a 3-D fully parallel thinning algorithm, which preserves connectivity, i.e., the skeleton has the same topology of the original object.

The skeleton gives a simplified graph of 3-D porous structures. If one knows the 3-D porous structure of a real or reconstructed porous medium, one can get the real network of the medium by means of skeleton. For flow in the porous medium, the normal hydraulic radii for all points of the graph are needed. In this chapter, visualization of the 3-D porous structure is first introduced (section 4.2). Then basic concepts for 3-D discrete topology, 3-D thinning algorithms and examples of skeleton extraction are given in section 4.3. Sections 4.4 and 4.5 show the graph of 3-D porous structure and calculation of hydraulic radius that will be used to predict the permeability in the next chapter.

4.2. VISUALIZATION OF THE 3-D POROUS STRUCTURE

Scientific visualization is an extremely useful tool for examining complex 3-D data and models by converting them to a graphical representation. Two visualization techniques for three-dimensional scalar data sets are: (i) *surface rendering* and (ii) *volume rendering*. Rendering is the process of conversion of geometric primitives, such as polygons and spheres, to an image that can be displayed. Surface fitting algorithms use a threshold value to convert a three-dimensional data set in a surface representation consisting of polygons. This can then be

rendered to indicate where values of the chosen threshold value are present. Surface rendering of scalar data can be done by using scalar glyphs, cutting planes, orthogonal slicers or isosurfaces. After the geometric representation of the fitting isosurface has been constructed, rendering algorithms together with rendering hardware can be used to quickly display images. Volume rendering techniques work directly on the whole three-dimensional data set and avoid problems related to determining how a voxel contributes to a surface representation, but are more computer intensive. The algorithm typically uses color (brightness) and opacity (light attenuation) values to expose a range of data values and to make other parts transparent. Surface fitting algorithms are faster than direct volume rendering algorithms since the polygons which describe the surface have to be constructed only once, after which the viewing and lighting parameters can be changed interactively.

Generally, there are three different approaches to make visualization. First, a graphics library can facilitate constructing a personal tailor-made visualization program. This approach requires programming skills and exact knowledge of what has to be visualized upfront. A second approach are turnkey visualization packages which are user-friendly but limited in their functionality because private extensions and reprogramming are not possible. A third class of visualization programs, the so-called application builders, offers many advantages and solves the limitations of the two above approaches. This software is data-driven, using filtering, mapping and rendering operations. It is designed to be flexible for programmers and non-programmers and, therefore, it uses modules, which can be connected interactively to make a visualization application.

In the present work, COI-LIB (Maliska Júnior, 1996) and IDL (Research System, Inc., 1997) are used to visualize the generated 3-D porous structure. COI-lib TM 1.0, Classes & Objects for Interfacing, is a C++ library for the X Window System TM that implements a full-featured object oriented interface with 3-D support. IDL 5.0 (Interactive Data Language) is a software belonging in the third approach to make visualization. IDL's features include: advanced image processing, interactive 2-D and 3-D graphics, insightful volume visualization, a high-level programming language, integrated mathematics and statistics, flexible data I/O, a cross-platform GUI (Graphical User Interfaces) toolkit, and versatile program linking tools.

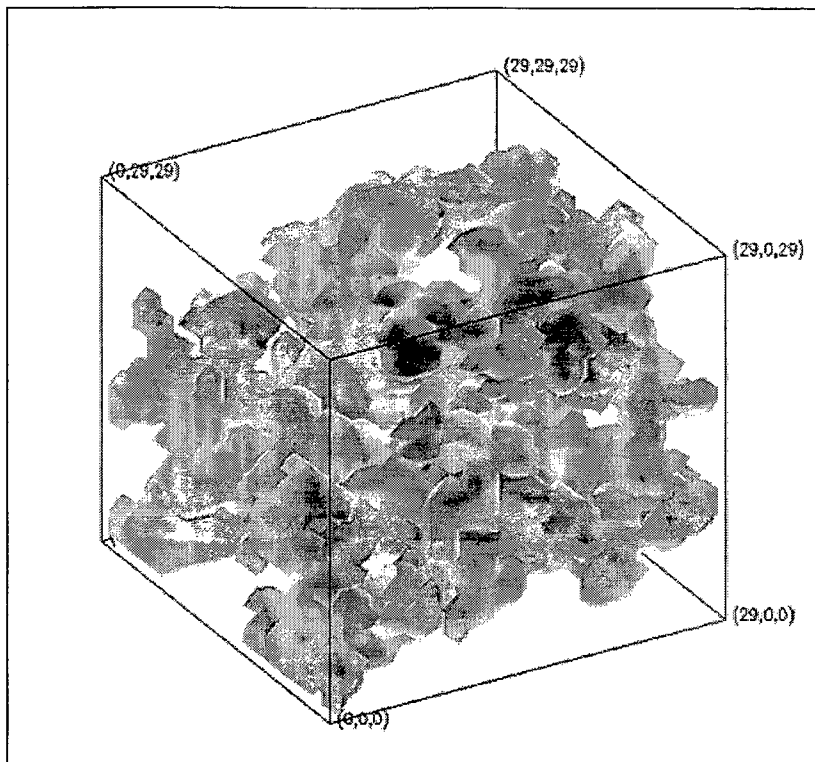


Figure 4.1 - Isosurface of a reconstructed porous structure for sample GF2.

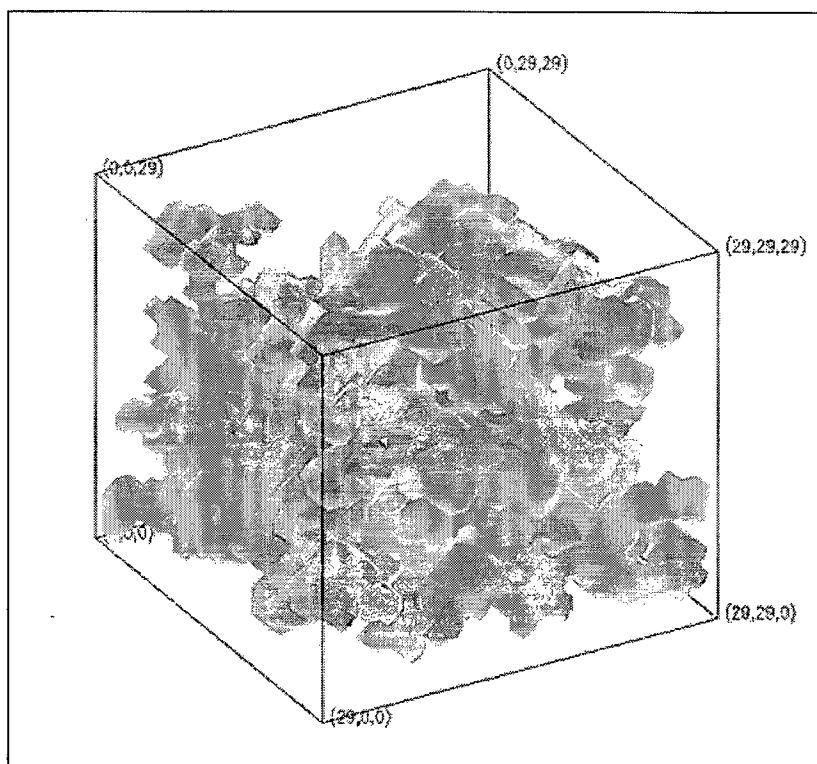


Figure 4.2 - Isosurface of a reconstructed porous structure in Figure 4.1 rotated 60 degrees.

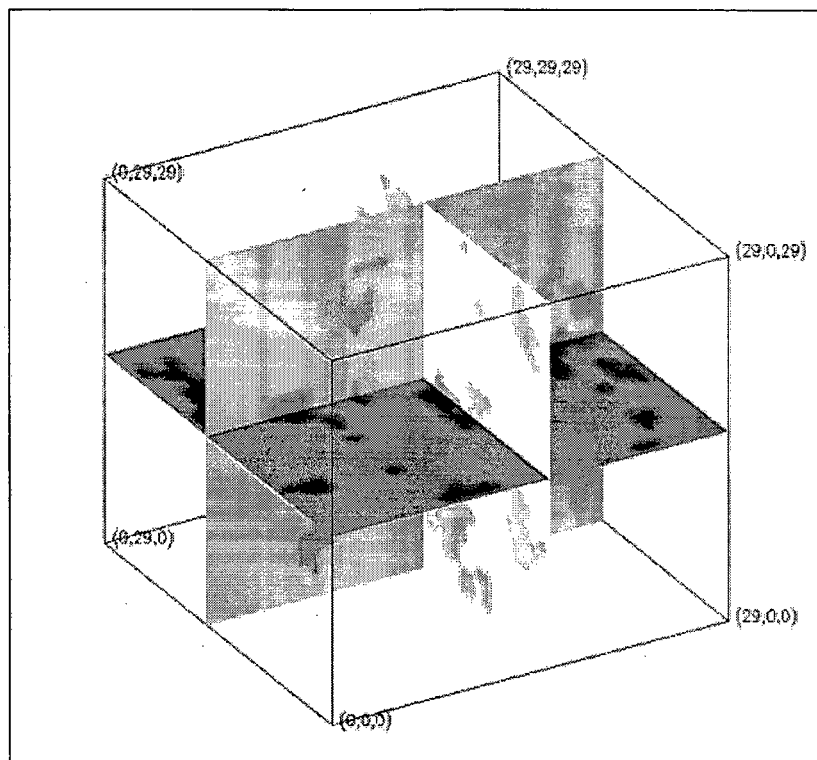


Figure 4.3 - Slice display of a reconstructed porous structure in Figure 4.1 by three orthogonal direction.

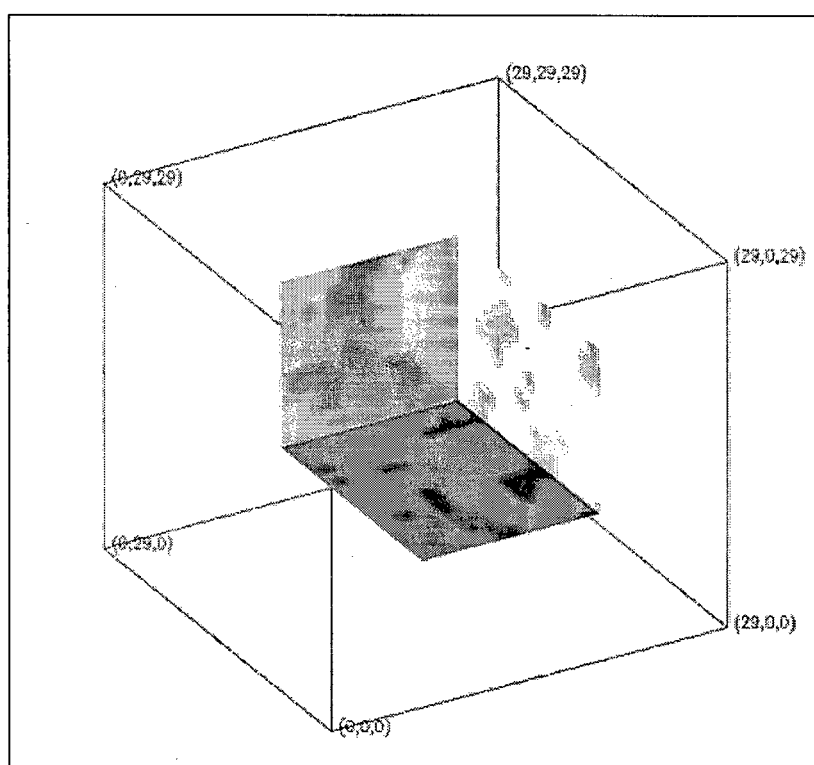


Figure 4.4 - Cutout display of a reconstructed porous structure in Figure 4.1.

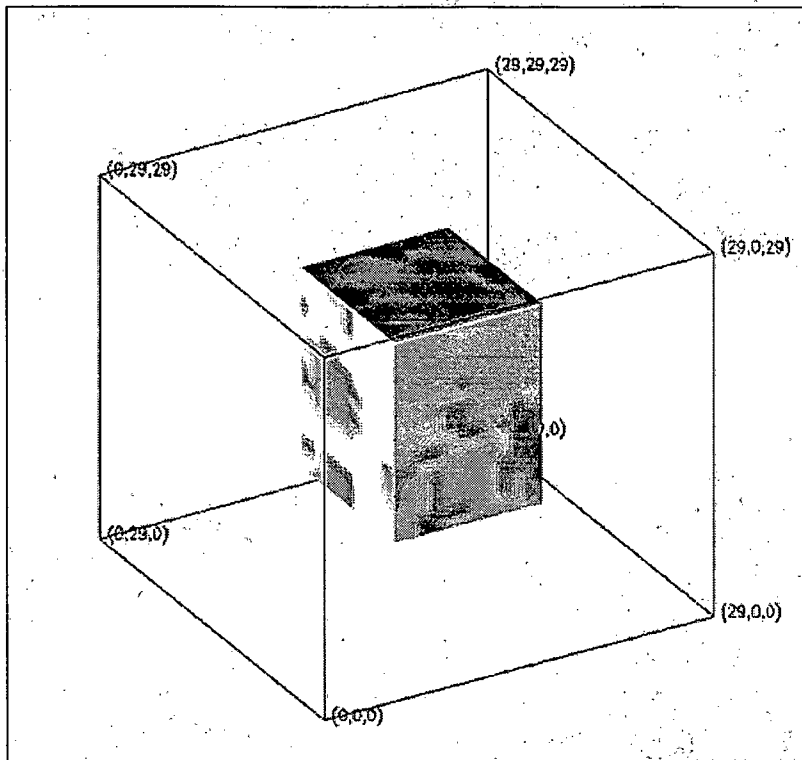


Figure 4.5 - Block display of a reconstructed porous structure in Figure 4.1.

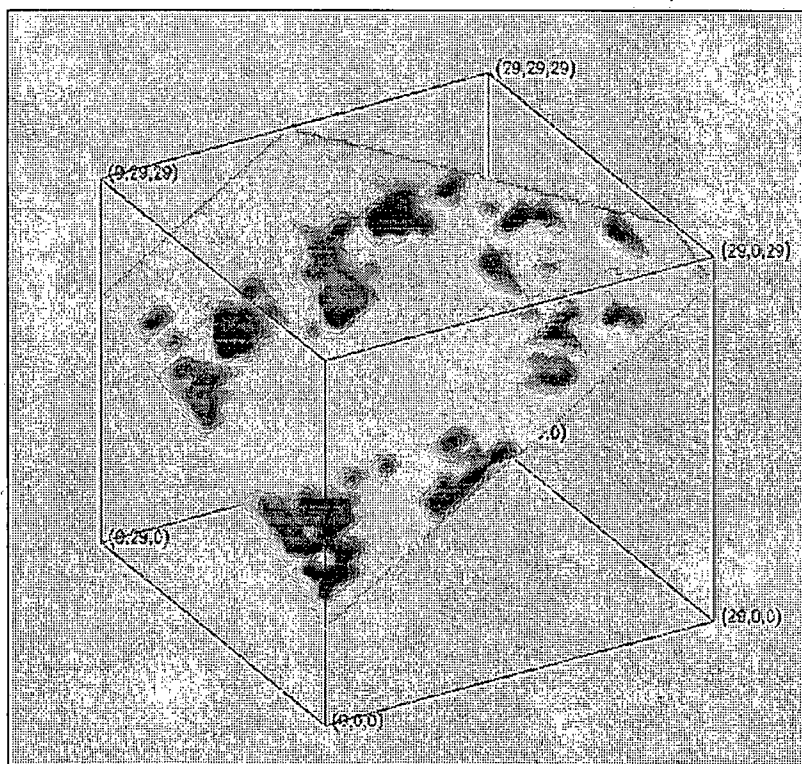


Figure 4.6 - Oblique slice display of a reconstructed porous structure in Figure 4.1 by any direction.

Figure 4.1 shows the isosurface display of a reconstructed porous structure for sample GF2 by IDL. Figure 4.2 - Figure 4.6 show the isosurface representation rotated 60 degrees, a slice display by three orthogonal planes, the cutout display, the block display and an oblique slice display, respectively, of the reconstructed porous structure shown in Figure 4.1.

4.3. THE SKELETON OF 3-D OBJECT

4.3.1. Basic Concepts for 3-D Discrete Topology

In a 3-D discrete space Z^3 , the *distance* function between two distinct points p and q with coordinates (x_p, y_p, z_p) and (x_q, y_q, z_q) is defined as:

$$d(p, q) = \sqrt{(x_q - x_p)^2 + (y_q - y_p)^2 + (z_q - z_p)^2} \quad (4.1)$$

The points p and q are *6-adjacent* if $d(p, q) = 1$, *diagonally adjacent* if $d(p, q) = \sqrt{2}$, and *diametrically adjacent* if $d(p, q) = \sqrt{3}$. An example of 6-adjacent, diagonally adjacent and diametrically adjacent paths is given in Figure 4.7. Furthermore, they are *18-adjacent* if they are 6- or diagonally adjacent, and *26-adjacent* if they are 18- or diametrically adjacent. The point p is a *k-neighbor* of q , if they are k -adjacent. The *k-neighborhood* of p is the set of p and all points that are k -adjacent to p . Define $N(p)$ to be the 26-neighborhood of p . A *unit lattice square* is a set of four corners of a unit square embedded in Z^3 . A *unit lattice cube* is a set of eight corners of a unit cube embedded in Z^3 .

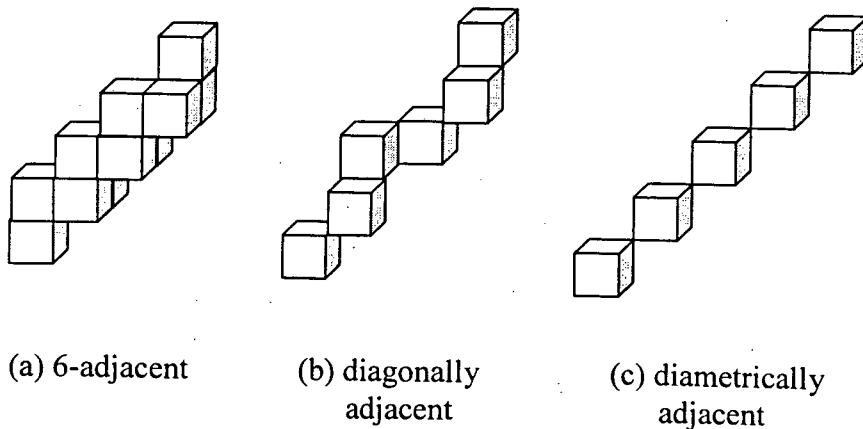


Figure 4.7 - 6-adjacent, diagonally adjacent and diametrically adjacent paths.

For a 3-D binary digital image (or briefly a 3-D image) in Z^3 , each element is assigned either a value 1 (a black point) or a value 0 (a white point). Two black points of a 3-D image are *adjacent* if they are 26-adjacent. Two white points, or one white point and one black point of a 3-D image are adjacent if they are 6-adjacent. By “ $p=1$ ” we mean that the point p is a black point, and by “ $p=0$ ” we mean that p is a white point. Two black points p and q are *connected* if there exists a sequence of black points from p to q such that every pair of consecutive points in the sequence are adjacent. Let P be a set of points of a 3-D image. A *black component* on P is the maximal 26-connected subset of the set of black points of P . A *white component* on P can be defined similarly. A black point in a 3-D image is called a *border point* if it is 6-adjacent to a white point of a 3-D image. The definitions of edge points, simple points and simple sets are as follows.

Definition 4.1 Let p be a black point of a 3-D image. Then p is called an *edge point* if p has exactly one black 26-neighbor in $N(p)$ or in any of three orthogonal 3×3 planes containing p ; p is called a non-edge point if it is not an edge point.

Definition 4.2 Let p be a black point of a 3-D image. Then p is called *simple* if

- 1) p is 26-adjacent to only one black component in $N(p) - \{p\}$; and
- 2) p is 6-adjacent to only one white component in p 's 18-neighborhood.

Definition 4.3 Let D be a set of black points of a 3-D image. Then D is called *simple* if it can be ordered as a sequence for which every point is simple after all previous points in the sequence are deleted (i.e., change to white points).

4.3.2. Thinning Algorithm

A thinning algorithm should preserve connectivity, i.e., an object and its skeleton should maintain the same connected structure. Ma (1994) proposed sufficient conditions for providing a 3-D thinning algorithm to preserve connectivity. We state Ma's results as follows:

Theorem 4.1 A 3-D thinning algorithm preserves connectivity if all of the following conditions hold:

- 1) Only simple points can be deleted.
- 2) If two black corners, p and q , of a unit lattice square are deleted, then $\{p, q\}$ is simple.

- 3) If three black corners, p , q and r , of a unit lattice square are deleted, then $\{p, q, r\}$ is simple.
- 4) If four black corners, p , q , r , and s , of a unit lattice square are deleted, then $\{p, q, r, s\}$ is simple.
- 5) No black components contained in a unit lattice cube can be deleted completely.

Ma (1995) further proposed a 3-D fully parallel thinning algorithm for generating medial faces. We first review this algorithm. Then this algorithm will be combined with theorem 4.1 to get the unit width skeleton of 3-D object, which also preserves connectivity.

The orientations of x -, y - and z -axis are shown in Figure 4.8. Suppose p is a point in a 3-D image. Let $e(p)$, $w(p)$, $n(p)$, $s(p)$, $u(p)$ and $d(p)$ be the east, west, north, south, up, and down neighbors of p , respectively.

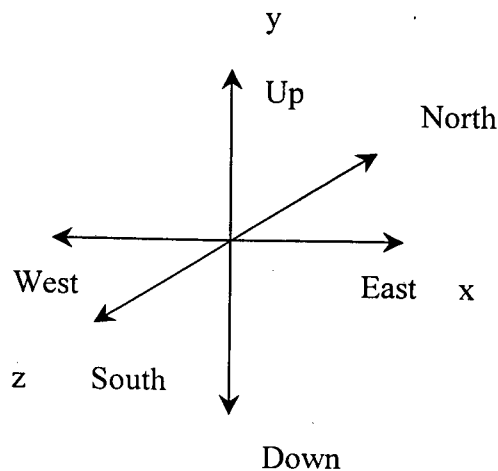


Figure 4.8 - The x -, y - and z -axis, and the arrangement of each orientation.

Consider the figures shown in Figure 4.9. In (b), at least one point marked \square is a white point, in (c) at least one point in $\{a_1, b_1\}$ and at least one point in $\{a_2, b_2\}$ are white points, and in (a) – (c), every unmarked point is either a black point or a white point.

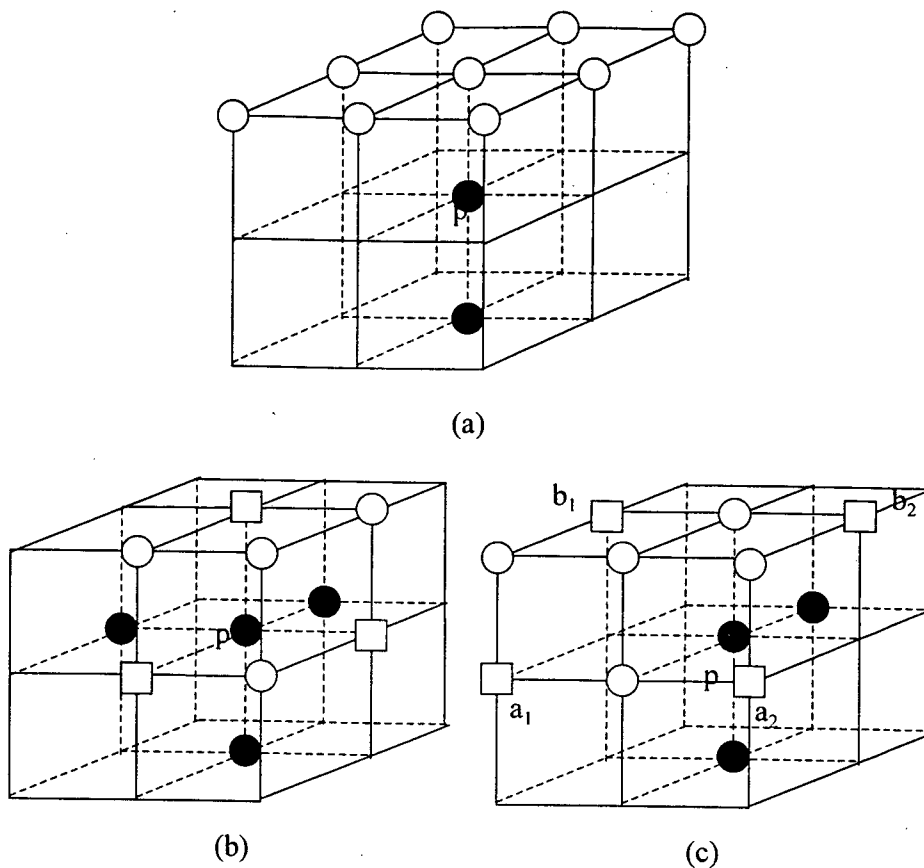


Figure 4.9 - Three deleting templates of the parallel thinning algorithm.
 • denotes a black point, o denotes a white point and □ denotes either a black point or a white one (see the text).
 Each unmarked point is either a black or a white point.

Let Ω be the set of all rotations and reflections (see appendix B) of all three configurations shown in Figure 4.9. For each element T of Ω , a black point p is said to satisfy T if all of the following conditions are satisfied:

- 1) p is a non-edged point;
- 2) if p is a north border point, then $s(s(p))=1$;
- 3) if p is an east border point, then $w(w(p))=1$;
- 4) if p is an up border point, then $d(d(p))=1$.

A black point p is said to satisfy Ω if p satisfies any element in Ω .

To establish the algorithm, we need the following preserving condition.

Rule 4.1 Suppose all four corners of a unit lattice square are to be deleted. Then the corner with the smallest sum of coordinates is preserved if and only if it is non-simple after the other three corners are deleted.

We now introduce the algorithm, which was proved by Ma (1995) that it preserves connectivity.

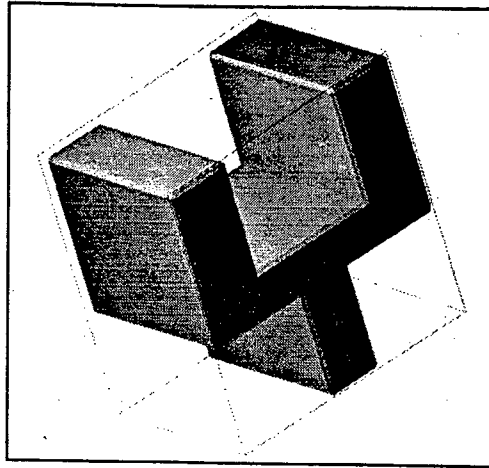
Algorithm 4.1 Ma's thinning algorithm

```
Repeat
    parallel delete every
    black point that satisfies
     $\Omega$  and is not preserved by
    above rule 4.1;
until
    no points are deleted.
```

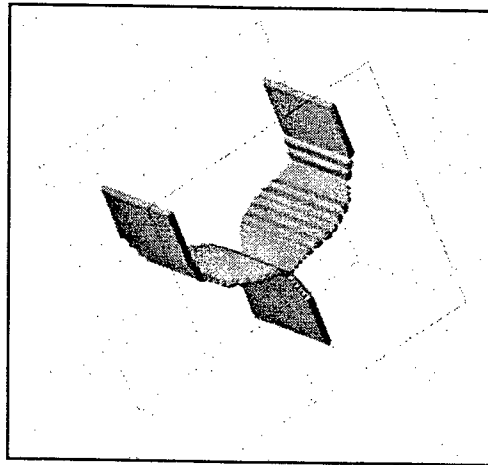
The above algorithm terminates when no black points can be deleted. Since we assume all input images contain finitely many black points, this algorithm will eventually terminate. This algorithm is the first connectivity preserving fully parallel thinning algorithm that needs only one application in each iteration (Ma, 1995). There are two phases in each application - one for marking black points satisfying Ω , and the other for releasing marked points that are preserved by the rule. The above algorithm obtains the medial faces. In order to generate the unit-width graph of skeleton, we further use theorem 4.1, which also preserves the connectivity.

4.3.3. Examples

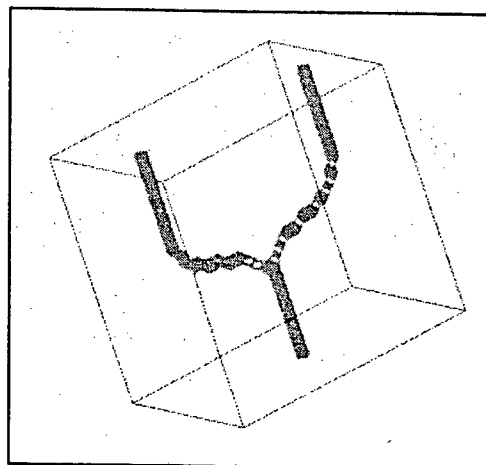
The further details on the verification of preserving connectivity were given in the literatures (Ma, 1994; 1995). Here we only show two examples of skeleton extraction. A simple example is shown in Figure 4.10 (a) original object (b) medial face of the object (c) final skeleton of the object. Figure 4.11 represents another example and its unit-width skeleton.



(a)

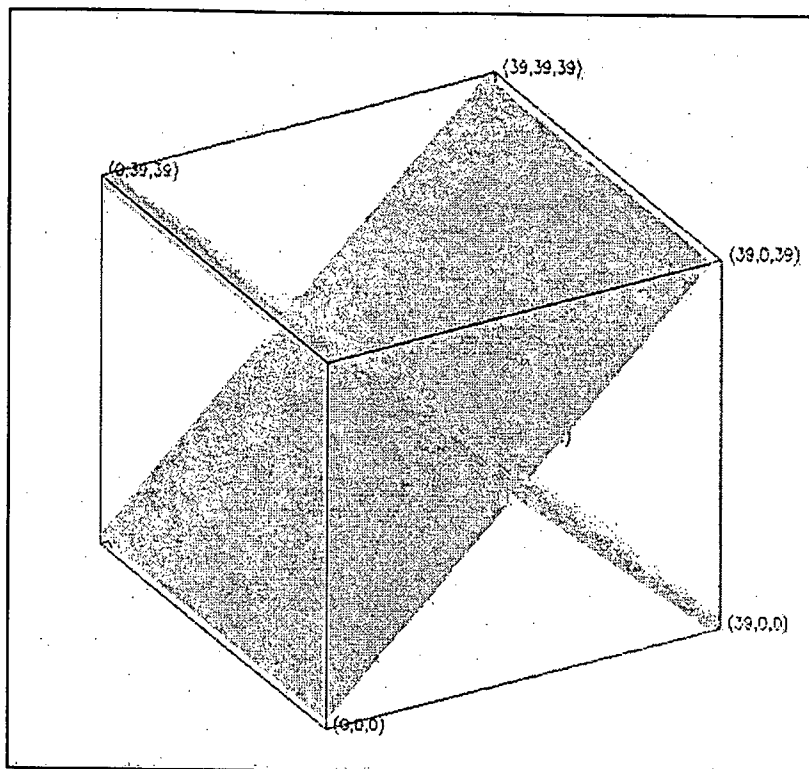


(b)

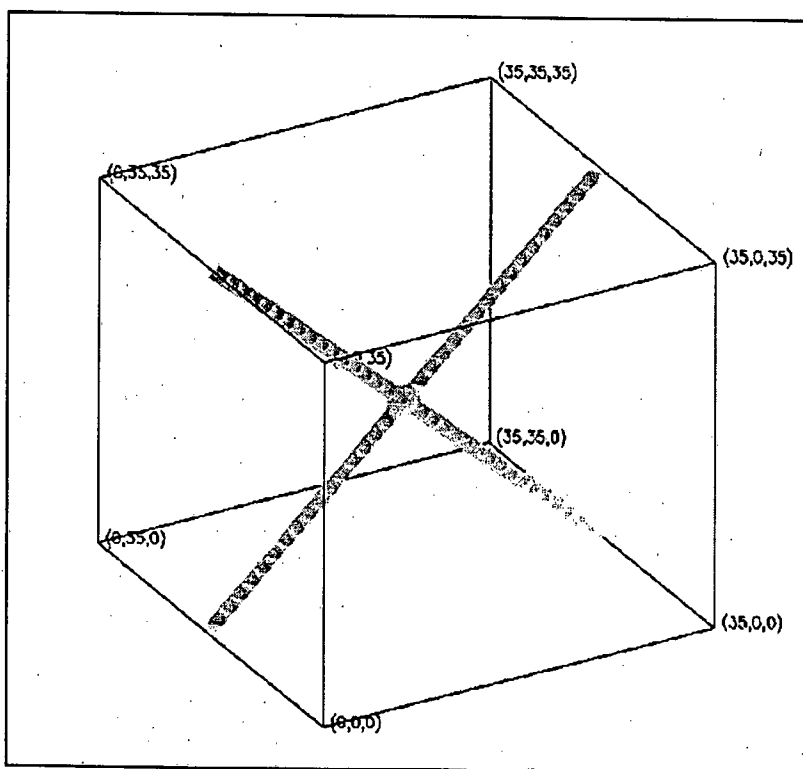


(c)

Figure 4.10 - Thinning of a simple object. (a) original object (b) medial face of the object (c) final skeleton of the object.



(a)



(b)

Figure 4.11 - Another example (a) original plane and (b) its unit width skeleton.

4.4. GRAPH OF 3-D POROUS STRUCTURE (SKELETON)

Serra (1982) and Adler (1992) defined the skeleton of the pore space as the set of points (voxels) at equal distance from two or more points of the solid wall. The skeleton may thus be thought of as a spatial representation of the center line of pore space. This spatial center line will contain points where two or more lines meet. These meeting points are the network nodes (approximate center of pore bodies) which are connected to other nodes by links or pore throats.

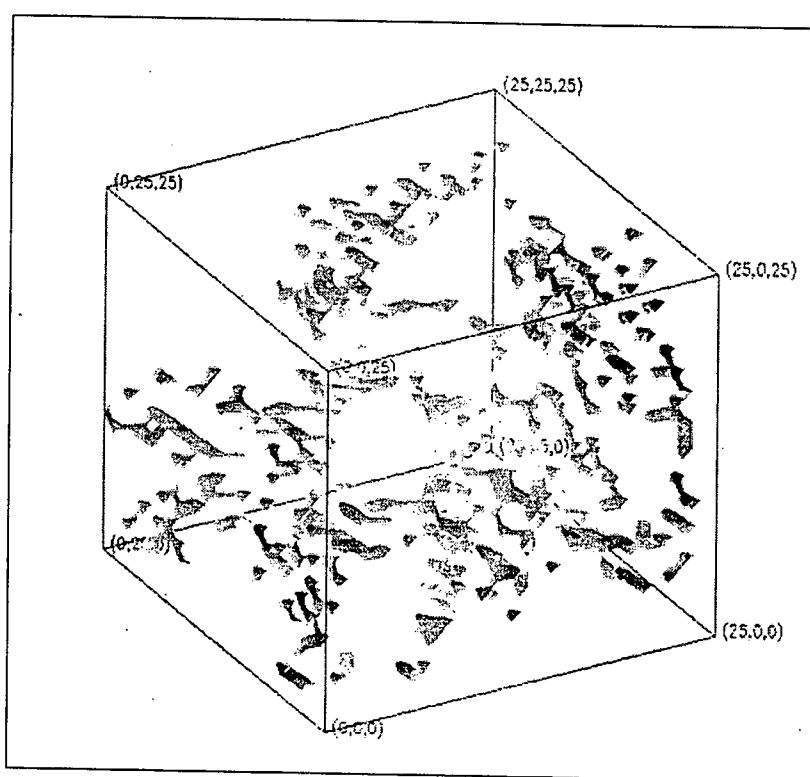


Figure 4.12 - Skeleton of the reconstructed porous structure in Figure 4.1 for sample GF2.

The skeleton of a 3-D pore space provides a way of visualizing the graph of the porous structure. It gives both visual and quantitative information about the connectivity of the pore space and about the coordination number for every pore body. The skeleton is also a very good basis for a complete quantitative analysis of the geometry of the pore bodies and throats. Thovert *et al.* (1993) succeeded in developing a 3-D thinning algorithm that worked well on their models. However, as discussed by Bakke and Øren (1996), visual examination showed

that in some complex voxel junctions, the algorithm introduced artificial holes in the skeleton of pore space. This can lead to wrong results for fluid flow purposes because they may change coordination numbers for pore bodies. In the present work, 3-D thinning algorithm described in section 4.3 is used to extract the skeleton of the pore space, which preserves connectivity. Figure 4.12 shows the skeleton of the 3-D reconstructed porous structure for sample GF2. Once the skeleton is extracted, the nodes and links in the skeleton are classified and defined by their spatial coordinates. The degree of each node (coordination number) is also calculated and recorded.

4.5. "PORE SIZE" DISTRIBUTION AND HYDRAULIC RADIUS

If the radius r of the cylindrical capillaries or spherical pore bodies in porous media is randomly distributed, then the pore size distribution function can be defined as $F(r)$. It is the probability of finding a given porous volume as cavities (cylinders or spheres) with radius smaller than or equal to the radius r . For general porous microstructures, however, it is difficult to define "pores" or "pore bodies", and the concept of pore size distribution remains ill defined. Nevertheless, a variety of well-defined probability distributions for arbitrary media have been introduced to overcome the above mentioned difficulty. Dullien (1992) discussed various definitions of effective sizes in detail. The concept of pore size distributions continues to be popular in most fields dealing with porous materials because of adsorption measurements and mercury porosimetry. The mathematical morphological approach can be used to determine pore size distribution. Opening operators with structural elements of increasing size are performed on the porous structure. The volume fractions for different sizes of structural element are obtained. Magnani (1996) developed an efficient algorithm for opening operation using a spherical structural element with d_{345} chamfer metric in 3-D.

The hydraulic radius is a useful measure of "size" in the case of irregularly shaped cross sections, as discussed by Dullien (1992). The hydraulic radius r_H for a capillary of uniform cross section is defined:

$$r_H = \frac{\text{volume of capillary}}{\text{surface area of capillary}} \quad (4.2)$$

For the case of a variable cross section the above definition can be generalized for any normal cross section of the capillary as follows:

$$r_H = \frac{\text{area of cross section}}{\text{length of perimeter of cross section}} \quad (4.3)$$

For the general case of irregular capillaries, the above ratio given must be calculated in all orientations of the sectioning plane for a fixed point inside the capillary. The minimum value of this ratio is the hydraulic radius r_H of irregular capillary at this point.

Dullien (1992) showed that the values of reciprocal hydraulic radius ($1/r_H$) and twice the reciprocal mean radius of curvature ($2/r_m$) in a capillary are almost identical. Here $2/r_m$ is related to the capillary pressure P_c , i.e., the pressure difference across the fluid-fluid interface with a mean radius of curvature r_m in mechanical equilibrium. Laplace's equation gives

$$P_c = \frac{2\sigma}{r_m}, \quad (4.4)$$

where σ is the interfacial tension. For the case of nonzero contact angle θ , r_m must be replaced by R , according to the relation

$$R = r_m \cos \theta. \quad (4.5)$$

Because hydraulic radius r_H is suited to the case of pore throats that control the flow rate of fluids through the porous medium, it will be used to predict permeability. Figure 4.13 and Figure 4.14 show a simple irregular 3-D shape and normal planes at two points, respectively. The normal plane at a link point in the skeleton is the cross section normal to the tangent line of the link. A simple example is shown in Figure 4.15. The area and perimeter of the cross section connected to the point in the normal plane can be calculated to obtain r_H (see appendix B).

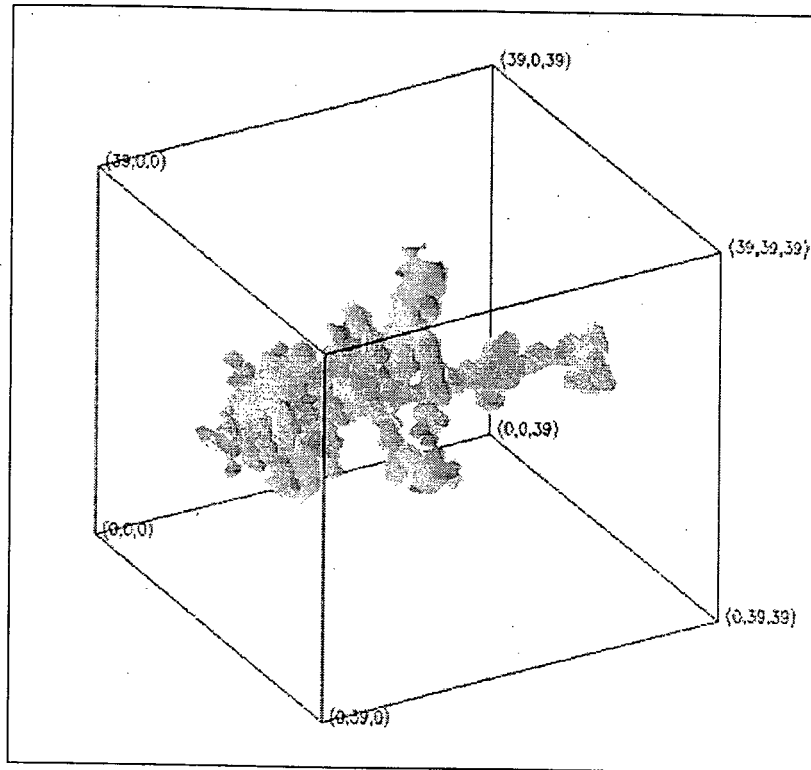


Figure 4.13 - A 3-D irregular shape.

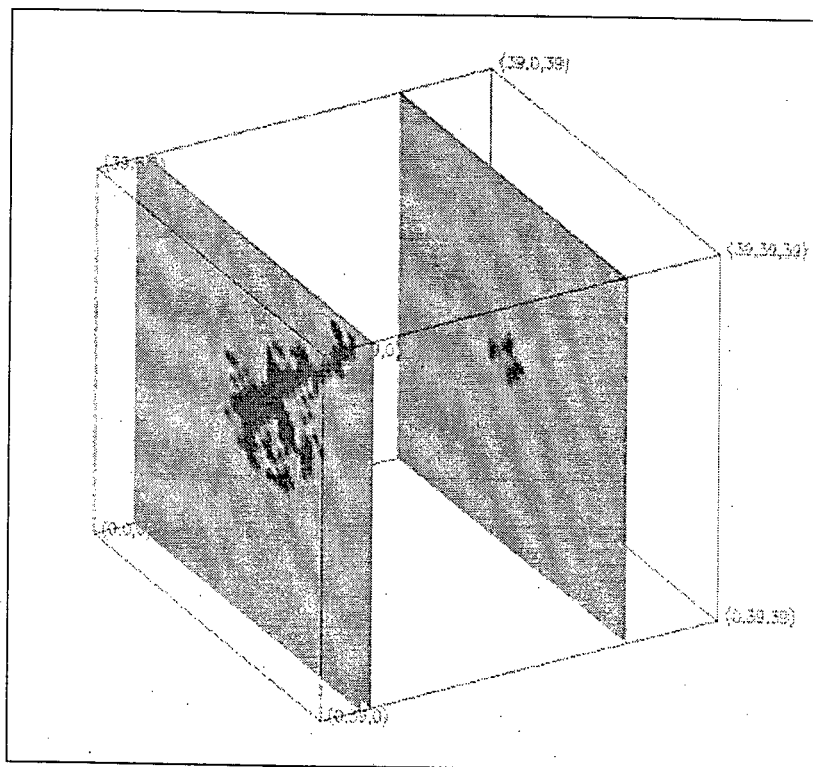


Figure 4.14 - Normal planes at two points of Figure 4.13.

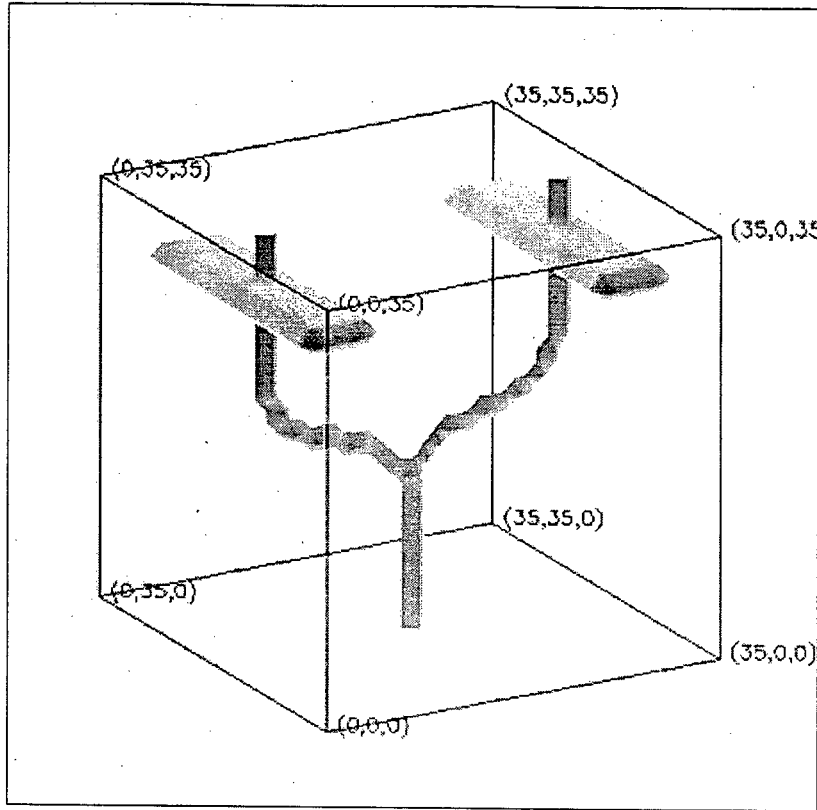


Figure 4.15 - Skeleton and its normal plane of Figure 4.10(a).

5. SIMULATION OF PERMEABILITY IN 3-D POROUS MEDIA

5.1. INTRODUCTION

The prediction of equilibrium and transport properties of porous media is a long-standing problem of great theoretical and practical interest, particularly in petroleum reservoir engineering (Dullien, 1992). Macroscopic properties, such as the capillary pressure curves, the absolute and relative permeability, and the formation resistivity factor, are closely related to the fluid distribution and multiphase flow in reservoir rocks. Their accurate determination is vital to the exploration of oil and gas reserves, in the design and application of production schemes, and is, at present, the subject of laborious experimentation. Sometimes routine permeability measurement is not applicable to the sample such as damaged core material. Therefore, it is essential to predict permeability accurately.

The permeability is the most important physical property of a porous medium in much the same way as the porosity is its most important geometrical property. The main numerical means for estimating the permeability of a disordered pore space has been computer simulation using a network model. A pore throat shape (e.g., cylindrical, channel-like, etc.) and a flow regime (e.g., laminar) are assumed. The flow problem is then solved analytically for a single pore, from which an expression is obtained for the flow rate q_i in pore i in terms of the pressure drop along the pore and the length and effective radius of the pore. In most cases the pressure drop across a pore body, where the pore throats meet, is ignored. One then writes down a mass balance for each node, or each pore body, which obeys that the net flow rate reaching it is zero. Such a mass balance for every interior node of the network results in a set of simultaneous equations for nodal pressures. From the solution of this set of equations the pressure field in the network is calculated. Further, the flow rate and finally permeability through the network can be derived from the pressure field. The boundary conditions are usually an imposed flow rate or an imposed pressure gradient in one direction and periodic or impervious boundary conditions in the other directions. One usually distributes the effective

sizes of the pore throats according to a probability density function which represents the pore size distribution. Various versions of this network simulation have been used in the previous literatures (e.g., Koplik, 1982; Koplik *et al.*, 1984; Ioannidis and Chatzis, 1993).

5.2. REVIEW ON SIMULATION OF PERMEABILITY

Permeability measures quantitatively the ability of a porous medium to conduct fluid flow. The permeability K is defined by Darcy's law:

$$Q = \frac{KA}{\mu} \frac{\Delta P}{L}, \quad (5.1)$$

where Q is the volumetric flow rate, A is the normal cross-sectional area of the sample, L is the length of the sample in the macroscopic flow direction, $\Delta P \equiv P_1 - P_2$ is hydrostatic pressure drop, and μ is the viscosity of the fluid. Darcy's law is limited to viscous or creeping flow, Newtonian fluids, absence of physical or chemical changes due to the fluid, no slip, and isotropic media. The permeability has dimension of an area, and it is usually measured in units of Darcy. A porous material has permeability equal to 1 Darcy if a pressure drop of 1 atm produces a flow rate of $1 \text{ cm}^3/\text{s}$ of a fluid with 1 cp viscosity through a cube having side 1 cm in length. 1 Darcy is equal to $0.987 \times 10^{-12} \text{ m}^2$ in SI unit.

Q and P in Eq. (5.1) are macroscopic averages, measured over several pore lengths or more. If this average is taken over a length larger than any correlation length in the porous structure of the medium, then the permeability K is a well-defined, intensive property of the rock, which characterizes its flow resistance. Measurement of permeability in the case of isotropic media is usually performed on cylindrical "core" samples at a single steady flow. In addition to the steady-state methods, unsteady-state permeametry is also used to measure permeability.

Dullien (1992) divided permeability models into the following types: deterministic, capillary, statistical, empirical and network models. The simplest approaches based on the idea of conduit flow do not pay any attention to the fact that different pores are interconnected with each other. These are called capillary permeability models, among which the so-called Carman-Kozeny model enjoys much greatest popularity. In the Carman-Kozeny theory, the porous medium was assumed to be equivalent to a conduit, in which the pore space is represented as an array of cylindrical tubes. The crucial assumption of the model is that the tubes do not intersect each other. Often it is also assumed that the tubes are straight or parallel

to each other. If a probability law is used, the model is called a statistical permeability model. One such statistical permeability model is called cut-and-random-rejoin-type model. It is assumed that the fraction of the area of a given section occupied by pore openings can be deduced from the drainage capillary pressure curve. The sample is sectioned into two parts by a plane perpendicular to the direction of flow, and two parts are joined together again in a random fashion. The flow rate in the capillaries is assumed by a Hagen-Poiseuille type relationship. Due to the use of drainage capillary pressure curve, this model suffers from the shortcoming of assigning all the pore volume to entry pores. In empirical permeability models permeability is usually correlated with some characteristic parameters. Here only some related permeability models are reviewed.

5.2.1. Deterministic Permeability Model

The low Reynolds number flow of an incompressible Newtonian fluid is governed by the usual Stokes equations:

$$\nabla p = \mu \nabla^2 \mathbf{v}, \quad (5.2)$$

and

$$\nabla \cdot \mathbf{v} = 0, \quad (5.3)$$

where \mathbf{v} , p and μ are the velocity, pressure and viscosity of the fluid, respectively. In general, \mathbf{v} satisfies the no slip condition on the fluid solid surface S :

$$\mathbf{v} = 0 \text{ on } S. \quad (5.4)$$

To determine the permeability of porous structures one can numerically solve the Stokes equation. A pressure difference is prescribed across the 3-D microstructure and Eq. (5.2) is solved using a finite difference scheme in conjunction with the artificial compressibility relaxation algorithm. The digital image based microstructure is discretized into a marker-and-cell mesh (MAC). A node was centered in each pixel, with pressure defined at the nodes, and velocities defined at the pixel boundaries. Figure 5.1 shows the schema for 2-D case (Martys and Garboczi, 1992). No-slip boundary conditions are imposed at all fluid-solid interfaces. This results in velocity profiles across channels being accurate to at least second order. Once the system has sufficiently relaxed, permeability of the porous medium is calculated by volume averaging the local fluid velocity and applying the Darcy equation.

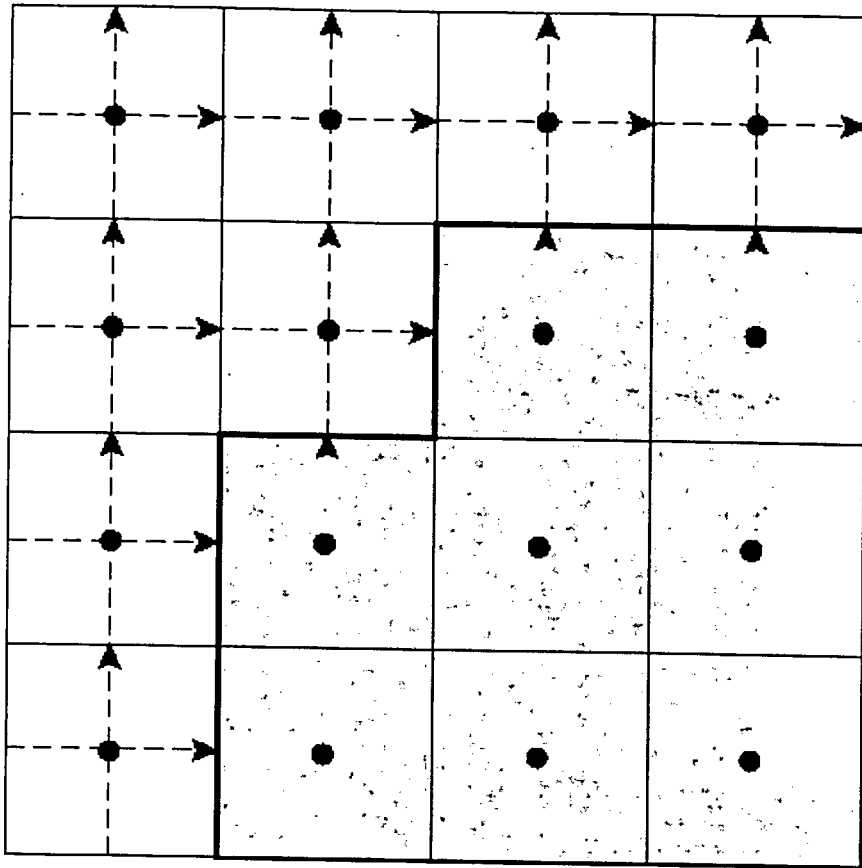


Figure 5.1 - A piece of a pore space-solid interface. The dark lines are pixel boundaries, and the dashed lines are the superimposed MAC mesh for the fluid-flow computation. The arrows show the location where the fluid velocities are determined, and the black circles show the nodes where the pressures are determined.

Adler *et al.* (1990) used the above method to determine numerically the Stokes flow of a Newtonian fluid in 3-D reconstructed porous media. The permeability of these media is derived from these flow fields. They reported that the permeabilities for Fontainebleau sandstones were underestimated by a factor of 5 in the worst case. In order to improve the accuracy of the solution, Bentz and Martys (1994) used non-centered difference equations near the pore surface to force the fluid velocities to be zero exactly at pixel boundaries. They also used an improved reconstructed porous media. The averaged permeability was within a factor of 2.7 of the values for the original microstructures.

5.2.2. Network Permeability Model

Koplik (1982) carried out a calculation on 2-D regular networks consisting of circular junctions (pores) centered at the intersections of straight channels (necks) and found linear relations of the Hagen-Poiseuille type between the flow rate and the pressure drop in both the pore and the neck. Hence the problem of calculating the network conductance could be reduced to the analogous electrical problem. He solved the problem by inverting the appropriate conductance matrix and averaging over the probability distribution function of the network elements. He found that averaging over the random medium could be carried out semi-analytically using an effective-medium theory. A typical network is shown in Figure 5.2. It consists of a regular lattice arrangement of sites or "pores", connected by bonds or "throats". Pores and throats are characterized by their radii, with an independent probability distribution function for each, and by the center-to-center distance. Furthermore, the lattice is characterized by its coordination number, the number of throats meeting at a pore. The coordination number is equal to 4 in Figure 5.2. In general, it can be a random variable. Regular networks such as square, hexagonal, Kagomé, trigonal, cubic and cross square were treated.

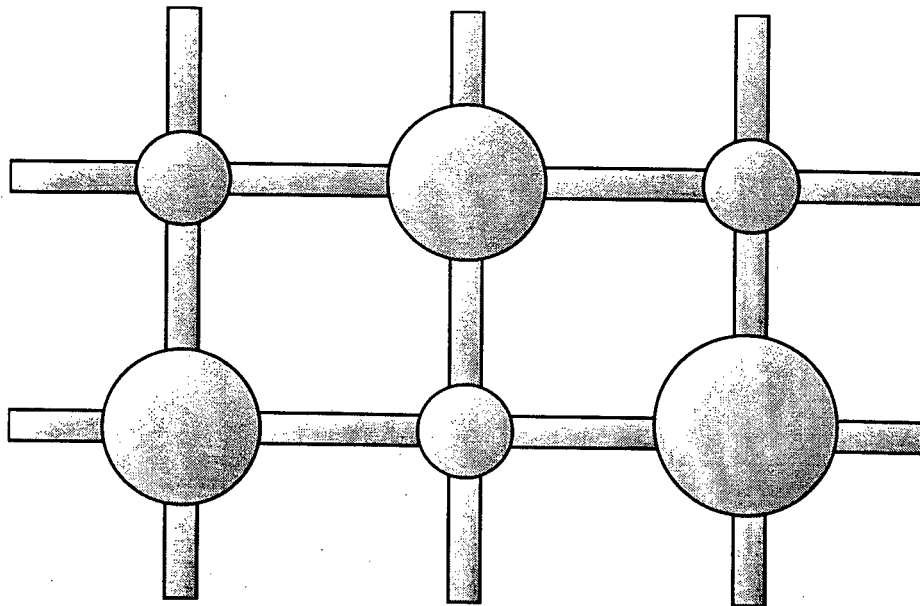


Figure 5.2 - Semi-regular network model of a 2-D porous medium (Koplik, 1982).

An application of this method to a real rock was given by Koplik *et al.* (1984). The theoretical analysis of permeability proceeds through the steps described in Figure 5.3. First, since the actual geometry of the porous material is often much too complicated for any quantitative study, they replaced it by a standardized model geometry. That is “ball and stick” networks of the type shown in the figure, with spherical pores connected by cylindrical throats. They made the simplifying approximation of neglecting the pressure drops through each pore body. The set of random throat sizes leads to a probability distribution of conductances, and they used effective-medium theory to average over this distribution. The idea of effective-medium theory is to focus on one conductor g and imagine that the random g 's in the rest of the network have averaged themselves out and can be described by a single effective medium value g_m . To fix the value of g_m , they consider the pressure field across the distinguished conductor; this differs from the field in the rest of the network by an amount depending on the particular value of g . This local fluctuation in the field over the probability distribution of g is averaged, and g_m is chosen in such a way that the average fluctuation is zero. Therefore, g_m is the solution of the following equation:

$$\int \frac{g - g_m}{g + (\frac{\bar{z}}{2} - 1)g_m} p(g) dg = 0, \quad (5.5)$$

where \bar{z} is the average coordination number of the network and $p(g)$ is the probability distribution function of g .

Then the “EM network” of Figure 5.3 is obtained, where each conductance has the value g_m . Further, the permeability is calculated as follows. Consider in Figure 5.4 a network of conductors in space, and fix the pressures at the two ends so as to produce an average pressure gradients $\overline{\nabla p}$. The total fluid flux crossing any plane S perpendicular to $\overline{\nabla p}$ is the sum of the individual fluxes in bonds intersecting S . Thus

$$Q = \sum_{i \in S} \frac{g_m}{\mu} \overline{\nabla p} \cdot L_i, \quad (5.6)$$

where L_i is the length of bond i . Dividing by the area of the plane A and comparing with Darcy's law Eq. (5.1) we can get the permeability

$$K = g_m \frac{\sum_{i \in S} L_i}{A}. \quad (5.7)$$

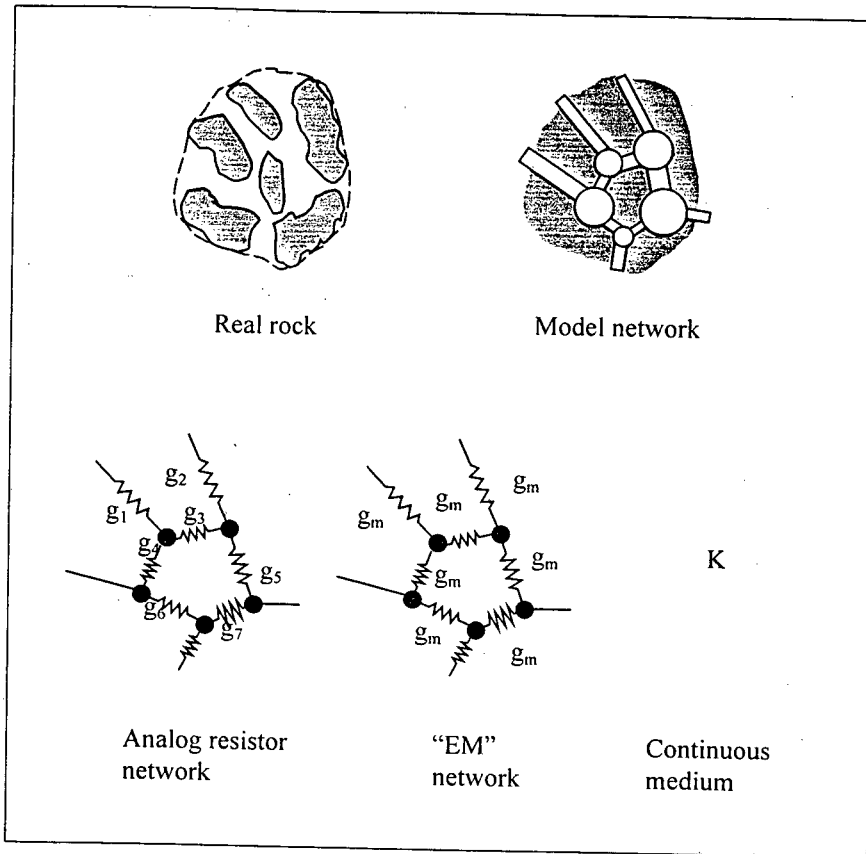


Figure 5.3 - Schematic sequence of operations in analyzing permeability.

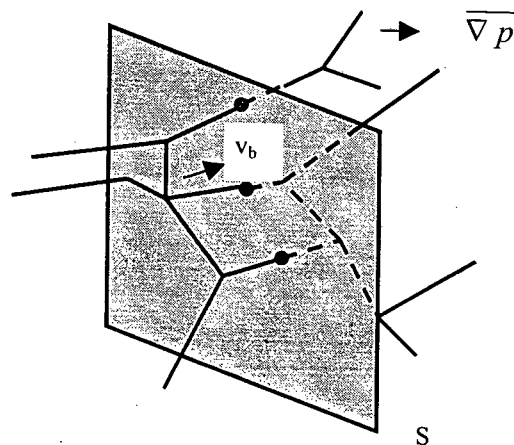


Figure 5.4 - Construction for calculating the permeability of a random network.

They analyzed in detail a Massillon sandstone, used serial sections of the pore space to determine an equivalent random network of cylinders. The fluid flow permeability of this network was estimated by Eq. (5.7). They found that the predicted permeabilities differ from the data by about one order of magnitude. They attributed the difference to the fact that most sedimentary rocks are highly heterogeneous and anisotropic.

5.2.3. Empirical permeability model

Dullien (1992) introduced two empirical permeability models using correlations with breakthrough pressure and porosity. The physical basis of this model is that the permeability of a tube with step changes in diameter, of given length L and volume, can be matched by the permeability of a bundle of n uniform tubes of diameter D_x , the same length L and same total volume if the following relationship between geometrical dimensions of the tubes exists (see Figure 5.5):

$$D_x = D_s \frac{(1 + L_1/L_s)^2}{[1 + (D_1/D_s)^2(L_1/L_s)][1 + (D_s/D_1)^4(L_1/L_s)]} \quad (5.8)$$

It is interesting that D_x is always smaller than D_s . For bundle of uniform capillary tubes, the permeability can be calculated analytically. Assuming a cube shaped sample of edge length L , the model consists of n parallel capillaries of length L and diameter D_x , satisfying the condition of porosity ε of the sample:

$$\varepsilon = \frac{n\pi D_x^2}{4L^2}, \quad (5.9)$$

and the condition of flow rate Q under the influence of the pressure drop ΔP :

$$Q = n \frac{\pi D_x^4 \Delta P}{128\mu L}, \quad (5.10)$$

given by the Hagen-Poiseuille equation, which is expressed also by Darcy's law

$$Q = K \frac{A \Delta P}{\mu L} = K \frac{L^2 \Delta P}{\mu L} = K \frac{L \Delta P}{\mu}. \quad (5.11)$$

Combination of Eq. (5.9) and (5.10) to (5.11) gives the permeability:

$$K = \varepsilon \frac{D_x^2}{32}. \quad (5.12)$$

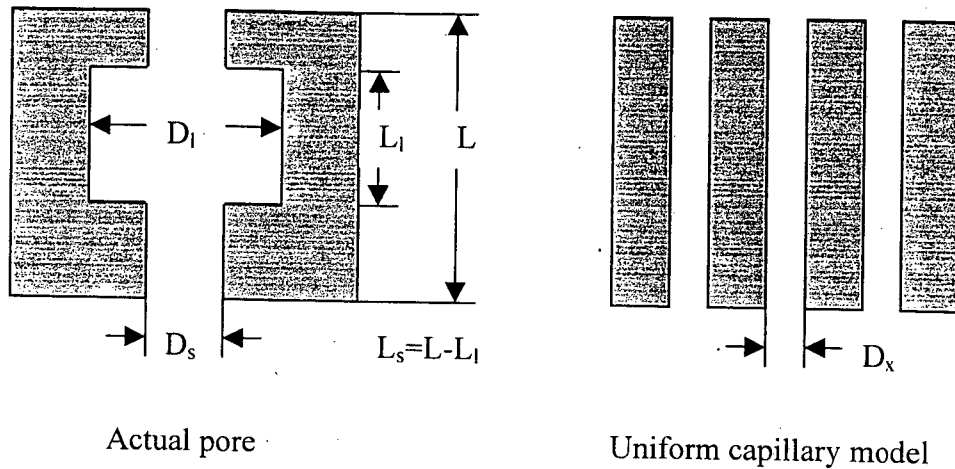


Figure 5.5 - Bundle of uniform capillary tubes model of identical diameter for the periodically constricted tube model (Dullien, 1992).

In the case of sandstone samples, Dullien (1992) found that $D_x = D_b/3.5$, where D_b is the “breakthrough” diameter. Hence, the calculated permeability could be expressed as follows:

$$K = \left(\frac{D_b}{3.5}\right)^2 \left(\frac{\varepsilon}{32}\right) \times 10^3 \text{ (mD)}, \quad (5.13)$$

where D_b is in μm unit. Another correlation of permeability with breakthrough capillary pressure was found by Chatzis (1980):

$$K = \left(\frac{85.63}{P_{cb}}\right)^{2.71}, \quad (5.14)$$

where P_{cb} is the breakthrough capillary pressure in psi unit, measured in the Hg/air system.

5.3. PREDICTION OF ABSOLUTE PERMEABILITY

The deterministic permeability model offers the ability to study the micro-physical basis of macroscopic transport. But it is time consuming. The network models have been used in the last four decades. However, they are all based on the some information of porous structure, such as size distribution and coordination numbers, which is almost assumed in the previous works.

The 3-D skeleton of a reconstructed porous structure results in a real network, which can be used to predict the permeability without making any assumptions concerning coordination number and the shape of porous cavities, as in the previous network models mentioned above. Further, as velocity field calculations by solving Navier-Stokes equation are avoided, 3-D skeleton based permeability models are less time consuming, need less computer storage capacity and enable the calculations to be performed for larger microstructural samples.

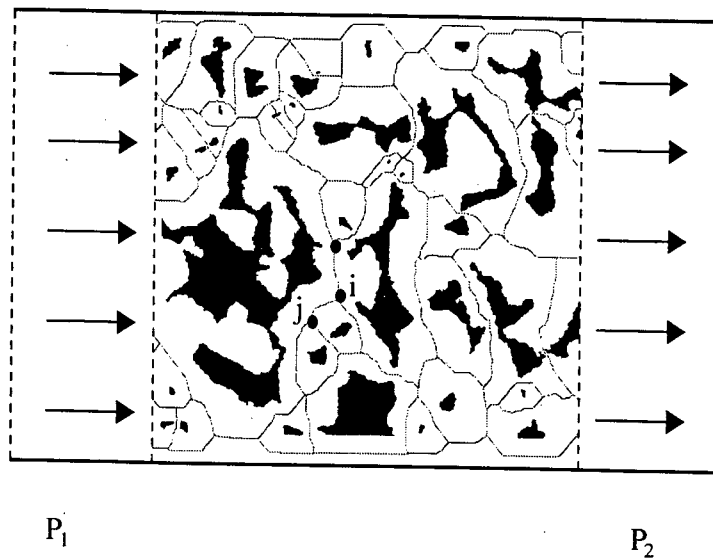


Figure 5.6 - The 2-D graph representation of pore space (skeleton).

The 3-D reconstructed porous media described in chapter 3 are used to calculate permeability. The x-axis of the network is chosen to be parallel to the direction of macroscopic flow. Impervious boundary conditions are applied to the sides of the network that are parallel to axes y and z. The graph of the porous structure is obtained by using a thinning algorithm, which preserves the connectivity, as described in chapter 4. To simplify illustration of the process to calculate permeability, a 2-D graph of the pore space is used, as shown in Figure 5.6. To calculate the resistance of each point of the graph and save computer memory, we use graph theory (Christofides, 1975) to describe the network. The links and nodes of the graph are composed of points with exactly two neighbors and three or more neighbors, respectively. A preferable way to describe a graph is by specifying the set of *nodes*

and a *correspondence* that shows how the nodes are related to each other. The degree of a node is the number of links that connect it; this is also called coordination number.

To compute absolute permeability, the hydraulic resistance or conductance for the fluid in the network must be defined. The flow is assumed to be sufficiently slow. Furthermore, we make the simplification that the resistance to flow of fluid in a pore link may be characterized in terms of an equivalent diameter d_H , which is four times the hydraulic radius r_H , as discussed in section 4.5.

$$d_H = 4r_H. \quad (5.15)$$

Calculations of the hydraulic radius r_H in a capillary are shown in appendix B. Thus, the conductance of fluid in a pore link, g_L , is given by Poiseuille's equation and may be written as:

$$g_L = \frac{\pi d_H^4}{128\mu l}, \quad (5.16)$$

where μ is the fluid viscosity and l is the length of the pore (here $l=1$ pixel). The conductance of the fluid in a pore node, g_i , is given by Koplik (1983):

$$g_i = \frac{r_i^3}{3\mu}, \quad (5.17)$$

where r_i is the radius of the link connected the node i . The overall resistance to fluid flow between two neighboring nodes i and j , g_{ij} , is the sum of the pore node resistances and the pore link resistance, i. e.,

$$\frac{1}{g_{ij}} = \frac{1}{g_i} + \sum \frac{1}{g_L} + \frac{1}{g_j}, \quad (5.18)$$

where g_L is the conductance of the pore link and g_i and g_j are the two pore node conductances.

The flow rate of fluid between the two pore nodes,

$$Q_{ij} = g_{ij}(P_i - P_j), \quad (5.19)$$

where P_i and P_j are the nodal pressures. Since the fluid is incompressible, mass conservation requires that

* This result was obtained by Dagan, Weinbaum and Pfeffer (1982). There is a typographical error printed in Koplik's paper (1983).

$$\sum_j Q_{ij} = 0, \quad (5.20)$$

where j runs over all pore links connected to pore node i . Eq. (5.20), together with the appropriate boundary conditions, form a complete solution to the steady flow of an incompressible fluid in the pore network. These equations are solved using successive over-relaxation:

$$P_i = \beta \frac{\sum_j g_{ij} P_j}{\sum_j g_{ij}} + (1 - \beta) P_i, \quad (5.21)$$

where β is a relaxation parameter. By imposing a pressure drop ΔP across the network and computing the resulting single phase flow rate Q , the absolute permeability K of the pore network is calculated from Darcy's law

$$K = \frac{\mu L Q}{A \Delta P} = \frac{\mu (N_x - 4) Q}{(N_y - 4)(N_z - 4) n \alpha \Delta P} \quad (5.22)$$

where μ , L and A are the same as in Eq. (5.1), n is amplification factor, α is the length per pixel, and N_x , N_y and N_z are the side sizes of reconstructed porous medium. After thinning operation, the sizes of the graph of 3-D pore space are $(N_x - 4) \times (N_y - 4) \times (N_z - 4)$. Therefore, L is equal to $(N_x - 4) n \alpha$ and A is $(N_y - 4)(N_z - 4)(n \alpha)^2$.

5.4. EXAMPLE

We use a sample Fontainebleau sandstone GF2 described in section 3.5. The reconstructed 3-D pore structure and its skeleton are obtained by the method represented in chapter 3 and chapter 4. Figure 5.7 shows a graph of 3-D porous structure, in which it is assumed that fluid flows from the left to the right and the other sides are impervious. The pressure at the left side is P_1 and at the right is P_2 . Here water is used as the fluid. Various realizations are carried out and permeabilities are calculated. Table 5.1 gives the results of the permeability for different parameters of reconstructed porous media. It can be seen that when the sizes of the reconstructed porous media are large enough, the value of permeability tends to be stable. This means that the porous media can be considered statistically homogeneous. The predicted permeability for sizes $100 \times 100 \times 100$ is about 1.9 Darcy. The permeability is also calculated when the flow is applied to the y - and z -direction. Table 5.2 gives the results of permeability in three directions. It is shown that the permeability is almost identical in all

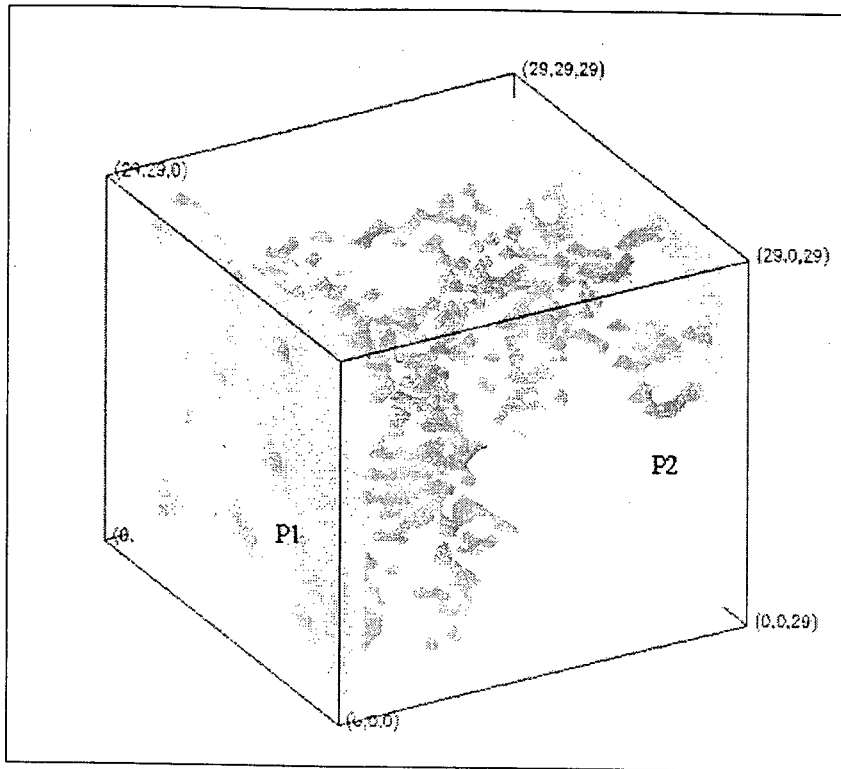


Figure 5.7 - A graph of 3-D Fontainebleau sandstone skeleton.

Table 5.1 : Results of predicted permeability ($\epsilon=0.25$, $\alpha=3.8 \mu\text{m}$, $n=4$, $\zeta=8$, $\beta=0.7$)

Size N	Number of nodes at left side	Number of nodes at right side	Total number of nodes	K (mD)
20	8	10	114	1,221.3
27	13	22	391	1,755.7
30	26	25	538	1,618.8
60	138	110	6,388	1,943.9
80	224	244	16,042	1,982.3
100	370	348	32,775	1,984.1

three directions. The comparison of the predicted permeability with experimental values and Adler *et al.*'s results is given in Table 5.3. It can be seen that the estimated permeability is a better approximate value than the one calculated by Adler *et al.* (1990) for this sample.

Table 5.2 : Comparison of predicted permeability in three directions (N=80, n=4, $\zeta=8$, $\alpha=3.8 \mu\text{m}$).

	x-direction	y-direction	z-direction
Number of nodes	16,042	16,010	16,120
K (mD)	1,982.3	2,043.1	1,979.3

Table 5.3 : Comparison of predicted permeability with experimental and Adler *et al.*'s results (n=4, $\zeta=8$, $\alpha=3.8 \mu\text{m}$).

	Size N	K (mD)
This work	27	1,755.7
	80	1,982.3
	100	1,984.1
Adler <i>et al.</i> (1990)	27	670.0
Experimental value		~2,700

6. RESULTS AND DISCUSSIONS

6.1. INTRODUCTION

As shown in Figure 1.1 and discussed in previous chapters, when one wants to predict the absolute permeability for a rock sample, the binary plane section image is firstly obtained by image analysis techniques. The porosity and autocorrelation function of the binary image are calculated by using Fourier transform. Then, a 3-D porous structure is generated by using the truncated Gaussian method with Fourier transform; this porous structure possesses the same porosity and autocorrelation function as the real sample in study. After the reconstructed porous structure is generated, a graph of 3-D pore space (skeleton) can be obtained by using a thinning algorithm, which preserves connectivity. Using the graph of pore space, the main flow path for a single flow can be obtained, and classified into nodes and links. The local cross-sectional area and perimeter normal to the flow path in each link is recorded to compute the local hydraulic radius. Resistance to flow may then be calculated for each link. A fluid pressure is computed at each node, and the total volumetric flux through the network is calculated. Then, the absolute permeability can be predicted from the corresponding network for the sample.

In this chapter, the whole process to predict the permeability is shown and the results for several samples are discussed. Section 6.2 shows the process for one example, including selection and analysis of the sample, generation of 3-D reconstructed porous structure, prediction of the permeability obtained from the graph of 3-D pore space and the effects of various reconstruction parameters on permeability. More results for several samples are given in section 6.3. Section 6.4 gives discussions about the results. These results are compared with experimental and empirical ones.

6.2. DESCRIPTION OF WHOLE PROCESS TO PREDICT PERMEABILITY

6.2.1. Sample Selection and Analysis

The sample investigated is a type of Berea sandstone. A 500 mD Berea sandstone shown in Figure 2.3 was selected as the sample. It is a digital binary image of a plane section of the sample, which is 609×458 pixels, with magnification of $50\times$. Each pixel corresponds to 2.6 microns. In Figure 2.3, pore and solid phase are represented in black and white, respectively (see section 2.2). The reported porosity by mercury intrusion is 22.5%. The average porosity in Figure 2.3 is 0.2214, which is in good agreement with experiment.

To roughly get an idea about the homogeneity of the sample, the image in Figure 2.3 was divided into two half parts, as shown in Figure 6.1. The porosity of two half images is 0.2229 and 0.2201, respectively. The normalized autocovariance function was measured on each part as shown in Figure 6.2. The sample is considered approximately homogeneous since the porosity and normalized autocovariance function of two half parts are almost identical with the ones of Figure 2.3.

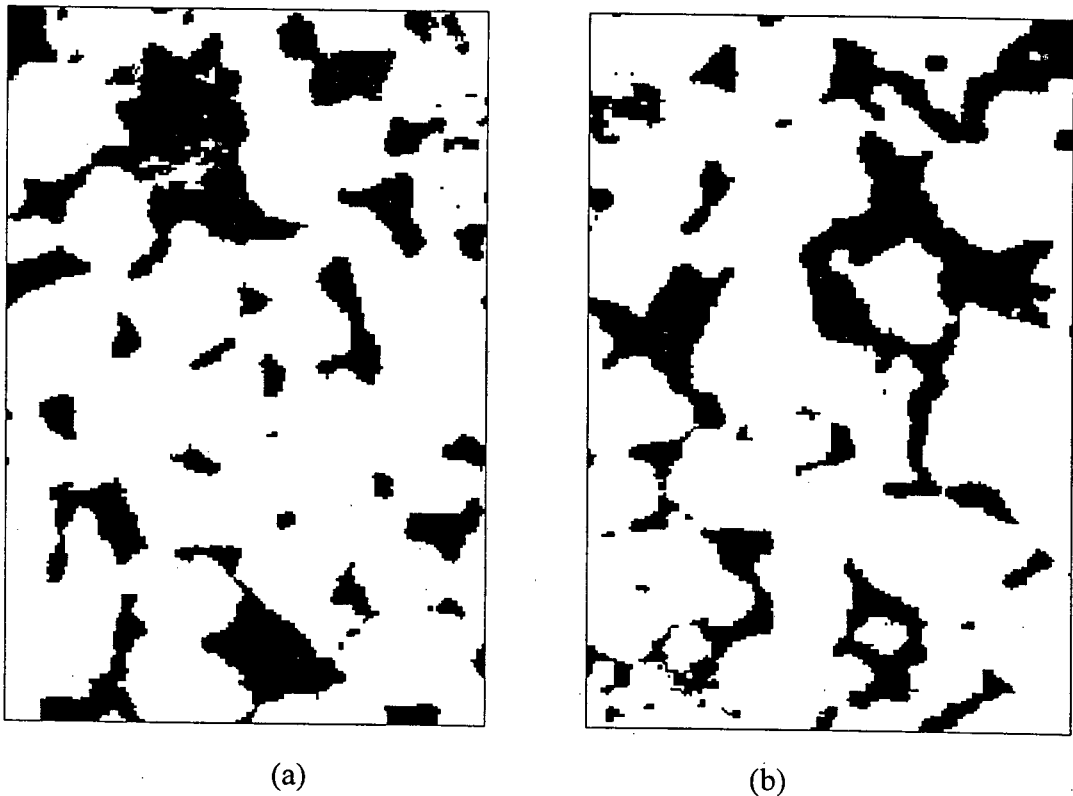


Figure 6.1 - Two half segments of Figure 2.3.

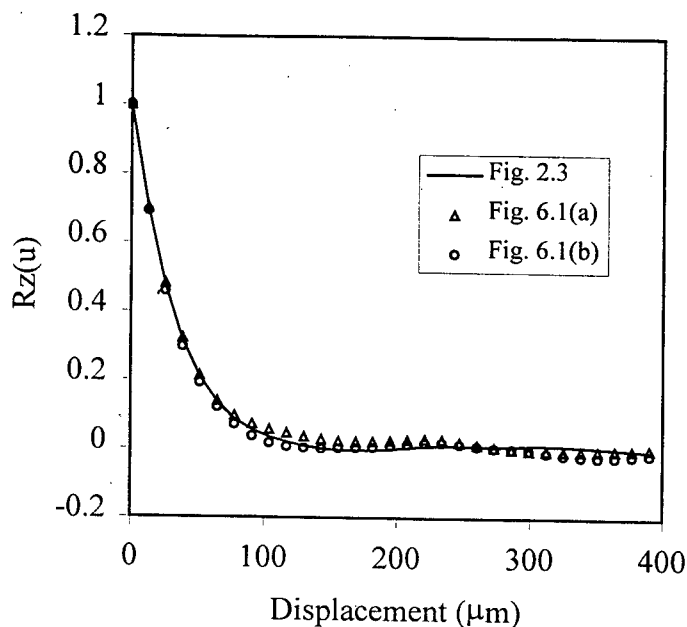


Figure 6.2 - Comparison of normalized autocovariance function for Berea 320220.

The concepts *stationary*, *homogeneous*, *heterogeneous* and *ergodic* can be further discussed here. Stationarity is a basic concept of stochastic process. A stochastic process is *stationary* if its statistics are not affected by a shift in the origin. A random field is called *homogeneous* if its mean is independent of position, i.e., constant and if its autocorrelation function is translational invariant. Otherwise, it is *heterogeneous*. Therefore, a random or periodic field is stationary. A stationary field must be homogeneous. However, the converse is not true. The concept ergodic for homogenous random field can be understood as follows: for example, porosity is a mean of binary image with area S . If S tends to infinite, the porosity is equal to constant. Then the random field is called *ergodic* with respect to the porosity. Anguy *et al.* (1995) used Fourier transform to check local homogeneity of the sample. In fact, local homogeneity is attained where the local microstructure may be either random or quasi-periodic. The falloff along the frequency away from $(0,0)$ in the power spectrum is only a measure of the coarseness (fractal or texture) of an image.

To test the isotropic property, autocorrelation functions were measured along the x and y directions. They are $C(x,0)$ and $C(0,y)$, which are compared with $C(u)$ in Figure 6.3. It is seen that the difference between autocorrelation functions in the two directions was found

statistically insignificant, thus verifying that the medium was isotropic. As discussed in section 2.4, the autocorrelation function obtained by Fourier transform method is more precise than the average autocorrelation function obtained in only two directions. This function and porosity will be used as the input data of next process. Pore size distribution function for sample was calculated using mathematical morphology (Philippi and Fernandes, 1995), which is shown in Figure 6.4.

6.2.2. Reconstruction of 3-D Porous Structure for Berea Sandstone

The reconstruction process of 3-D porous structure has been discussed in section 3.4.2. Here only the results of reconstruction for the sample are given. Normalized autocovariance function $R_Z(u)$ and the corresponding translated $R_Y(u)$ for the Berea 320220 are shown in Figure 6.5. Various realizations were done for different parameters. In order to get good results, different reconstruction parameters n , ζ and N were tested. As discussed in chapter 3, one has to choose appropriate n and N . Table 6.1 and Figure 6.6 gives effects of n on porosity and normalized autocovariance function for constant nN . The effects of N are shown in Table 6.2 and Figure 6.7, respectively. Table 6.3 and Figure 6.8 give the effects of random generator. It is seen that n for small n and seed is not important for the results, but with increase of N the porosity and normalized autocovariance function are better.

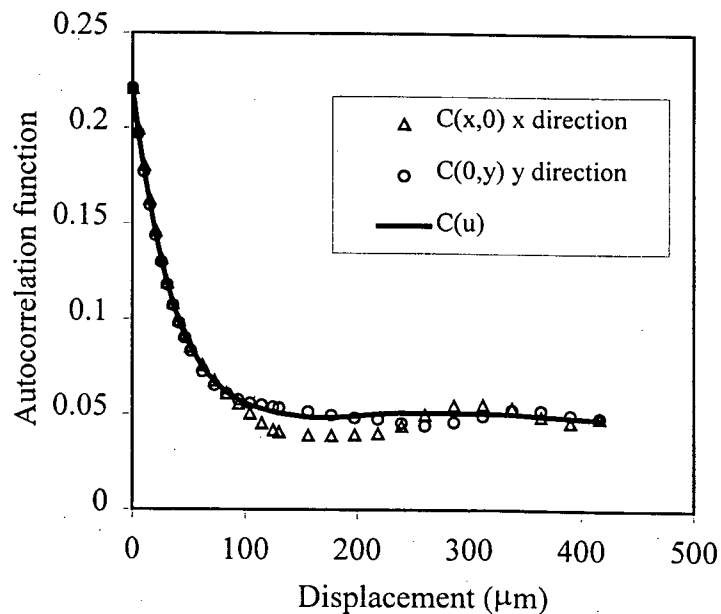


Figure 6.3 - Autocorrelation function of Berea 320220.

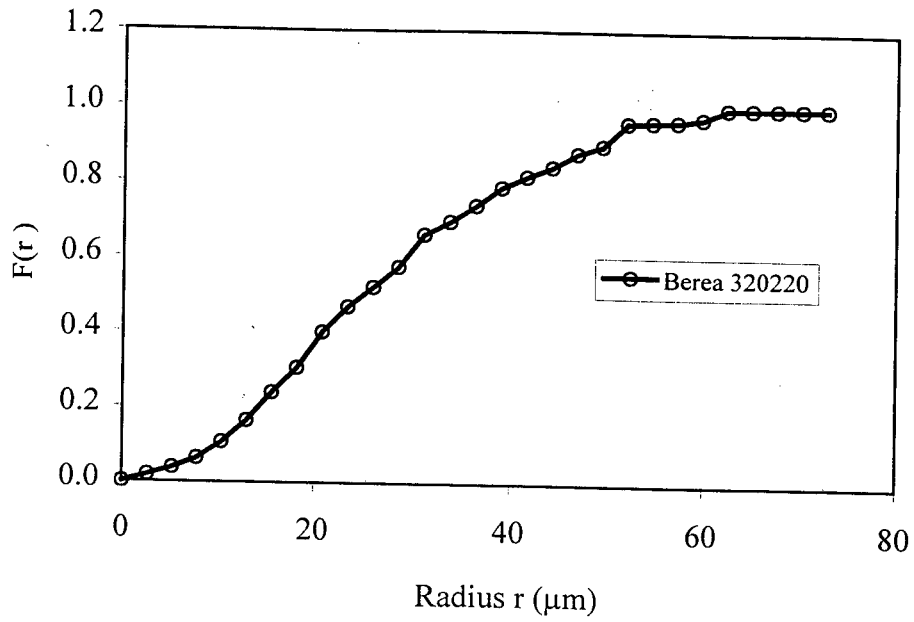


Figure 6.4 - Pore size distribution function for sample Berea 320220.

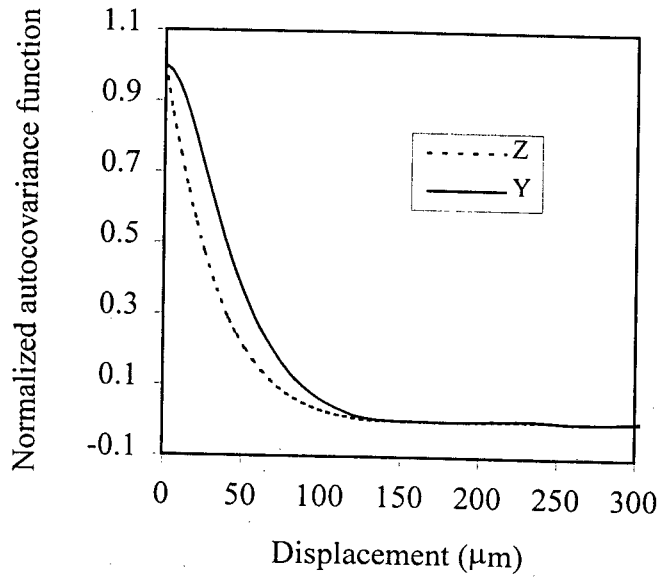


Figure 6.5 - Normalized autocovariance function $R_Z(u)$ and the corresponding $R_Y(u)$.

Table 6.1 : Effects of n on porosity ($\varepsilon = 0.2214$ and $nN = 240$).

n	N	Average of $Z(x)$ (porosity)	Running time (seconds)
2	120	0.2228	28
4	60	0.2212	12
6	40	0.2197	12
8	30	0.2197	4
10	24	0.2218	3

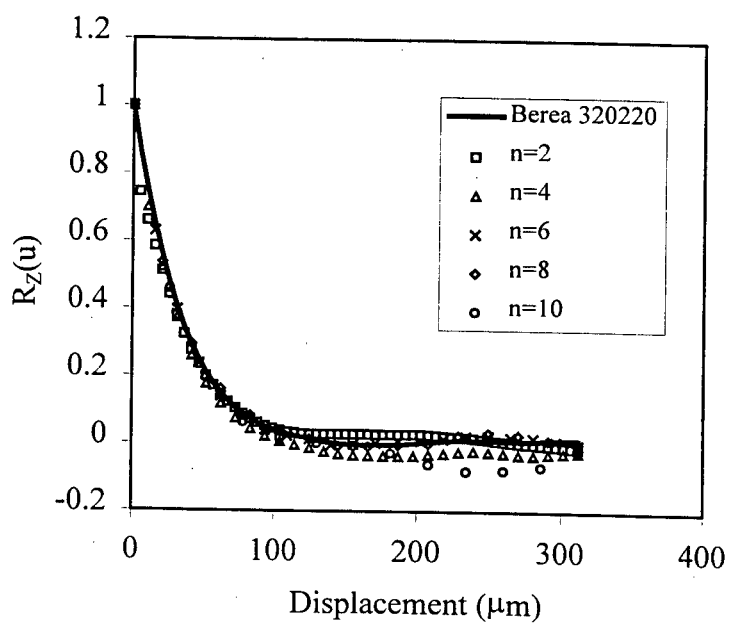
Figure 6.6 - Normalized autocovariance function of Berea 320220 for different n .

Table 6.2 : Effects of N on porosity ($\epsilon=0.2214$, $n=5$ and $\zeta=12$).

N	Average of Z(x) (porosity)	Running time (seconds)
24	0.2301	2
40	0.2272	13
60	0.2211	21
80	0.2221	49
100	0.2208	105
120	0.2213	242

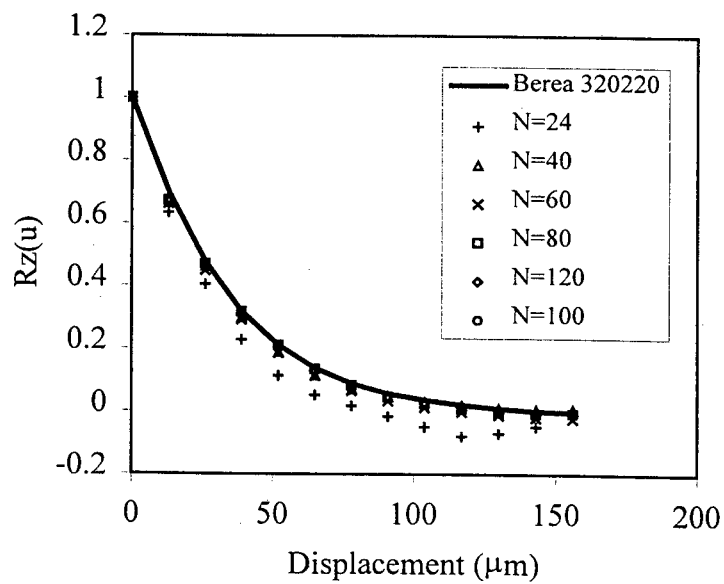


Figure 6.7 - Normalized autocovariance function of Berea 320220 for different N.

Table 6.3 : Effects of random generator on porosity ($\epsilon=0.2214$, $n=3$, $\zeta=20$ and $N=100$).

Seed	Average of $Z(x)$ (porosity)	Running time (seconds)
-100	0.2208	105
-200	0.2207	110
-300	0.2211	110
-400	0.2218	103
-500	0.2220	111
Average	0.2212	107.8

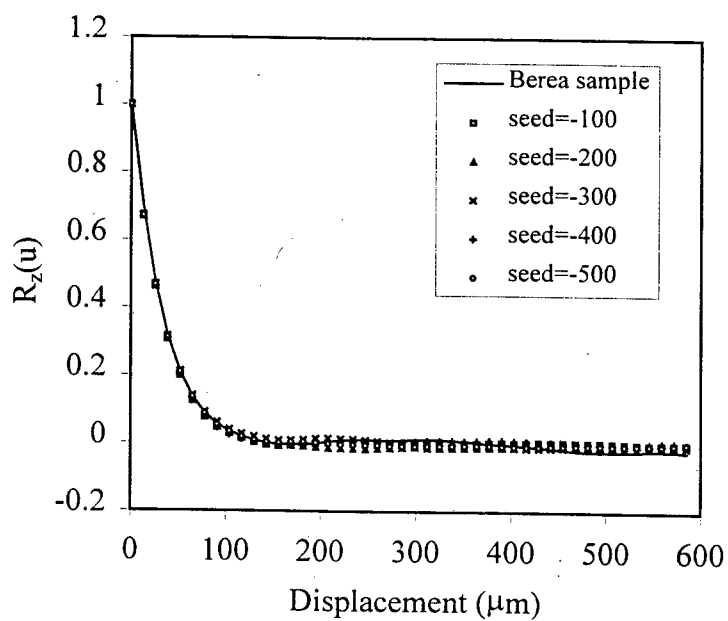


Figure 6.8 - Normalized autocovariance function of Berea 320220 for different realizations.

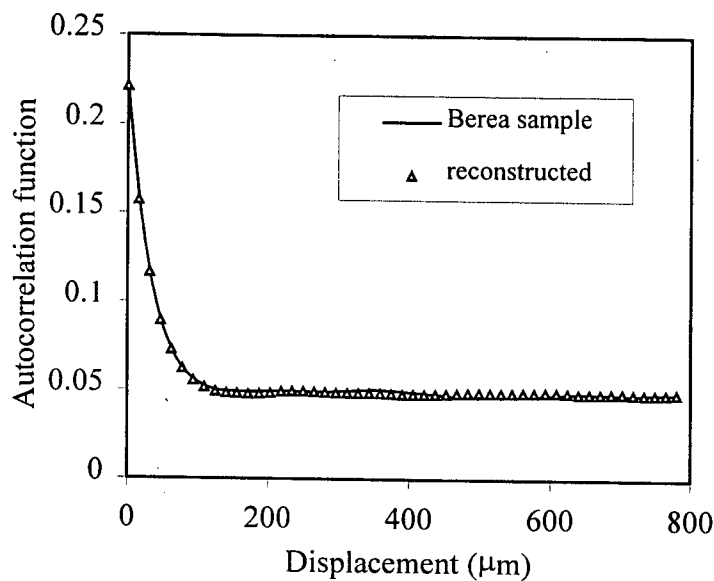


Figure 6.9 - Comparison of autocorrelation function between the sample and the reconstructed porous structure (Berea 320220, size 80^3).

Using $n=6$, $\zeta=18$ and $N=80$, a reconstructed porous structure was generated. The total porosity of the structure was found 0.2228. The average autocorrelation function of the reconstructed Berea sample compares favorably to the original autocorrelation function, as it is shown in Figure 6.9. The visualization of a 3-D reconstructed porous medium of this sample is shown in Figure 6.10. It should be noticed that stochastic realizations of porous structure may generate non-percolating solid and pore components. In this work, these components can be determined by an efficient cluster multiple labeling algorithm developed by Hoshen and Kopelman (1976) in 2-D case and extended by Magnani (1996) for 3-D case. In this example, the fractions of non-percolating solid and pore phases are 0.0008 and 0.012, respectively. The non-percolating solid phases correspond to islands isolated inside the pore phases. This is impossible in the real porous media. Then they were change as pore phases. This makes porosity of the reconstructed porous structure become 0.2236. Percolating and non-percolating porosity are 0.2224 and 0.012, respectively. Figure 6.11 shows the results of removing the isolated components. Comparison of normalized autocovariance function between reconstructed porous structure and the one after removal of isolated components is shown in Figure 6.12. A cutout and an oblique slice display of the reconstructed porous

structure in Figure 6.11 are shown in Figure 6.13 and Figure 6.14 respectively. Figure 6.15 shows the block display of the reconstructed porous medium in Figure 6.11.

Reconstruction preserves the pore size distribution measured in the original 2-D section as shown in Figure 6.16. In this figure, comparison is made between the original measured pore size distribution (see Figure 6.4) and the mean pore size distribution obtained from several sections of the reconstructed porous structure. The pore size distributions for all xy plane sections in z direction were calculated and averaged in this figure. Nevertheless, 3-D pore size distributions of reconstructed microstructure are only approximate when compared with 2-D pore size distribution of the sample (Figure 6.17).

A graph of reconstructed porous structure is obtained by a thinning algorithm described in the chapter 4 and shown in Figure 6.18. Figure 6.19 shows the slice display in three directions of Figure 6.18.

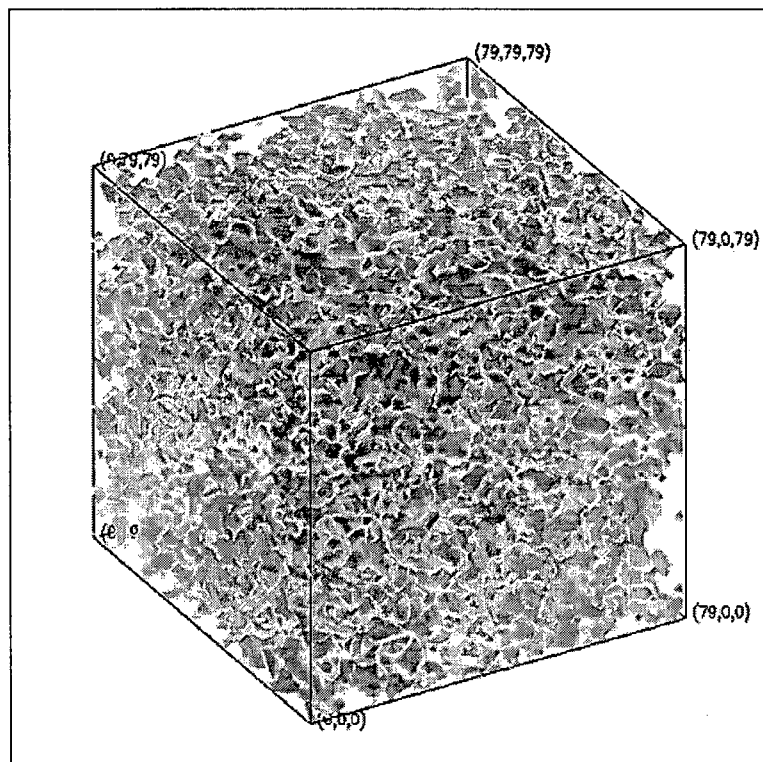


Figure 6.10 - A sample reconstruction of porous structure (Berea 320220, size 80^3).

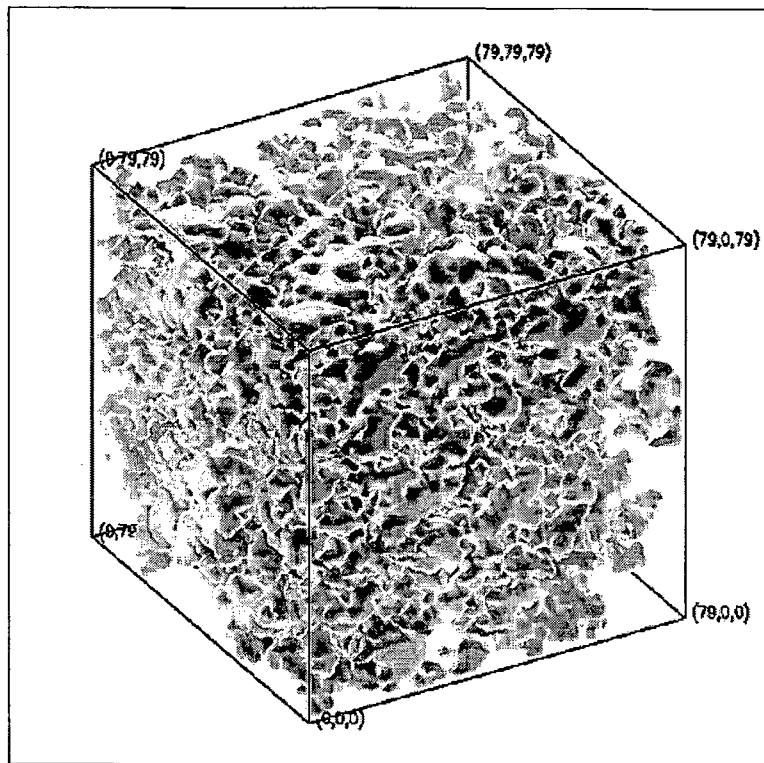


Figure 6.11 - Isosurface of 3-D porous structure after removal of isolated solids (Berea 320220, size 80^3).

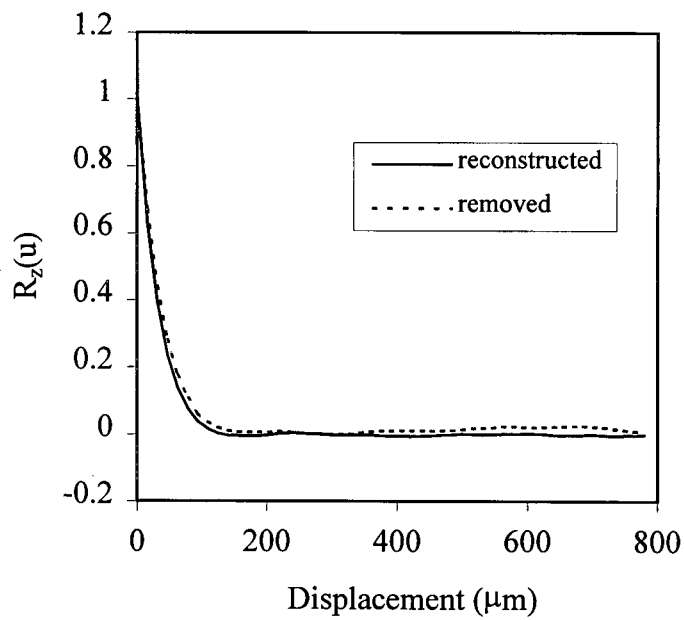


Figure 6.12 - Comparison of normalized autocovariance function between reconstructed and after removal of isolated components (Berea 320220, size 80^3).

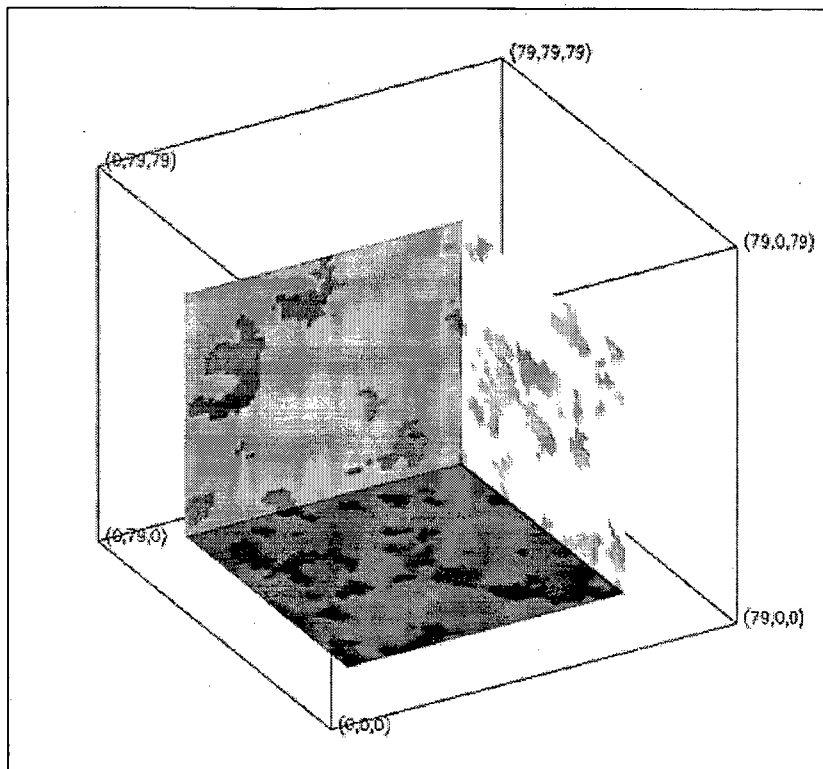


Figure 6.13 - A cutout display of the reconstructed porous structure in Figure 6.11.

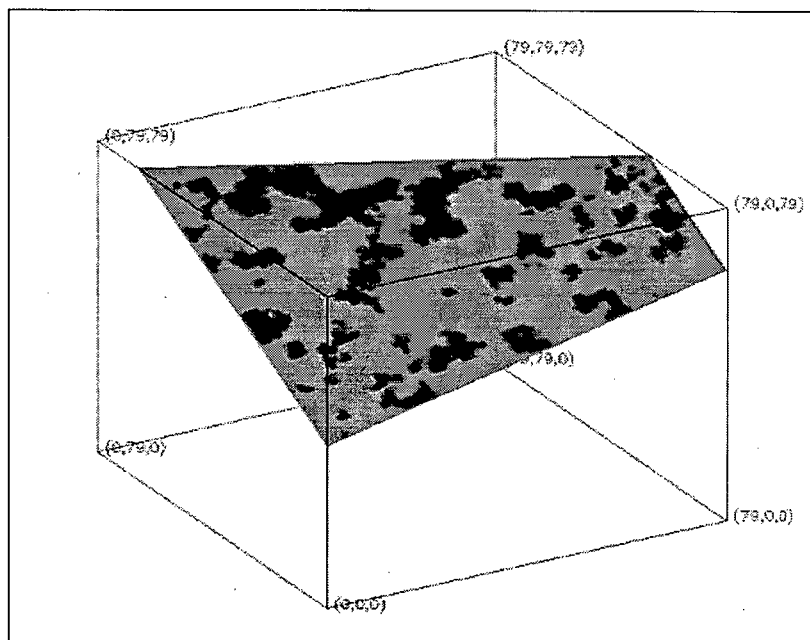


Figure 6.14 - An oblique slice display of the reconstructed porous structure in Figure 6.11.

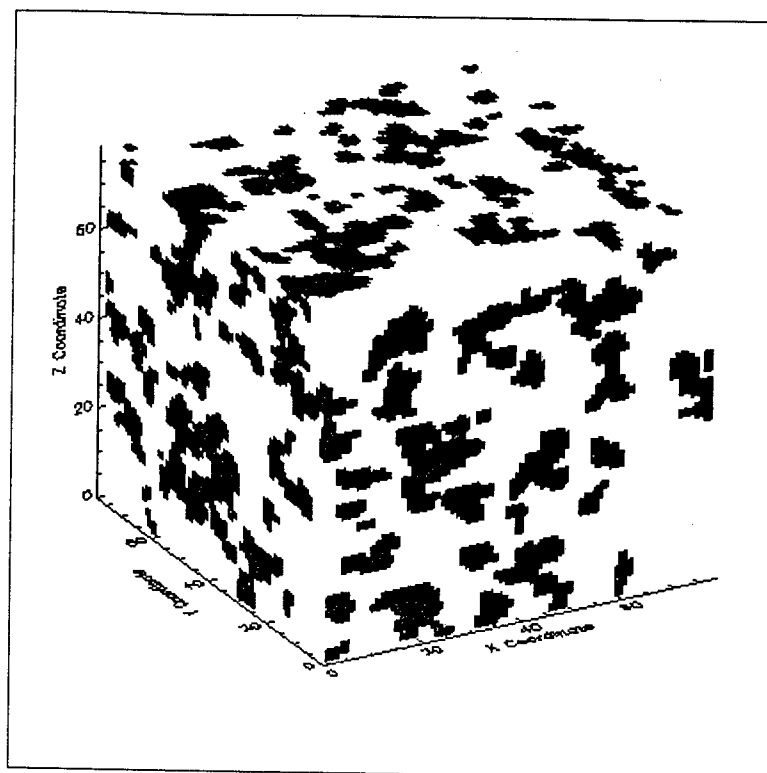


Figure 6.15 - A block display of the reconstructed porous structure in Figure 6.11.

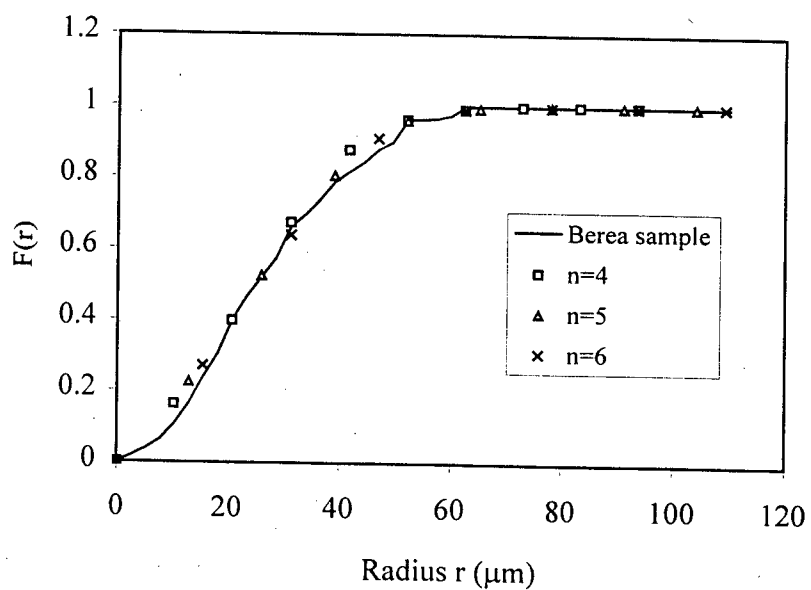


Figure 6.16 - Comparison of pore size distribution function between the sample and the 2-D cross sections of reconstructed porous structure.

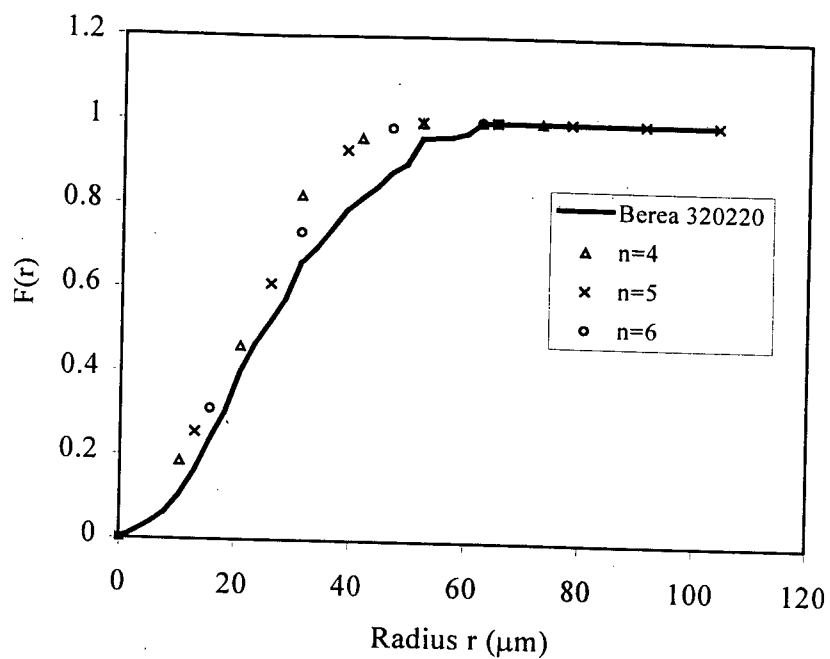


Figure 6.17 - Pore size distribution for 3-D reconstructed porous structure of Berea 320220.

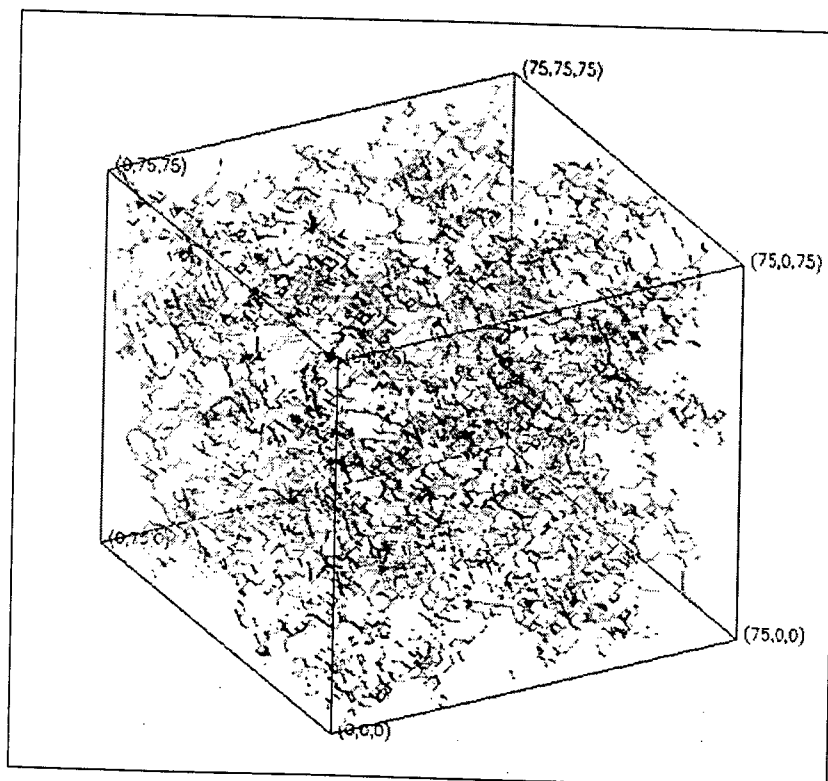


Figure 6.18 - Graph of the reconstructed porous structure for Berea 320220 in Figure 6.11.

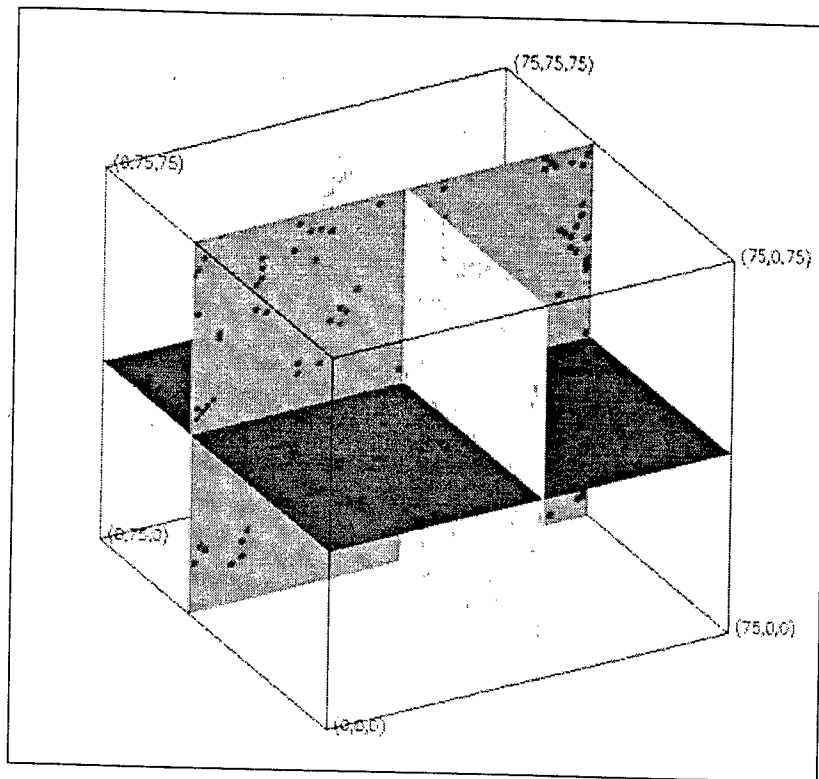


Figure 6.19 - Slice display in three direction of Figure 6.18.

6.2.3. Prediction of Permeability

The skeleton provides a main flow path for single flow, which is classified into nodes and links. When the skeleton is obtained, the simulation of fluid flow is directly carried out on it, as is shown in Figure 6.20. The local cross-sectional area and perimeter normal to the flow path in each link is recorded to compute the local hydraulic radius. Resistance to flow is evaluated for each link. Fluid pressure is calculated at each node, and total volumetric flux through the network is computed. Then, the absolute permeability is predicted from the corresponding network.

In order to avoid the edge effects, the 3-D porous structure is reconstructed with size 120^3 and only the central cube 100^3 is considered. Table 6.4 gives a comparison between predicted permeability in three directions for 500mD Berea 320220. It is observed that the permeability of the porous structure is almost identical in three directions. Therefore, the porous structure is approximately isotropic.

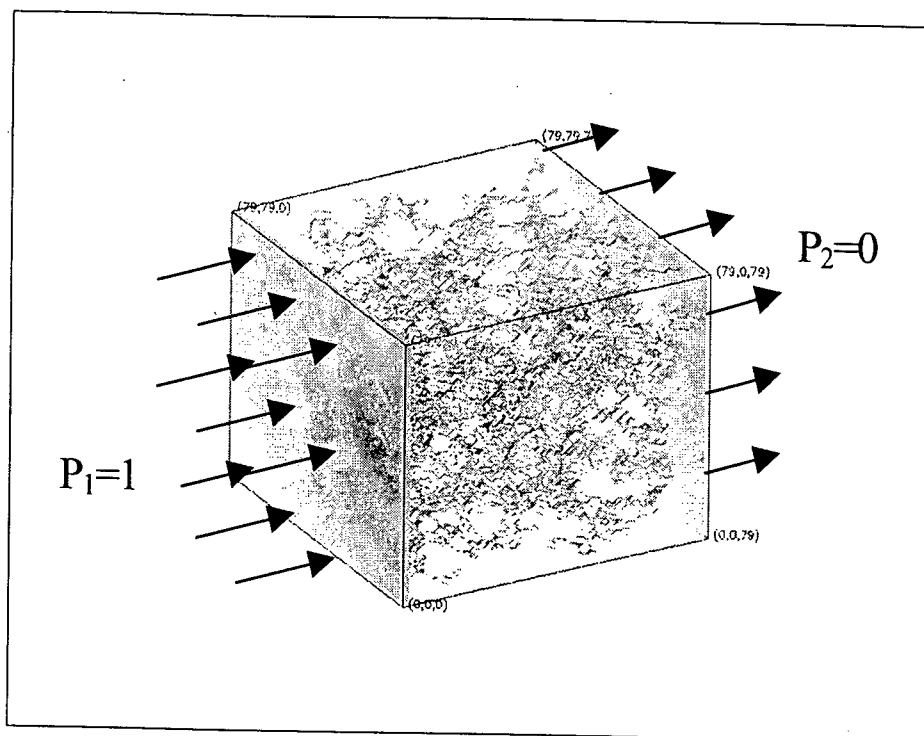


Figure 6.20 - Simulation of fluid flow on the graph of pore space in a porous structure.

Table 6.4 : Comparison of predicted permeability in three directions for 500mD Berea sandstone 320220. ($n=5$, $\zeta=12$ $N=100$).

directions	Node numbers	K (mD)
x	14,004	467.1
y	14,037	439.0
z	13,944	434.8

As discussed in section 3.5.2, from a point of view of the reconstruction of 3-D porous media, the following conditions must be obeyed:

$$1 \ll \frac{\lambda}{n\alpha} \ll \zeta \ll N/2, \quad (6.1)$$

where λ , α , n , ζ and N are correlation length, length per pixel, amplification factor, total length (pixels) of used $R_z(u)$ data and cube size (pixels) of the reconstructed porous medium, respectively. In this section, the effects of three parameters n , ζ and N on the permeability are explored. Table 6.5 gives numerical results for the predicted permeability of Berea 320220 for various different parameters. The influence of n is not generally important, except when n is large. A small value of n means a better description of the fine details of the porous structure. However, small values of n increase ζ and larger sizes N are required, increasing computer storage requirements and processing time. When n is very large, the fine details of the porous structure are lost and this affects the exactness of the geometrical representation associated with the reconstructed porous structure. Table 6.6 gives the effects of n on permeability for Berea 320220. In this table, \aleph is the number of different realizations, using different seeds for the random number generator, \bar{K} the average permeability, calculated from these realizations and σ_K the standard covariance for K . The influence of ζ on the permeability is not important, as is shown in Table 6.7. From Table 6.5, it can be seen that the effect of size N of the reconstructed porous structure is important as it is directly associated to statistical homogeneity of the reconstructed structure. With the increase of N , the estimated permeability tends to converge. Table 6.8 shows the effect of N on prediction of permeability for Berea 320220 ($n=5$, $\zeta=12$). In this table, \bar{K} is the average permeability calculated from five different realizations. As mentioned above, small values of n require larger values of N , increasing computer requirements. Therefore, a compromise has to be made in order to get good results. A stable prediction which fluctuates, for several N , around the experimental value of permeability K was obtained for $n=4$, $n=5$ and $n=6$. For all cases, stable values of permeability were obtained when the ratio of L and D_{\max} are larger than 10. Here D_{\max} is the maximum pore diameter, which can be found in the curve of pore size distribution function (see Figure 6.4). The permeability for various realizations was predicted and is given in Table 6.9.

Table 6.5 : Numerical results of prediction of permeability for Berea 320220 ($\alpha = 2.6 \mu\text{m}$ and $D_{\text{max}} = 124.8 \mu\text{m}$).

n	N	$\frac{L}{D_{\text{max}}}$	Node numbers	K (mD)
4	60	5	2,562	362.2
	80	6.7	6,010	339.9
	100	8.3	12,073	384.9
	120	10	21,488	378.4
	150	12.5	41,819	337.5*
	200	16.6	101,727	340.6*
5	40	4.2	695	339.9
	60	6.25	2,438	409.3
	80	8.3	6,352	406.3
	100	10.4	14,004	467.1
	120	12.5	23,130	432.3
	150	15.6	46,177	447.2*
6	40	5	809	627.2
	60	7.5	2,615	570.7
	80	10	6,935	602.6
	100	12.5	14,422	665.8
	120	15	25,660	639.5
8	30	5	377	2112.1
	40	6.7	926	1496.3
	60	10	3,642	1447.4
	80	12.3	9,385	1489.3

* The data was run in IBM sp2.

Table 6.6 : Effects of n on permeability for 500mD Berea 320220.

n	N	\aleph	\bar{K} (mD)	σ_K	$\frac{\sigma_K}{\bar{K}}$
4	120	5	333.9	32.5	0.09
5	100	5	463.2	24.0	0.05
6	80	5	741.9	26.0	0.04
8	60	2	1425.2	25.1	0.02

Table 6.7 : Effects of ζ on permeability for 500mD Berea 320220
($N=100, n=5, \text{seed} = -1, \alpha=2.6 \mu\text{m}$)

ζ	Node numbers	K (mD)
11	13,572	443.3
12	14,004	467.1
13	14,575	479.9
14	13,630	454.2
15	14,406	475.4
30	13,783	439.4

Table 6.8 : Effects of N on prediction of permeability for 500mD Berea 320220 (n=5, $\zeta=12$).

N	$\frac{L}{D_{\max}}$	\bar{K} (mD)
40	4.2	352.4
60	6.3	444.3
80	8.3	444.9
100	10.4	463.1
120	12.5	452.2
150	15.6	464.3

Table 6.9 : Effects of different configurations on permeability for 500mD Berea 320220 (N=100, n=5, $\zeta=12$, $\alpha=2.6 \mu\text{m}$)

Configuration	Node numbers	K (mD)
No 1	14,082	475.97
No 2	13,798	499.12
No 3	13,125	437.35
No 4	13,439	436.18
No 5	14,004	467.15
Average		463.15

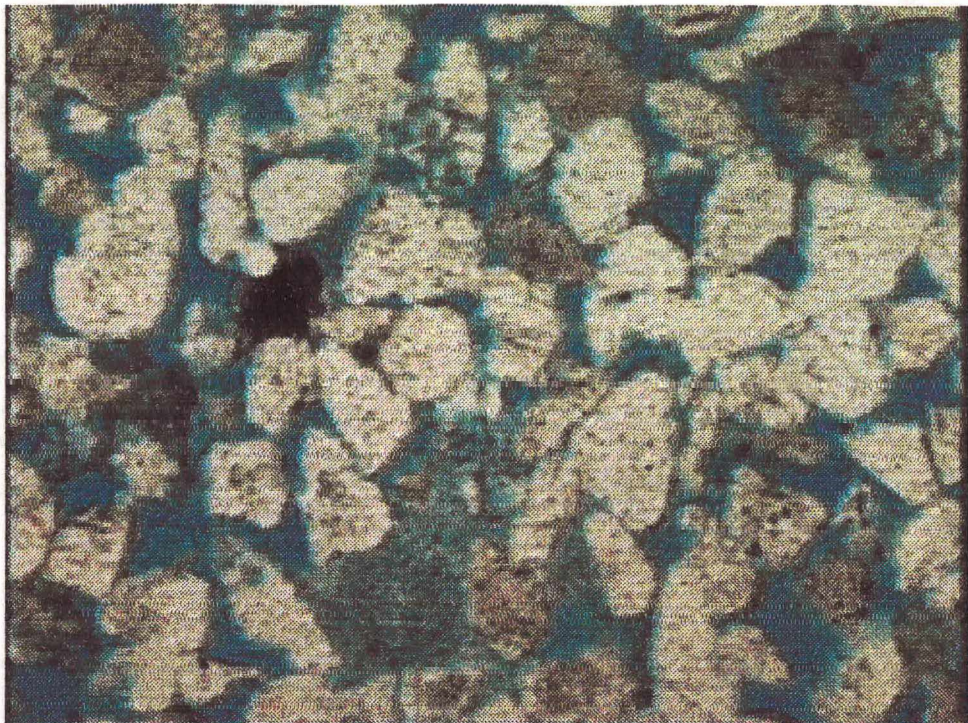
6.3. RESULTS FOR MORE SAMPLES

The simulated value of permeability for Berea 320220 is satisfying when compared with nominal value of the sample. In this section, permeability is calculated for more samples.

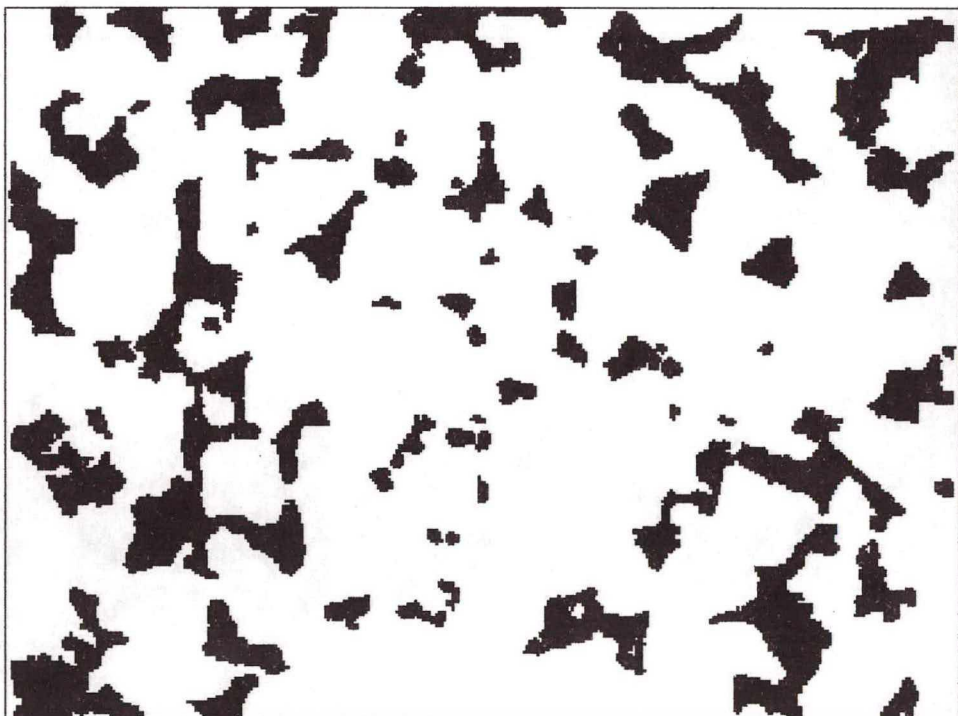
One image of 200 mD and three images of 500 mD Berea sandstone were used, which were obtained by using optical microscopy in CENPES, PETROBRAS. Their original code numbers are 26, 310259, 318238 and 32216, respectively. Therefore, Berea 26, Berea 310259, Berea 318238 and Berea 32216 are used to represent these samples in the following. The porosities of 200mD and 500mD by experiment are 0.193 and 0.225. The color images are shown in Figure 6.21(a), Figure 6.22 (a), Figure 6.23 (a) and Figure 6.24 (a), respectively. They are with magnification of 50 \times . Each pixel corresponds to 2.6 microns. In these images, the black parts may be oils or calcinated materials, and these parts are considered as solid matrix in binarization process with the same as Berea 320220. The obtained color images were segmented using object boundary and image HUE histogram information (Philippi and Fernandes, 1995). The corresponding binary images are shown in Figure 6.21 (b), Figure 6.22 (b), Figure 6.23 (b) and Figure 6.24 (b), respectively. Figure 6.25 - Figure 6.28 show their power spectra of Figure 6.21 (b), Figure 6.22 (b), Figure 6.23 (b) and Figure 6.24 (b), respectively. The Fourier transform method described in chapter 2 was used to characterize 2-D image of the samples. The porosities for all samples are given in Table 6.10. The normalized autocovariance functions for all samples are given in Table 6.11 and shown in Figure 6.29. Figure 6.30 gives pore size distribution functions of all samples obtained by mathematical morphology. For the convenience of comparison, Berea 320220 mentioned in the above section is also included in these tables and figures.

Table 6.10 : Porosity ϵ and porosity of half image ϵ_h for all samples.

Sample type	Sample code	Original code	Porosity, ϵ	Porosity of half image, ϵ_h
200mD Berea sandstone	1	26	0.1989	0.2091
500mD Berea sandstone	2	310259	0.2595	0.2870
	3	318238	0.2366	0.2328
	4	32216	0.2153	0.2484
	5	320220	0.2214	0.2229

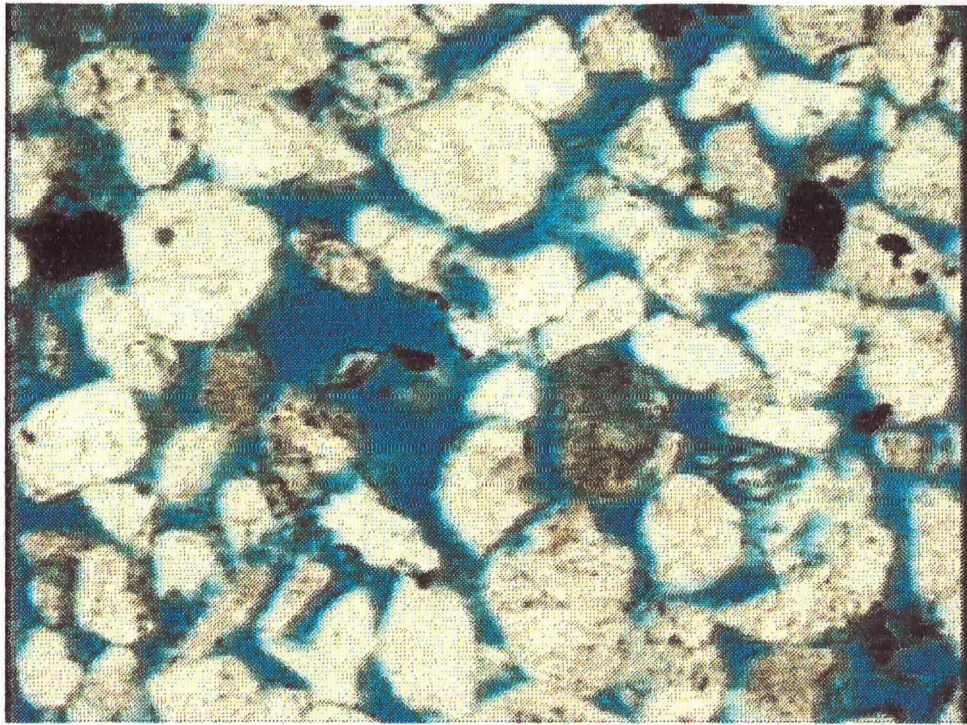


(a)

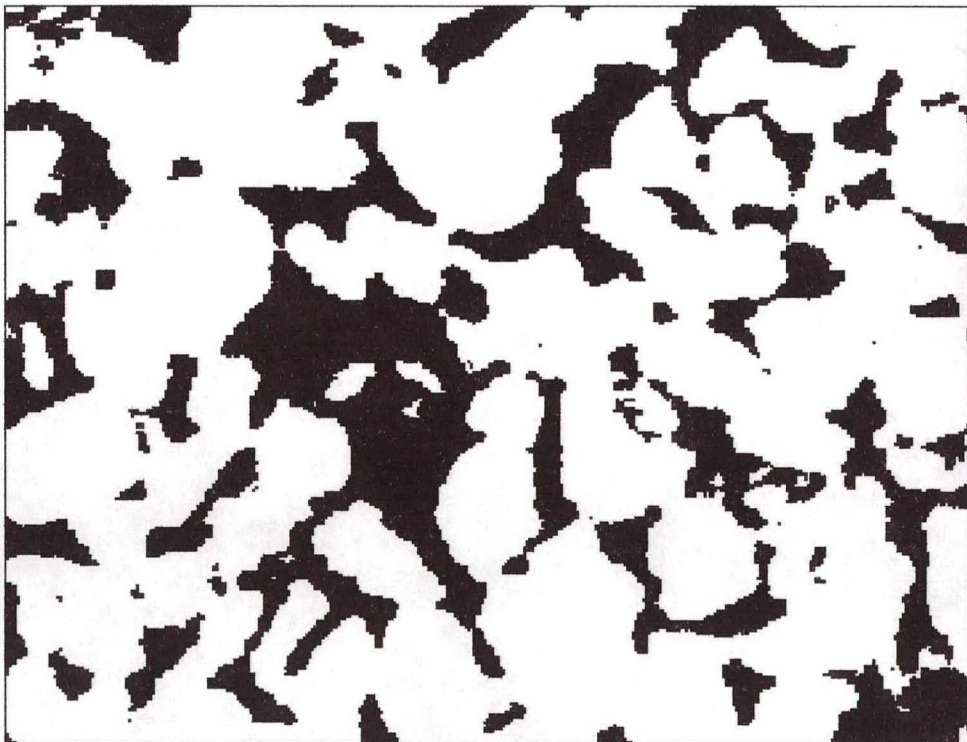


(b)

Figure 6.21 - (a) Digital image of a plane section of 200 mD Berea sandstone. Original code No. is 26. In the following, Berea 26 is used to represent it. It is 640×480 pixels with magnification $50 \times$. (b) its binary image.

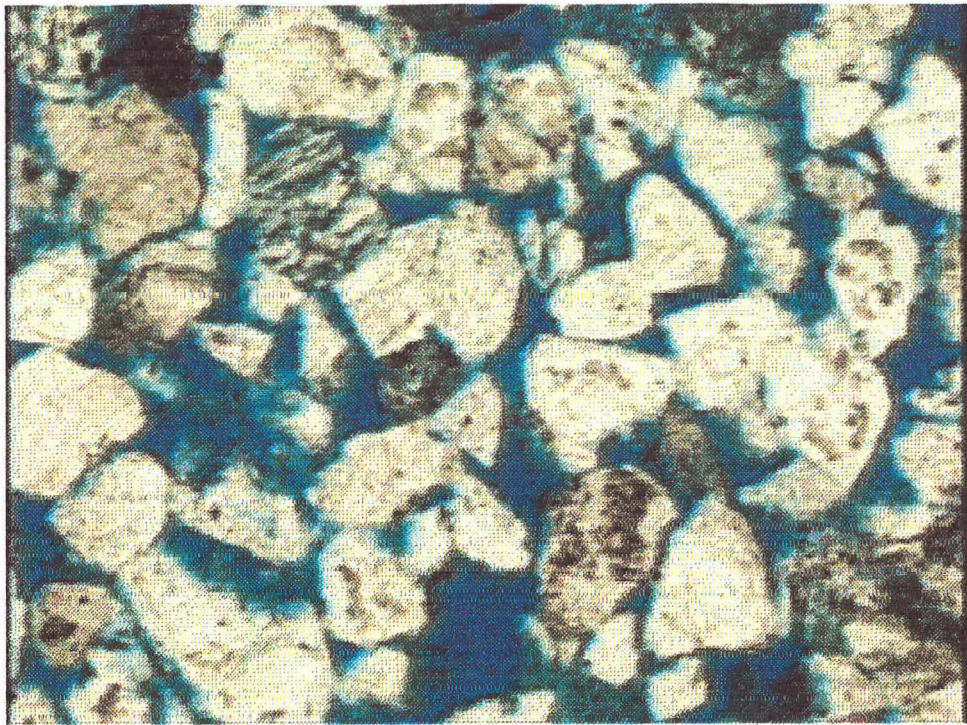


(a)

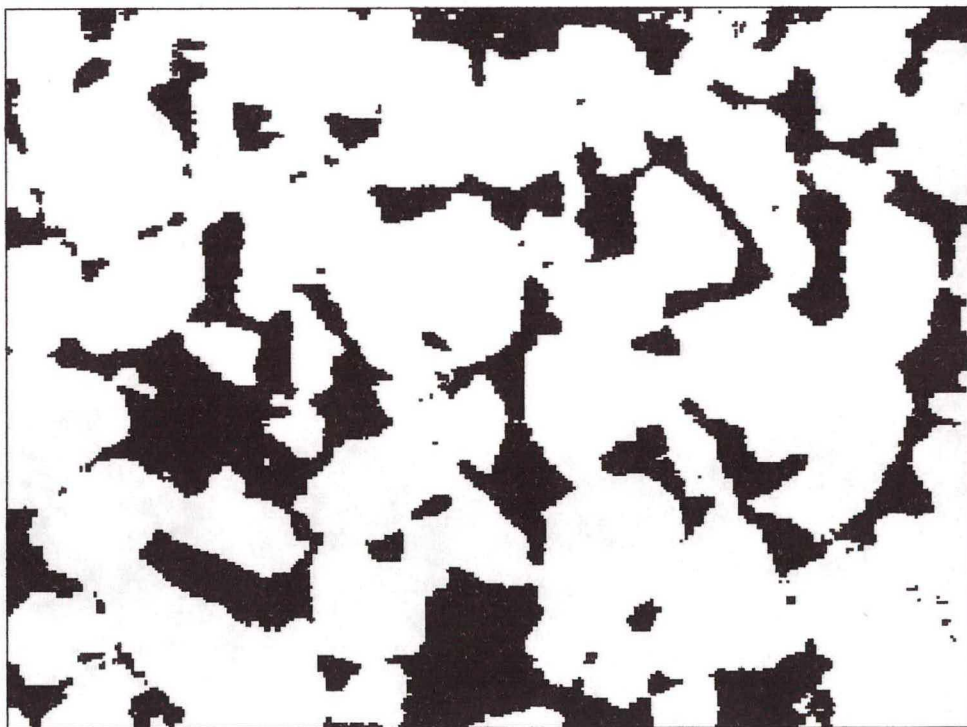


(b)

Figure 6.22 - (a) Digital image of a plane section of 500 mD Berea sandstone. Original code No. is 310259. In the following, Berea 310259 is used to represent it. It is 619×457 pixels with magnification $50 \times$. (b) its binary image.

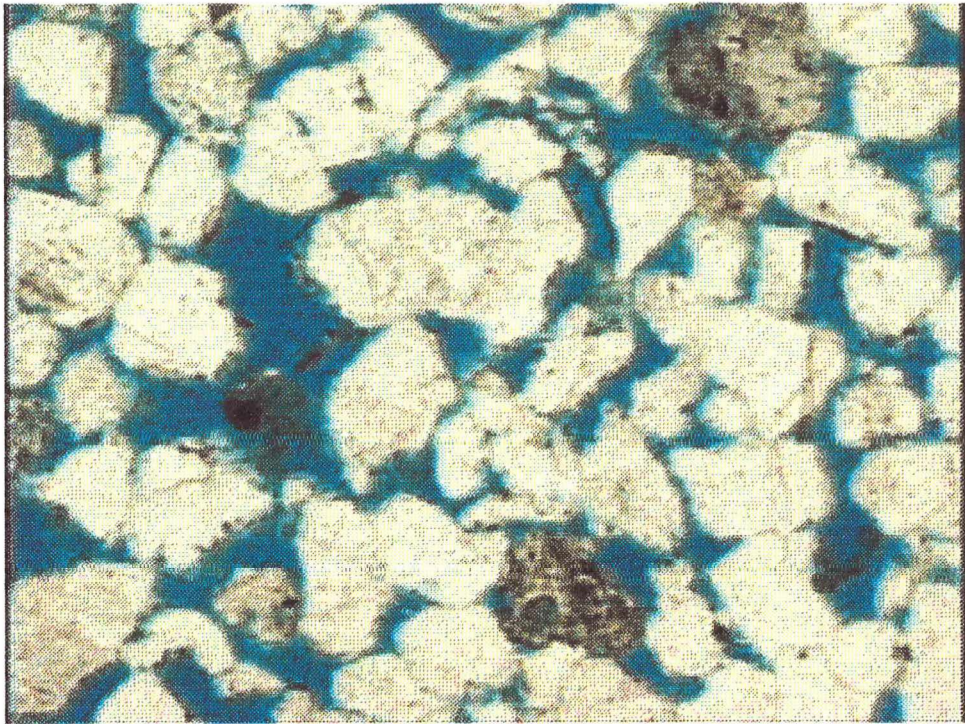


(a)

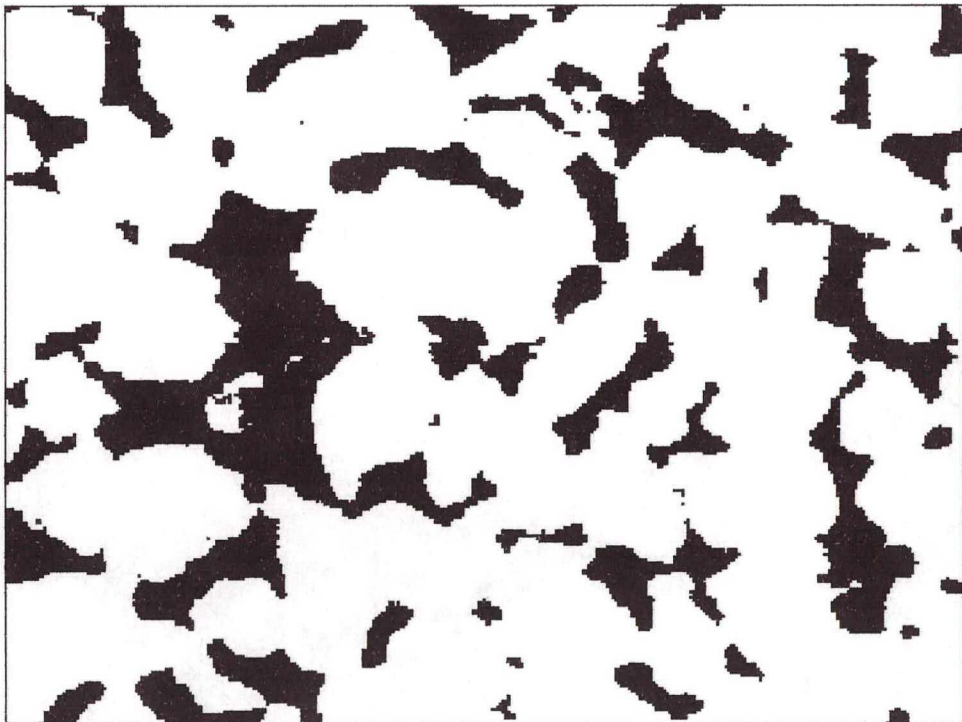


(b)

Figure 6.23 - (a) Digital image of a plane section of 500 mD Berea sandstone. Original code No. is 318238. In the following, Berea 318238 is used to represent it. It is 612×458 pixels with magnification $50 \times$. (b) its binary image.



(a)



(b)

Figure 6.24 - (a) Digital image of a plane section of 500 mD Berea sandstone. Original code No. is 32216. In the following, Berea 32216 is used to represent it. It is 610×460 pixels with magnification $50 \times$. (b) its binary image.

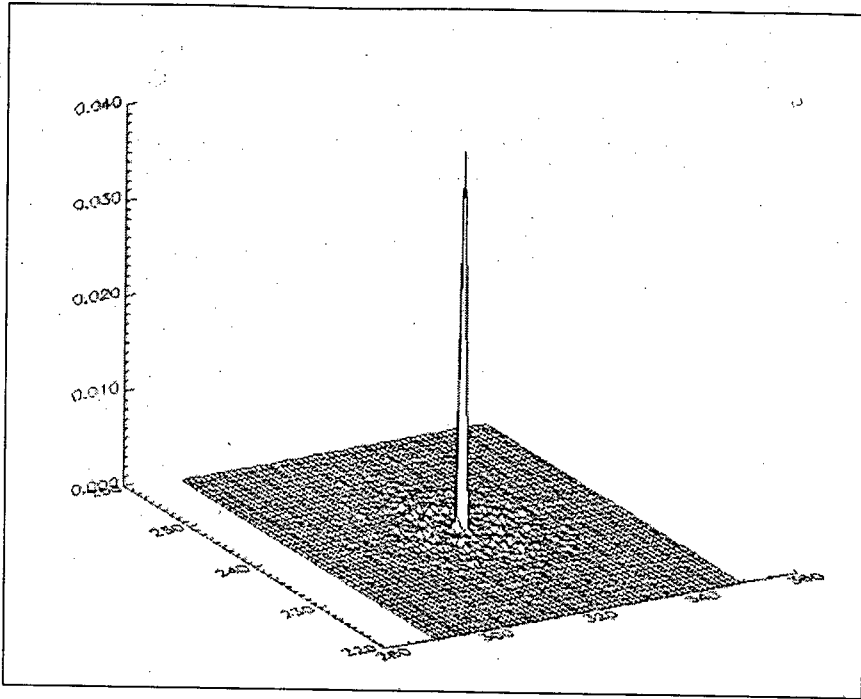


Figure 6.25 - Power spectrum of Figure 6.21 (b).

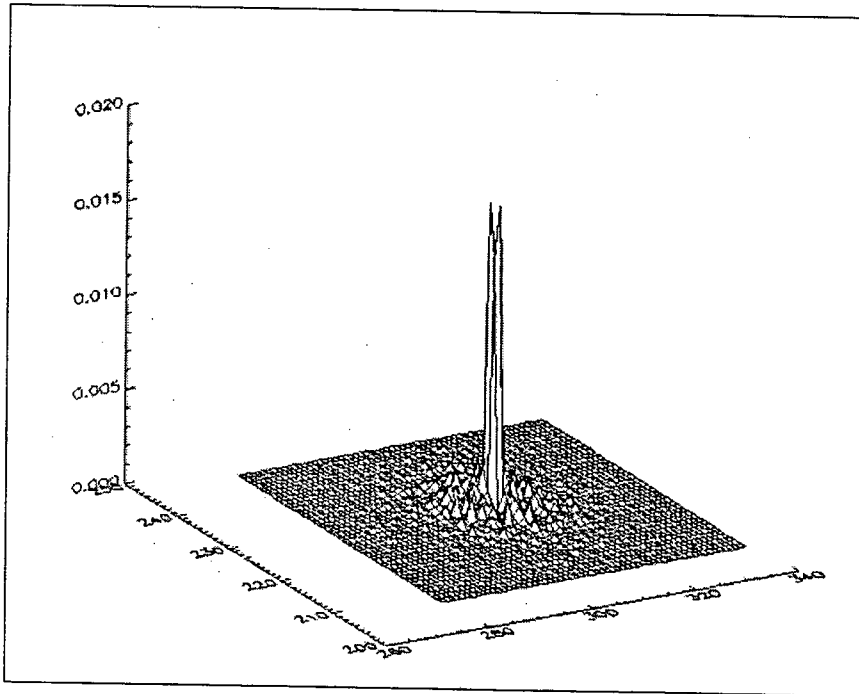


Figure 6.26 - Power spectrum of Figure 6.22(b).

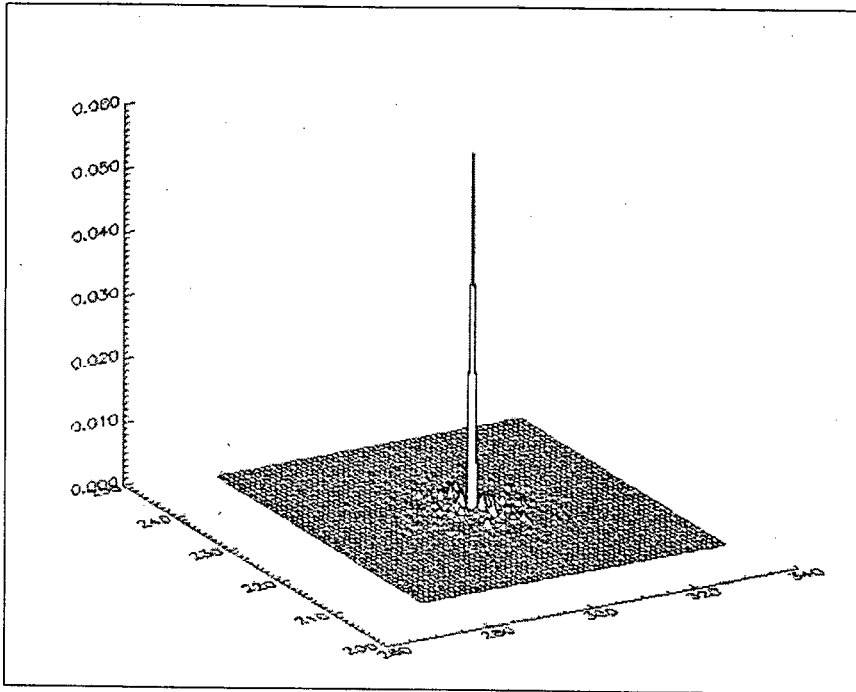


Figure 6.27 - Power spectrum of Figure 6.23 (b).

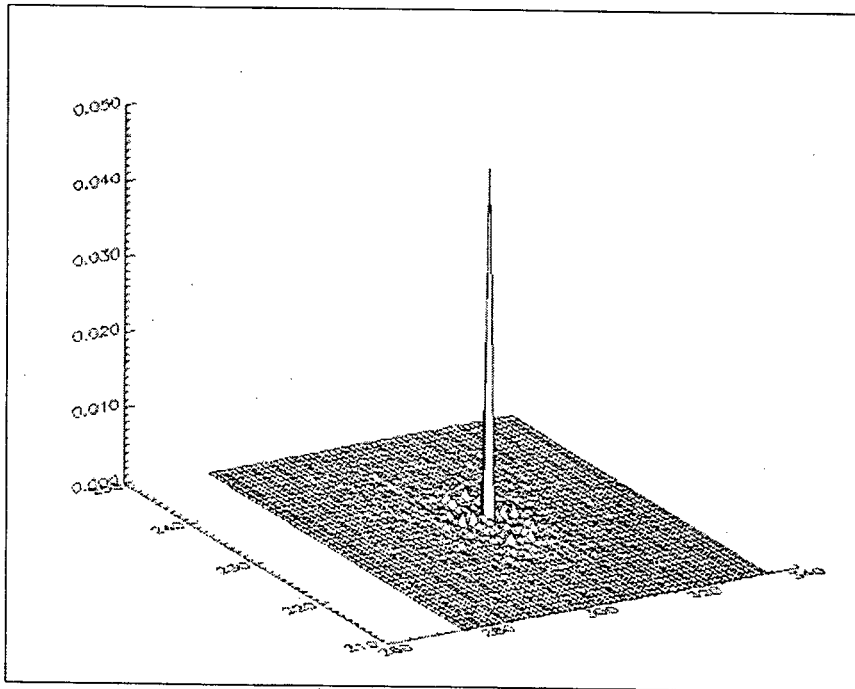


Figure 6.28 - Power spectrum of Figure 6.24 (b).

Table 6.11 : Normalized autocovariance function for all samples.

displacement (μm)	Berea 26	Berea 310259	Berea 318238	Berea 32216	Berea 320220
0	1.0	1.0	1.0	1.0	1.0
13	0.6845	0.7009	0.7269	0.7199	0.7013
26	0.4492	0.4746	0.5251	0.5016	0.4775
39	0.2822	0.3095	0.3740	0.3390	0.3181
52	0.1699	0.1958	0.2634	0.2280	0.2110
65	0.0981	0.1196	0.1835	0.1546	0.1379
78	0.0514	0.0714	0.1262	0.1078	0.0886
91	0.0188	0.0450	0.0899	0.0749	0.0569
104	-0.0026	0.0289	0.0688	0.0509	0.0362
117	-0.0147	0.0196	0.0564	0.0327	0.0215
130	-0.0191	0.0170	0.0476	0.0198	0.0098
143	-0.0164	0.0174	0.0390	0.0103	0.0020
156	-0.0103	0.0167	0.0306	0.0050	-0.0016
169	-0.0069	0.0133	0.0221	0.0026	-0.0027
182	-0.0053	0.0098	0.0141	0.0014	-0.0019
195	-0.0043	0.0073	0.0058	0.0019	0.0017
208	-0.0022	0.0066	0.0011	0.0027	0.0060
221	0.0036	0.0060	0.0009	0.0041	0.0103
247	0.0199	0.0006	0.0030	0.0072	0.0121
260	0.0265	-0.0016	0.0002	0.0055	0.0111
273	0.0310	-0.0015	-0.0003	0.0022	0.0102
286	0.0329	0.0004	0.0022	-0.0022	0.0120
299	0.0312	0.0042	0.0041	-0.0080	0.0137

Table 6.11 (Continued).

displacement (μm)	Berea 26	Berea 310259	Berea 318238	Berea 32216	Berea 320220
312	0.0281	0.0070	0.0035	-0.0125	0.0135
325	0.0248	0.0057	0.0027	-0.0144	0.0124
338	0.0198	0.0016	0.0015	-0.0172	0.0109
351	0.0147	-0.0019	0.0003	-0.0207	0.0085
364	0.0115	-0.0054	0.0020	-0.0235	0.0052
377	0.0095	-0.0072	0.0057	-0.0250	0.0015
390	0.0086	-0.0075	0.0091	-0.0248	-0.0006
403	0.0066	-0.0063	0.0118	-0.0219	-0.0028
416	0.0042	-0.0034	0.0144	-0.0171	-0.0056
429	0.0017	-0.0005	0.0174	-0.0108	-0.0081
442	0.0002	-0.0015	0.0209	-0.0042	-0.0108
455	-0.0009	-0.0068	0.0234	0.0014	-0.0146
468	0.0007	-0.0162	0.0228	0.0058	-0.0180
481	0.0028	-0.0256	0.0198	0.0090	-0.0199
494	0.0028	-0.0322	0.0163	0.0086	-0.0211
507	0.0008	-0.0371	0.0128	0.0063	-0.0210
520	-0.0005	-0.0404	0.0112	0.0047	-0.0201
533	-0.0010	-0.0427	0.0108	0.0033	-0.0190
546	-0.0015	-0.0433	0.0108	0.0013	-0.0179
559	-0.0030	-0.0427	0.0113	-0.0014	-0.0178
572	-0.0026	-0.0395	0.0120	-0.0040	-0.0189
585	-0.0004	-0.0332	0.0122	-0.0058	-0.0214

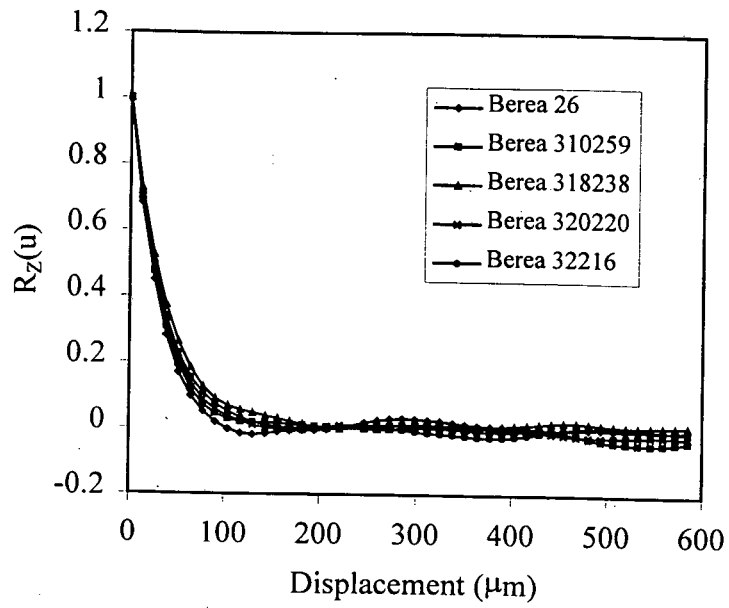


Figure 6.29 - Normalized autocovariance function for all samples.

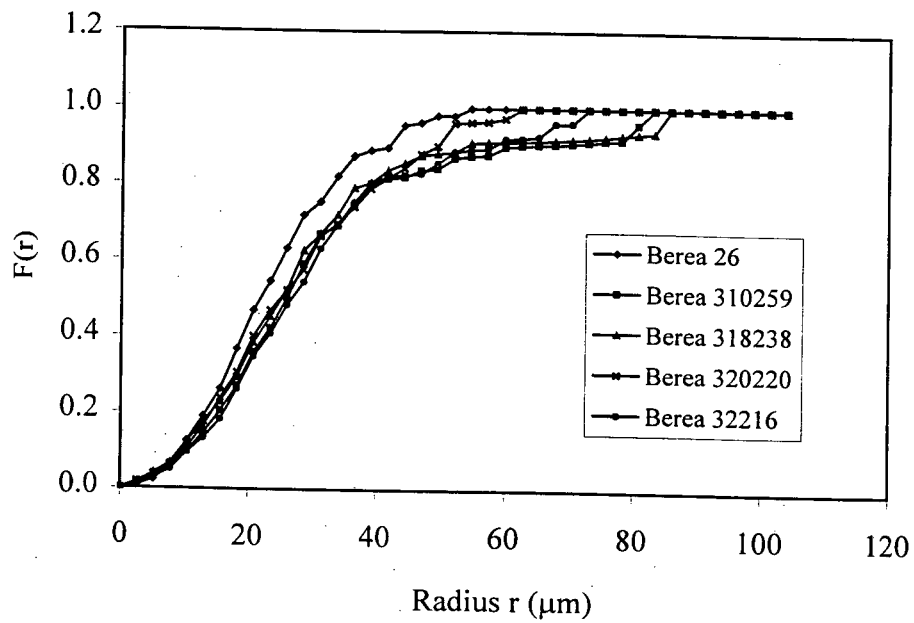


Figure 6.30 - Pore size distribution function for all samples.

The 3-D porous structures and skeletons for the four samples were obtained by the same method as discussed in section 6.2.2. From the discussion in section 6.2, it is important that the side length L of the reconstructed porous structure should be much larger than maximum pore diameter D_{\max} . For example, L/D_{\max} is 10 (see Table 6.5). The permeability was calculated for four samples. Considering computer memory and running time at a typical workstation, the following reconstruction parameters were used:

$N=105$, $n=4$ and $\zeta = 10$ for 200mD Berea sandstone,

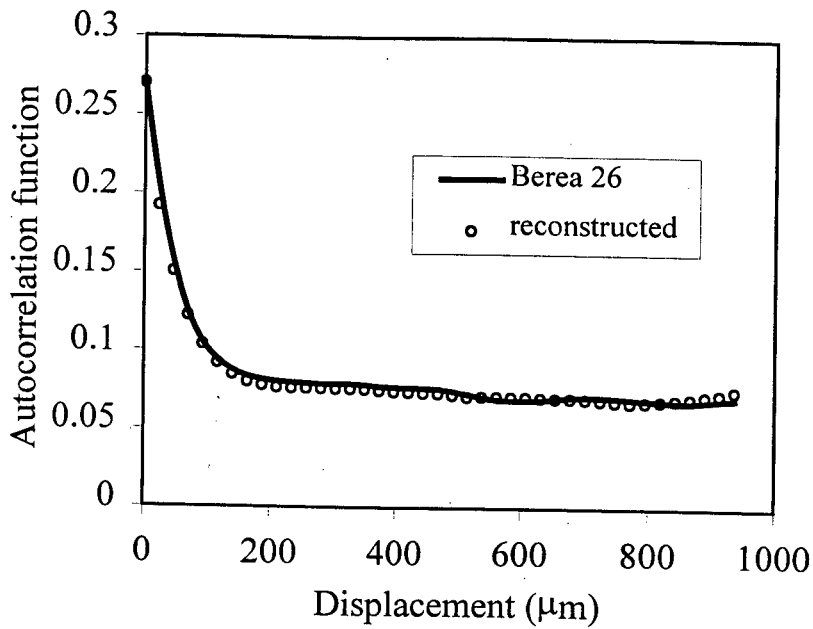
and

$N=100$, $n=5$ and $\zeta = 12 - 22$ for 500mD Berea sandstones.

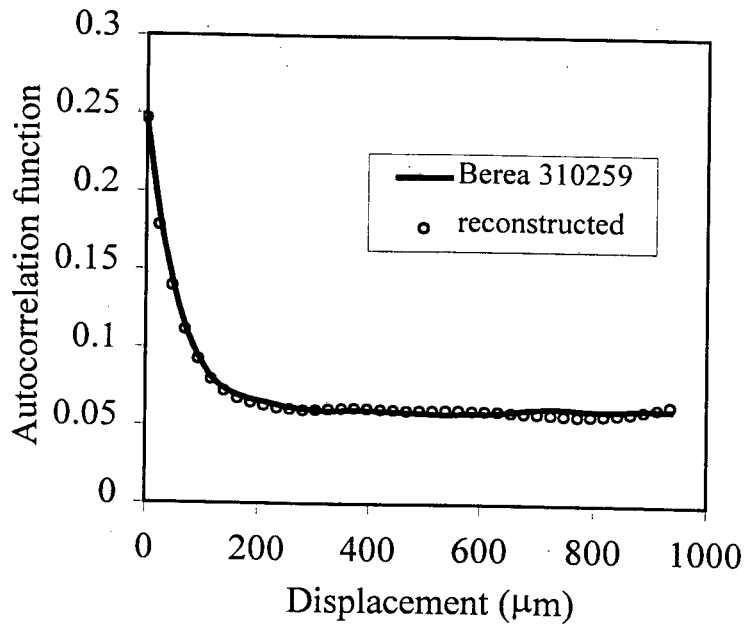
Comparison of porosity and autocorrelation function of the reconstructed porous structures with original samples, 3-D visualization of the reconstructed porous structures and corresponding skeletons are shown in Table 6.12, Figure 6.31, Figure 6.32 and Figure 6.33, respectively.

Table 6.12: Comparison of porosity ε of reconstructed porous structures for all samples with the original.

Sample code	Reconstructed	Original
Berea 26 (200 mD)	0.1980	0.1989
Berea 310259 (500 mD)	0.2600	0.2595
Berea 318238 (500 mD)	0.2368	0.2366
Berea 32216 (500 mD)	0.2155	0.2153
Berea 320220 (500 mD)	0.2228	0.2214

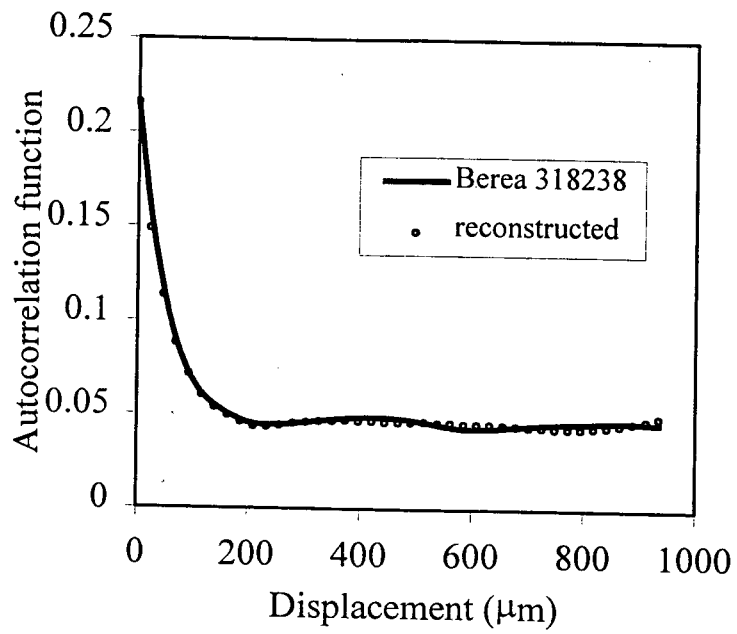


(a)

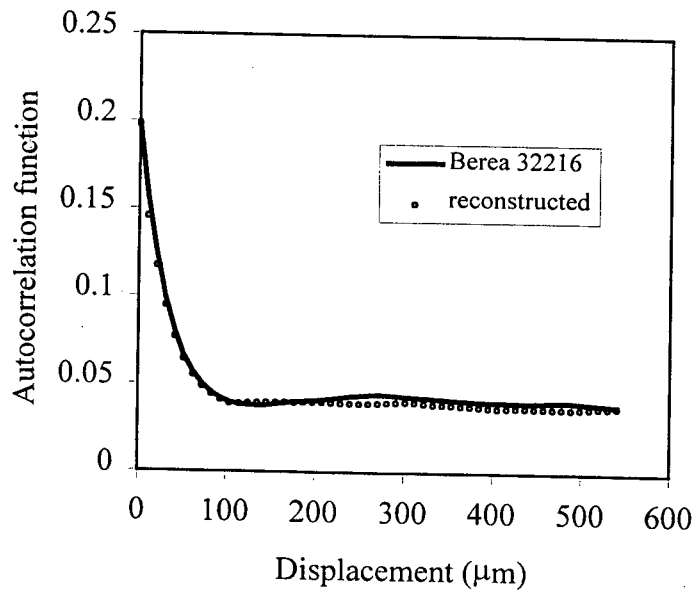


(b)

Figure 6.31 - Comparison of autocorrelation functions between reconstructed porous structures and samples: (a) Berea 26 (b) Berea 310259 (c) Berea 318238 (d) Berea 32216.

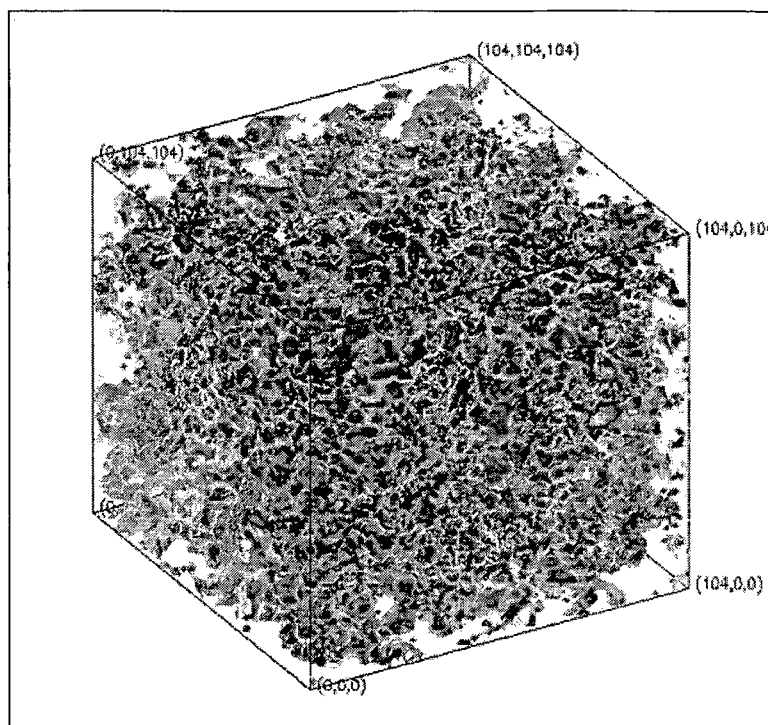


(c)

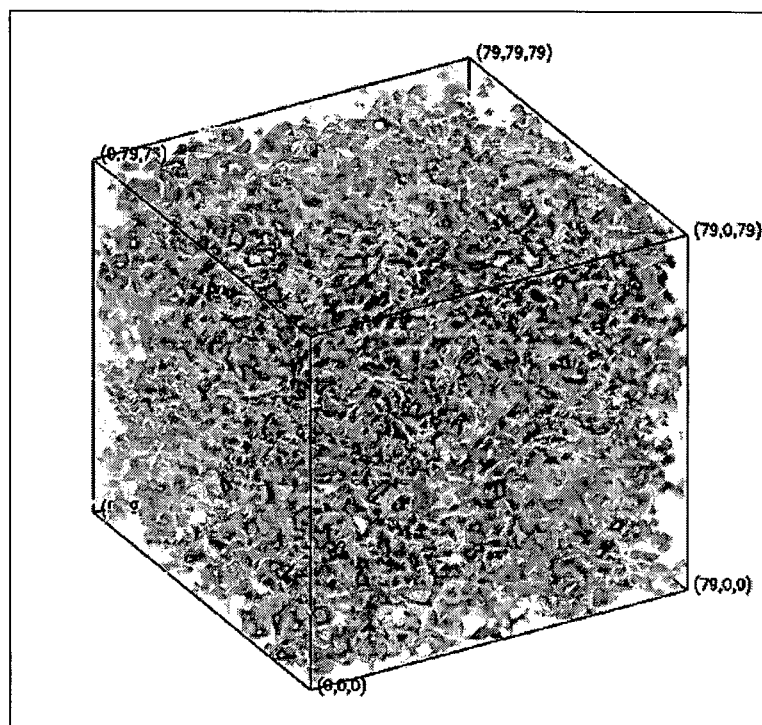


(d)

Figure 6.31 (continued).

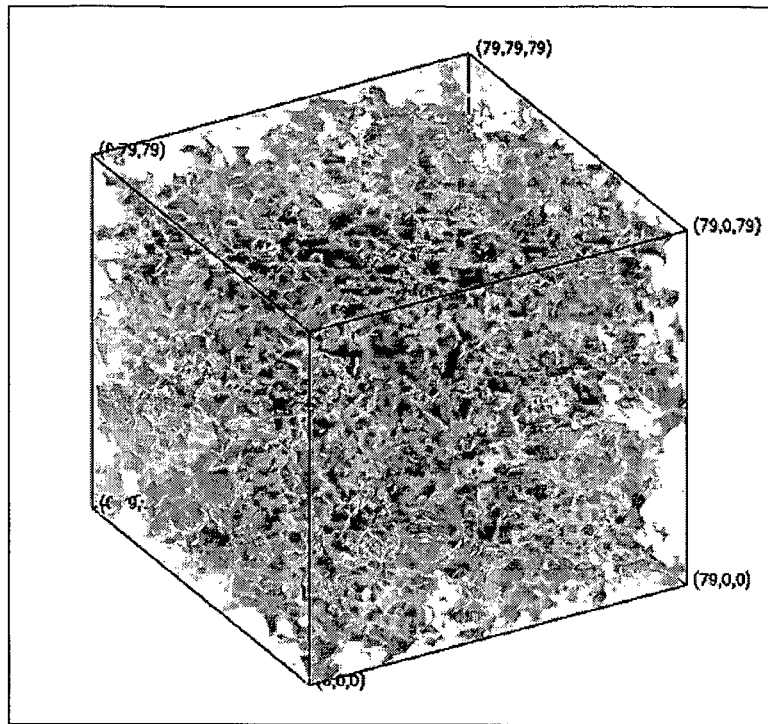


(a)

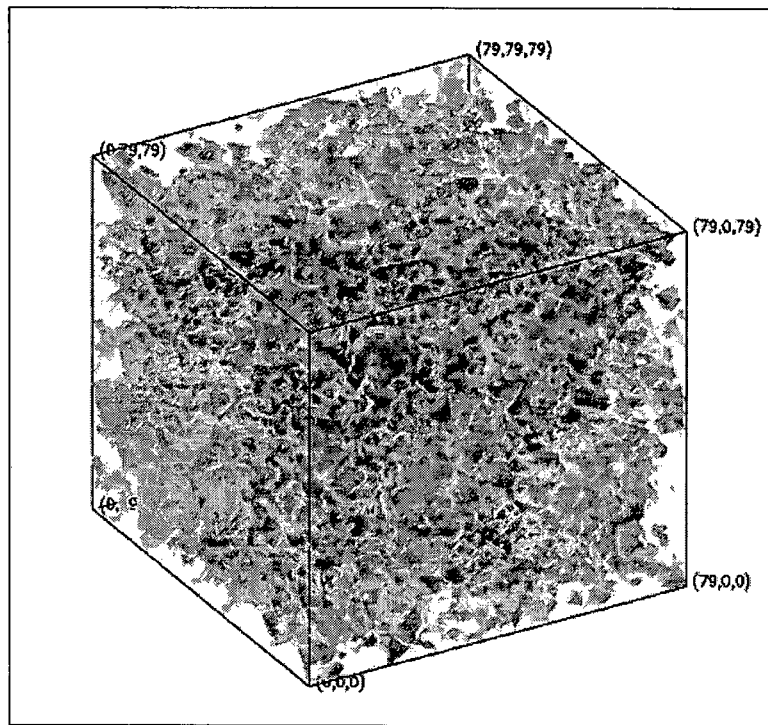


(b)

Figure 6.32 - The reconstructed porous structures for four samples: (a) Berea 26 (b) Berea 310259 (c) Berea 318238 (d) Berea 32216.

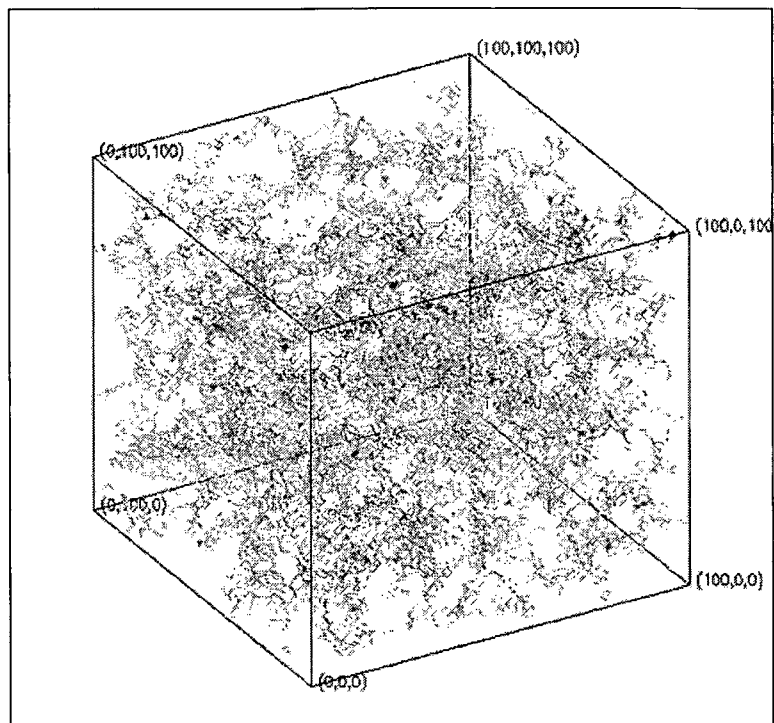


(c)

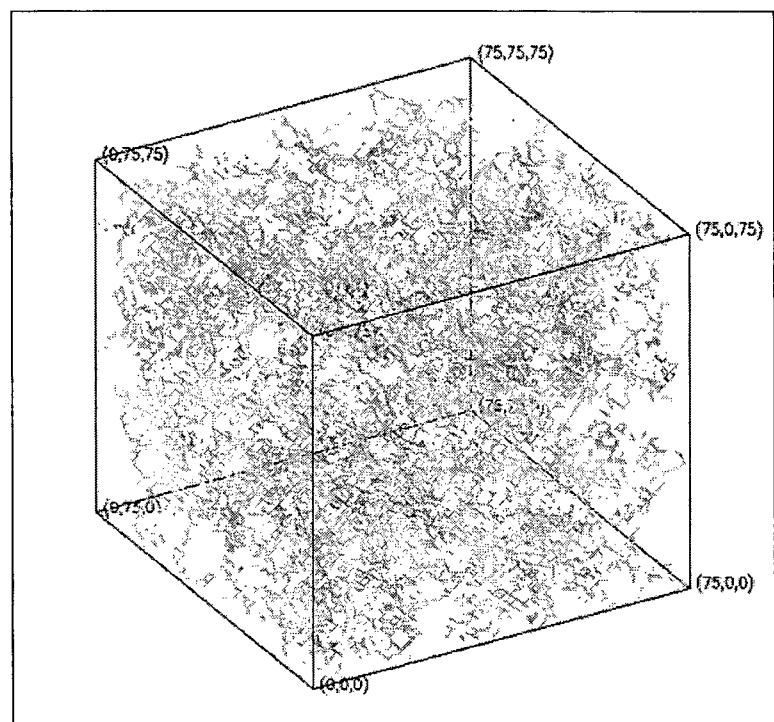


(d)

Figure 6.32 (continued).

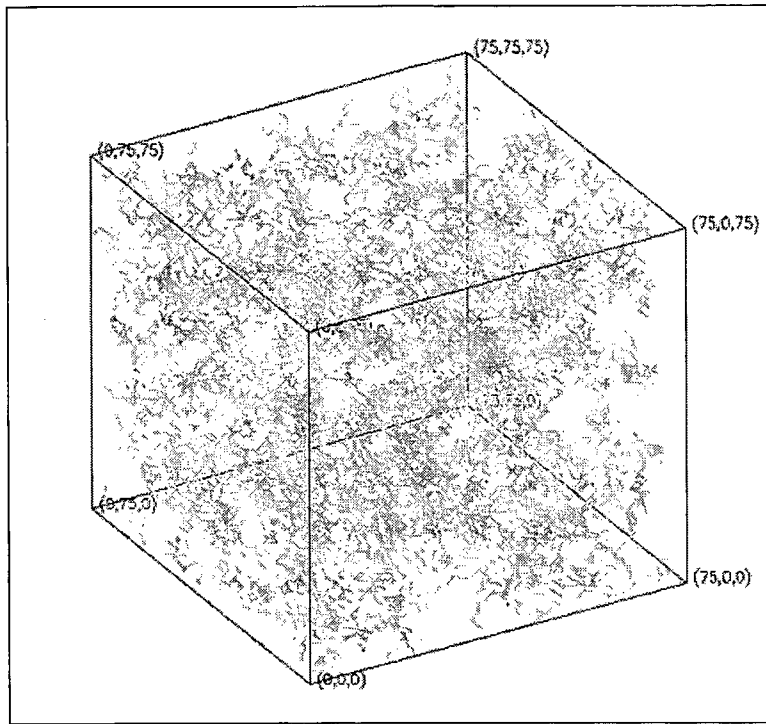


(a)

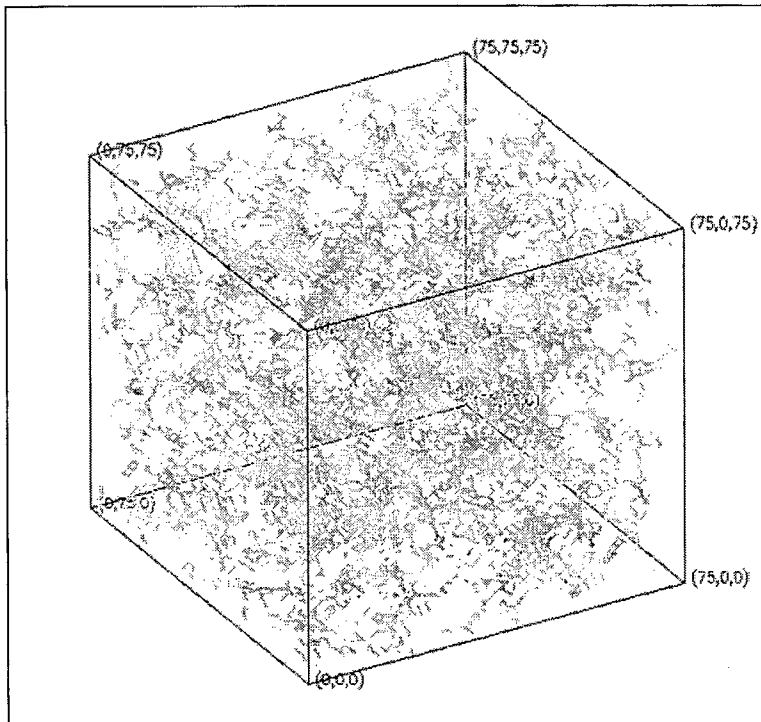


(b)

Figure 6.33 - 3-D graph of pore space for reconstructed porous structures for four samples: (a) Berea 26 (b) Berea 310259 (c) Berea 318238 (d) Berea 32216.



(c)



(d)

Figure 6.33 (continued).

The results of predicting permeability for all samples are given in Table 6.13. In this table, the Berea M-1 is an artificial sample using the average porosity and average autocorrelation function of four 500 mD samples – Berea 310259, 318238, 320220 and 32216. The mean porosity is 0.2342. \aleph is the number of realizations using different random seeds.

Table 6.13 : Numerical results when predicting permeability for 200mD and 500 mD Berea sandstone samples.

Sample code	Sample code	n	N	ζ	\aleph	K (mD)		
						Minimum	Maximum	Average
200mD Berea sandstone	26	4	105	10	5	200.4	233.5	214.3
500mD Berea sandstone	310259	5	100	19	5	674.4	734.1	704.6
	318238	5	100	16	5	443.7	604.4	540.8
	320220	5	100	12	5	436.1	569.9	510.1
	32216	5	100	14	5	389.6	447.4	422.2
	M-1*	5	100	26	5	445.6	489.7	469.5

*M-1 is an artificial sample using the average porosity and average autocorrelation function of four 500 mD samples – Berea 310259, 318238, 320220 and 32216.

6.4. DISCUSSIONS

6.4.1. Permeability as Function of Porosity and Autocorrelation Function

The main advantage of the present method for characterizing porous media is that it provides a set of well-defined functions of increasing complexity for the geometrical description of the porous structure. One usually uses the second autocorrelation function (Quiblier, 1986; Adler *et al.*, 1990; Fernandes, 1994). Estimated values for permeability from four sections of 500 mD Berea sandstone, one section of 200 mD Berea sandstone and Fontainebleau sandstone, together with their original porosity and correlation length, can be

concluded in Table 6.14. The correlation length λ is defined by $\lambda = \int_0^{\infty} R_z(u) du$ (Lantuéjoul, 1991; Ioannidis *et al.*, 1996). The effect of porosity is as expected, increasing permeability for different samples with the same geological genesis. Permeability increases with porosity and correlation length. In fact, as it is well known, permeability does not depend only on porosity. For instance, Berea sandstone (310259) and Fontainebleau sandstone have almost the same porosity, but permeability of Fontainebleau sandstone is larger due to its longer correlation length.

Table 6.14 : Relation of permeability with porosity and correlation length.

Samples	porosity	λ (μm)	Permeability (mD)
Berea 320220 (500 mD)	0.2214	34.19	463.1
Berea 310259 (500 mD)	0.2595	34.24	704.6
Berea 318238 (500 mD)	0.2366	40.99	540.8
Berea 32216 (500 mD)	0.2153	37.06	422.2
Berea 26 (200 mD)	0.1989	31.52	214.3
Fontainebleau GF2 (2700 mD)	0.25	65.05	1,984.1

As it can be concluded from Table 6.5 comparing the results obtained using $n=4$ and $n=5$, the simulation using the amplification factor $n=5$ is in better agreement with the nominal value of permeability for Berea 500 mD. This was, somewhat, surprising since more detailed porous cavities are included for $n=4$. A possible reason is related to the lower porosity of the sample image Berea 320220 (0.2214), which was used in reconstructing the porous structure, with respect to the experimental value for Berea 500 mD (0.225). Another possibility is related with the reconstruction method itself. Although autocorrelation function provides much more information about the geometry than the porosity, many important properties of the medium (such as pore size distribution) may be buried in higher order functions. High-order moments larger than two of the phase function for reconstructed porous media should be verified in future research. The mean pore size distribution of all section of reconstructed porous media for $n=5$ and $n=6$ are in better agreement with the image in study than the one for

$n=4$, as shown in Figure 6.16. In this figure, comparison is made between the original measured pore size distribution and the mean pore size distribution obtained from several serial sections of the reconstructed porous structure. But larger n results in increasing the error when calculating local hydraulic radius.

To summarize, the amplification factor $n=5$ was chosen for Berea 500 mD. In fact, it gave a better description of the pore size distribution measured on the original image and was more suitable from the point of view of computer running time and memory requirements. This choice cannot, however, be considered as the better one. According to the above discussions, reconstruction parameters $N=105$, $n=4$ and $\zeta=10$ were used to predict the permeability for 200mD Berea sandstone.

6.4.2. Graph of Porous Structure

The thinning algorithm used in this work preserves topology. Visual examination shows that it works adequately. Because of the complexity of 3-D pore structure, it was found that the 3-D skeleton is uncertain of the good unit-width like 2-D skeleton in the discrete space. For example, connectivity was treated and extended to the next-nearest neighbors in the previous thinning algorithms. A simple example in 2-D is displayed in Figure 6.34. This final stage of thinning, at which Figure 6.34 (a) was treated as Figure 6.34 (b), was generally used in previous thinning algorithms (e.g., Thovert *et al.*, 1993). Considering that it may change the topological property in 3-D, one should not delete the points to get a single line. The corresponding penalty is the increase of node numbers. It causes the time-consuming to solve the pressure equations of the network. In this work, we do not emphasize on coordination number distribution and the pore "size" distribution to characterize the 3-D pore structure because the flow problem does not depend only on them. In the previous works, these characterizations for porous media were usually carried out. Once these data are obtained, various models, such as network model, are used to study the macroscopic properties. The advantage of this work is to directly extract the real graph of 3-D pore structure and calculate the permeability, combining with corresponding local hydraulic radius at each point in the graph. Therefore, good algorithm for extracting skeleton of 3-D porous media forms a basis for this work.

0	0	0	0	0	1	1	1	0	0
1	1	1	1	1	1	0	1	0	0
0	1	1	1	1	0	0	1	0	0
0	1	1	1	1	1	1	1	0	0
1	1	0	0	1	1	1	1	0	0
1	1	0	0	1	1	1	1	1	1
1	1	1	1	1	1	1	1	1	1
1	1	1	1	1	1	1	1	1	1
1	1	1	0	0	0	0	0	0	0
1	1	1	0	0	0	0	0	0	0

(a)

0	0	0	0	0	1	1	1	0	0
1	1	1	1	1	1	0	1	0	0
0	1	1	1	1	0	0	1	0	0
0	1	1	1	1	1	1	1	0	0
1	1	0	0	1	1	1	1	0	0
1	1	0	0	1	1	1	1	1	1
1	1	1	1	1	1	1	1	1	1
1	1	1	1	1	1	1	1	1	1
1	1	1	0	0	0	0	0	0	0
1	1	1	0	0	0	0	0	0	0

(b)

Figure 6.34 - A display of the final stage of thinning in 2-D case. 0 represents solid phase, 1 and 1 pore phase and 1 skeleton.

6.4.3. Comparison of Permeability with Empirical Correlations

The experimental data for Berea sandstone were obtained by Brazilian Petroleum Company (CENPES/PETROBRAS, 1995). The experimental porosity for 200 mD and 500 mD Berea sandstone by mercury intrusion is 0.193 and 0.225, respectively. The capillary pressure curves of mercury intrusion for two samples are shown in Figure 6.35. Figure 6.36 gives the corresponding mercury volume distributions as diameter calculated from Laplace's equation. The breakthrough capillary pressures and breakthrough diameters were extracted from these data. Using these breakthrough capillary pressures and breakthrough diameters, the two empirical correlations (Eq. 5.13 and Eq. 5.14) were used to estimate the permeability. Mendes (1997) used the cut-and-rejoin-type model and also calculated the permeability for these two samples from these experimental data. The values are given and compared with our results and experimental ones for the two samples in Table 6.15 and Table 6.16, respectively. In Table 6.15, the predicted permeability for 200mD Berea sandstone of this work is the average for five realizations using reconstruction parameters $N=105$, $n=4$ and $\zeta=10$. In Table 6.16, the predicted permeability for 500mD Berea sandstone is the average taken from four

sections of the sample. It is shown that present results are in very good agreement with Dullien's model.

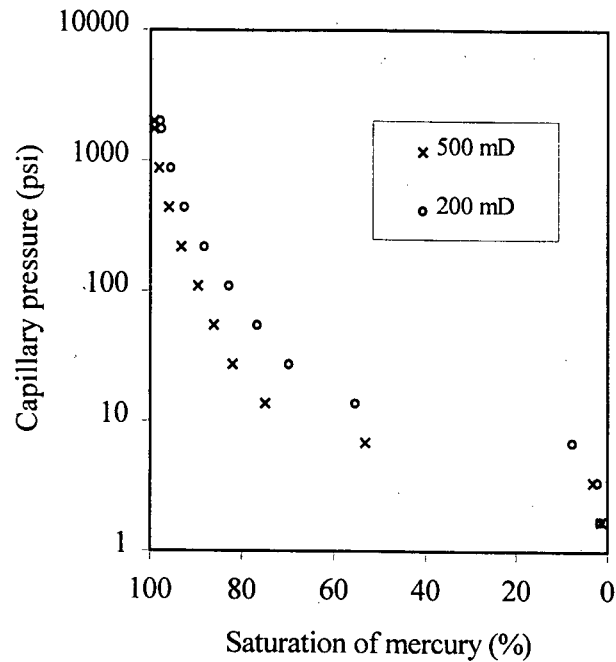


Figure 6.35 - Capillary pressure of mercury intrusion for 200 mD and 500 mD Berea sandstones (CENPES/PETROBRAS, 1995).

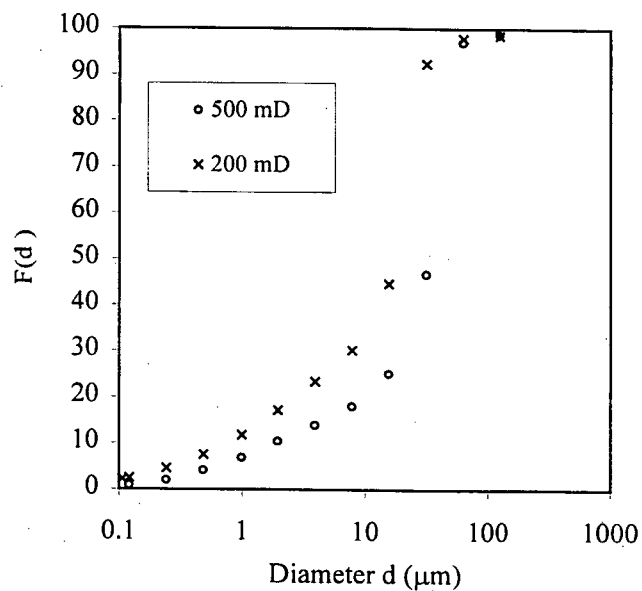


Figure 6.36 - Distribution of pore diameters for 200 mD and 500 mD Berea sandstones (CENPES/PETROBRAS, 1995).

Table 6.15 : Comparison of the result for 200 mD Berea sandstone with empirical permeability correlation. (Experimental data are: $\varepsilon=0.193$, $P_{cb}=10.24$ psi and $D_b=20.87$ μm).

Methods	K (mD)
$K = \left(\frac{D_b}{3.5}\right)^2 \left(\frac{\varepsilon}{32}\right) \times 10^3$ (Dullien, 1992)	215
$K = \left(\frac{85.63}{P_{cb}}\right)^{2.71}$ (Chatzis, 1980)	316
Mendes (1997)	171 ~ 342
This work	214.3
Nominal (CENPES/PETROBRAS, 1995)	200

Table 6.16 : Comparison of the result for 500 mD Berea sandstone with empirical permeability correlation. (Experimental data are: $\varepsilon=0.225$, $P_{cb}=6.83$ psi and $D_b=31.25$ μm).

Methods	K (mD)
$K = \left(\frac{D_b}{3.5}\right)^2 \left(\frac{\varepsilon}{32}\right) \times 10^3$ (Dullien, 1992)	560.5
$K = \left(\frac{85.63}{P_{cb}}\right)^{2.71}$ (Chatzis, 1980)	946.5
Mendes (1997)	632 ~ 1393
This work	532.6
Nominal (CENPES/PETROBRAS, 1995)	500

It was found that the permeability of 95% of the samples could be 10 times underestimated to 25 times overestimated using the existing methods, such as correlative approaches proposed by Katz and Thompson (1986) (Ioannidis and Chatzis, 1993). The modeling methodology in the present work allows us to obtain the real network for the pore structure. The predicted results for two types of Berea sandstones show that the range of estimated permeability could be about 50 ~ 200%. As secondary flows associated to flow deviations inside complex porous structures appears to not significantly contribute to the main flow resistance when the Reynolds number is very low. The present method appears to be very suitable and easier to use when compared with methods based on numerical solutions of Stokes equation, giving the full velocity field. In addition, it does not suffer from the well known limitations of methods based on percolation networks. In fact, the skeleton is constructed trying to preserve the fine details of the pore structure along the flow path and can thus better describe its influence on main flow. Although the results are encouraging, more other samples should be studied in future.

7. CONCLUSIONS

7.1. CONCLUSIONS

Computer generation and application of reconstructed 3-D porous structure are studied in this work. Reconstructed porous medium and its skeleton are used to characterize the 3-D pore structure and predict the permeability of porous rocks. At first, the 2-D plane section image of the sample is acquired and segmented by image analysis techniques to obtain a binary representation, which is pore and solid phase. The porosity and autocorrelation function of the binary image are calculated by using fast Fourier transform. Then a 3-D porous structure is generated, which possesses the same porosity and autocorrelation function as the real sample in study. A truncated Gaussian method by using Fourier transform is proposed in this work. After the reconstructed porous medium is generated, the graph of 3-D pore space (skeleton) can be obtained by using a thinning algorithm, which preserves connectivity. Using the graph of 3-D pore space, the main flow path for a single flow can be obtained and classified into nodes and links. The local cross-sectional area and perimeter normal to the flow path in every point of each link is recorded to compute the local hydraulic radius. Resistance to flow is calculated for each link. A fluid pressure is calculated at each node, and total volumetric flux through the network is computed. Then the absolute permeability can be predicted from the corresponding network for any samples.

Fast Fourier transform is an efficient tool to characterize 2-D images of the porous media and reconstruct 3-D porous structure. By using fast Fourier transform, the porosity and autocorrelation function of a binary image of the sample are calculated. The fluctuations due to periodicity in 1-D autocorrelation function are drastically reduced.

A truncated Gaussian method based on Fourier transforms is proposed to generate 3-D pore structure from 2-D image of the sample. It improves the previous JQA method. The Gaussian field $Y(\mathbf{x})$ is generated directly from its autocorrelation function, which is truncated

to generate the phase function $Z(\mathbf{x})$. The porosity and autocorrelation function of the reconstructed porous structure agree with measured values of the real sample.

The advantage of the new reconstruction method is that it does not need the linear filter and avoids solving a complicated set of nonlinear equations. Using the fast Fourier transform makes this algorithm more efficient. Both processing time and computer memory requirements are improved. Phase angle distribution is taken at random since it does not affect the autocorrelation function. Therefore, different phase angle distributions generate similar patterns of the pore structure.

After the reconstructed porous medium is generated, the skeleton of 3-D pore structure is extracted by a thinning algorithm, which preserves connectivity. That is, it has the same topology as the pore space. The skeleton gives the real network for 3-D porous medium. As secondary flows associated to flow deviations inside complex porous structures appears to not significantly contribute to the main flow resistance when the Reynolds number is very low. In fact, the skeleton is constructed trying to preserve the fine details of the pore structure along the flow path and can thus better describe its influence on main flow. This technique can be used to the reconstructed or real porous media. The main flow path for a single flow is obtained, which is classified into nodes and links. The local hydraulic radius normal to the flow path in each link can be recorded to predict the absolute permeability.

The simulation of permeability is directly on the skeleton network of pore space. The linear equations are resolved by using successive over-relaxation. If magnification factor n is not large, its effect on the result is not important. The effect of sample size L is important as it is directly associated to statistical homogeneity of the reconstructed structure. The estimated permeability tends to converge when the ratio of L and maximum pore diameter is large enough. The results show that the permeability not only depends on porosity, but also on the correlation of the porous structure. Even if the porosity is about same or smaller, larger correlation length of porous structure can also result in the increase of permeability.

The estimated value for the permeability related to Fontainebleau sandstone agrees favorably with experimental value when compared with Adler's results. Values of predicted permeability for 200 mD and 500mD Berea sandstone samples are also in very good agreement with experimental results and with the empirical correlation of Dullien.

7.2. FUTURE WORKS

There are a few possible areas for future research: application of skeleton method to more samples and other reconstruction models, prediction of other transport properties and simulation of flow in reconstructed porous media by cellular automata or lattice gas.

Daian (1992; 1994) proposed multi-scale model to construct porous structure. At each scale, pores are randomly distributed according to their volume fraction obtained from the pore size distribution. Fernandes (1994) and Fernandes *et al.* (1996) improved the multi-scale geometrical reconstruction of porous structure to simulate intrusion process. Fractal or multi-fractal models have been used to heterogeneous porous media because the real porous media are often heterogeneous. Some macroscopic properties such as porosity are considered to obey fractal statistics. Markov random field (MRF) theory provides a convenient and consistent way of modeling context dependent entities such as image pixels and other spatially correlated features. This is achieved through characterizing mutual influences among such entities using MRF probabilities. Application of MRF theory to reconstruction of porous media was not found in the literatures. The results obtained by these models, especially characteristics of 3-D pore structure such as connectivity function, should be compared.

Once 3-D discrete porous media are generated, other transport properties, such as formation factor and relative permeability can be calculated by solving the transport equations. A new method for simulating flow based on cellular automata or lattice gas is available to mention (Sahimi, 1993). The idea is to numerically solve the Navier-Stokes equations in a realistic microscopically disordered geometry, and then study how volume-averaged properties of the flow relate to microscopic details of the geometry (Ferréol and Rothman, 1995).

APPENDIX

A. ALGORITHM FOR COMPUTING THE MIXED RADIX FFT

The fast Fourier transform (FFT) algorithm is an efficient method for computing the transformation Eq. (2.2). A nice split-radix, n -dimensional, fast Fourier transform by Singleton (1969), which has been converted into C code (Beale, 1997) was used in the present work. It is shown that this code is significantly faster than the routine used by Press *et al.* (1986) (25 vs. 36 seconds for a 1024×1024 floating point matrix).

The basic idea of fast Fourier transform is factoring N

$$N = \prod_{i=1}^m N_i \quad (\text{A.1})$$

and then decomposing the transform into m steps with N/N_i transformations of size N_i within each step. The complex Fourier transform can be expressed as a matrix multiplication

$$F = Tf \quad (\text{A.2})$$

Where T is an $N \times N$ matrix of complex exponentials

$$T_{jk} = \exp(i2\pi jk/N). \quad (\text{A.3})$$

In computing the fast Fourier transform, T is factored as

$$T = PF_m F_{m-1} \dots F_2 F_1, \quad (\text{A.4})$$

Where F_i is the transform step corresponding to the factor N_i of N and P is a permutation matrix. The matrices F_i can be further factored to yield

$$F_i = R_i T_i \quad (\text{A.5})$$

Where R_i is a diagonal matrix of rotation factor and T_i can be partitioned into N/N_i identical square submatrices.

Consider the complex transform of dimension p

$$F_r(u) + iF_i(u) = \sum_{j=0}^{p-1} \{f_x(j) + if_y(j)\} \left\{ \cos\left(\frac{2\pi ju}{p}\right) + i \sin\left(\frac{2\pi ju}{p}\right) \right\}$$

$$\begin{aligned}
&= f_x(0) + \sum_{j=1}^{p-1} \left\{ f_x(j) \cos\left(\frac{2\pi ju}{p}\right) - \sum_{j=1}^{p-1} f_y(j) \right\} \sin\left(\frac{2\pi ju}{p}\right) + \\
&\quad + i \left\{ f_y(0) + \sum_{j=1}^{p-1} f_y(j) \cos\left(\frac{2\pi ju}{p}\right) + \sum_{j=1}^{p-1} f_x(j) \sin\left(\frac{2\pi ju}{p}\right) \right\} \\
&= f_x(0) + \sum_{j=1}^{(p-1)/2} \left\{ f_x(j) + f_x(p-j) \right\} \cos\left(\frac{2\pi ju}{p}\right) - \sum_{j=1}^{(p-1)/2} \left\{ f_y(j) - f_y(p-j) \right\} \sin\left(\frac{2\pi ju}{p}\right) + \\
&\quad + i \left\{ f_y(0) + \sum_{j=1}^{(p-1)/2} \left\{ f_y(j) + f_y(p-j) \right\} \cos\left(\frac{2\pi ju}{p}\right) + \sum_{j=1}^{(p-1)/2} \left\{ f_x(j) - f_x(p-j) \right\} \sin\left(\frac{2\pi ju}{p}\right) \right\}
\end{aligned} \tag{A.6}$$

for $u=0, 1, 2, \dots, p-1$. We note first that

$$F_r(0) + iF_i(0) = \sum_{j=0}^{N-1} \{f_x(j) + if_y(j)\} \tag{A.7}$$

is computed without multiplications. For $u > 0$, altogether there are $2(p-1)$ series to sum, each with $(p-1)/2$ multiplications, for a total of $(p-1)^2$ real multiplications.

The total number of complex multiplications is

$$mN(p-1)(p+3)/4p-(N-1) \tag{A.8}$$

for a radix- p transform of $N=p^m$ complex data values, where p is an odd prime.

The details about algorithm were given by (Singleton, 1969).

B. 3-D GEOMETRY AND TRANSFORMATIONS

B.1. 3-D GEOMETRY

We will adopt the right-handed coordinate system in 3-D model, as shown in Figure B.1. A line passing through the two points (x_1, y_1, z_1) and (x_2, y_2, z_2) in three dimensions is expressed in terms of a parameter t :

$$\begin{aligned}x &= (x_2 - x_1)t + x_1 \\y &= (y_2 - y_1)t + y_1 \\z &= (z_2 - z_1)t + z_1.\end{aligned}\tag{B.1}$$

One way of specifying a plane is by a single point (x_p, y_p, z_p) and the direction perpendicular to the plane. A vector perpendicular to a plane is called normal vector, which is denoted $[v_x, v_y, v_z]$. Then an equation for the plane is:

$$v_x(x - x_p) + v_y(y - y_p) + v_z(z - z_p) = 0.\tag{B.2}$$

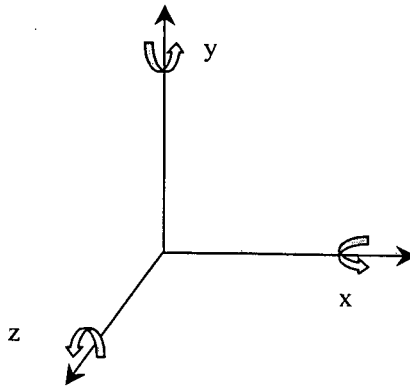


Figure B.1 - Right-handed coordinate system and positive rotations about the coordinate axes.

B.2. 3-D TRANSFORMATIONS

All transformations are expressed in a 3-D Cartesian coordinate system in which a point has coordinates denoted (x, y, z) . Suppose that we transform a point (x, y, z) to a new location (x^*, y^*, z^*) . We use the matrix representation as follows

$$\begin{bmatrix} x^* \\ y^* \\ z^* \\ 1 \end{bmatrix} = T \begin{bmatrix} x \\ y \\ z \\ 1 \end{bmatrix} \quad (\text{B.3})$$

where T is a 4×4 transformation matrix. Here we only introduce two transformations: rotation and reflection, which are used in thinning algorithm.

Rotations in 3-D are important in understanding the shape of an object or in verifying different angles of a model. Figure B.1 shows the three basic positive rotations about the coordinate axes. The coordinate system is right-handed and counterclockwise rotations are assumed positive when looking along the axis toward the origin. Table B.1 gives the summary of rotation matrices about the three coordination axes.

Table B.1 : Summary of rotation matrices about the three coordination axes.

Rotation operation	T
A rotation of θ degrees about x	$\begin{bmatrix} 1 & 0 & 0 & 0 \\ 0 & \cos\theta & \sin\theta & 0 \\ 0 & -\sin\theta & \cos\theta & 0 \\ 0 & 0 & 0 & 1 \end{bmatrix}$
A rotation of θ degrees about y	$\begin{bmatrix} \cos\theta & \sin\theta & 0 & 0 \\ -\sin\theta & \cos\theta & 0 & 0 \\ 0 & 0 & 1 & 0 \\ 0 & 0 & 0 & 1 \end{bmatrix}$
A rotation of θ degrees about z	$\begin{bmatrix} \cos\theta & 0 & -\sin\theta & 0 \\ 0 & 1 & 0 & 0 \\ \sin\theta & 0 & \cos\theta & 0 \\ 0 & 0 & 0 & 1 \end{bmatrix}$

Three-dimensional reflections (mirroring) are usually obtained by coordination transformations about specified reflection planes. Table B.2 shows the matrices that produce reflection about the planes $x=0$, $y=0$, $z=0$, and a central reflection about the origin.

Table B.2 : Reflection matrices.

Reflection operation	T
Plane x=0	$\begin{bmatrix} -1 & 0 & 0 & 0 \\ 0 & 1 & 0 & 0 \\ 0 & 0 & 1 & 0 \\ 0 & 0 & 0 & 1 \end{bmatrix}$
Plane y=0	$\begin{bmatrix} 1 & 0 & 0 & 0 \\ 0 & -1 & 0 & 0 \\ 0 & 0 & 1 & 0 \\ 0 & 0 & 0 & 1 \end{bmatrix}$
Plane z=0	$\begin{bmatrix} 1 & 0 & 0 & 0 \\ 0 & 1 & 0 & 0 \\ 0 & 0 & -1 & 0 \\ 0 & 0 & 0 & 1 \end{bmatrix}$
Point (0,0,0)	$\begin{bmatrix} -1 & 0 & 0 & 0 \\ 0 & -1 & 0 & 0 \\ 0 & 0 & -1 & 0 \\ 0 & 0 & 0 & 1 \end{bmatrix}$

B.3. THE TANGENT LINE AND NORMAL PLANE

We suppose arbitrary one link in the graph which has n points:

$$(x_1, y_1, z_1), (x_2, y_2, z_2), \dots \dots (x_n, y_n, z_n). \quad (\text{B.4})$$

There are many function forms which can be made to pass through sample points by adjusting parameters. Polynomial, trigonometric, exponential, etc., functions have been used. Here we use polynomial functions to approximate the curve. And the functions are expressed in the parametric form:

$$x = f_x(t) = \sum_{i=1}^n x_i B_i(t),$$

$$\begin{aligned}
 y = f_y(t) &= \sum_{i=1}^n y_i B_i(t), \\
 z = f_z(t) &= \sum_{i=1}^n z_i B_i(t).
 \end{aligned}
 \tag{B.5}$$

These functions $B_i(t)$ are called blending functions. For simplification, we use three points and Lagrange blending function. These give

$$\begin{aligned}
 B_1 &= \frac{t(t-1)(t-2)}{(-1)(-2)(-3)}, \\
 B_2 &= \frac{(t+1)(t-1)(t-2)}{(1)(-1)(-2)}, \\
 B_3 &= \frac{(t+1)t(t-2)}{(2)(1)(-1)}.
 \end{aligned}
 \tag{B.6}$$

Using these functions and three points, we can construct a curve which passes through the three sample points:

$$\begin{aligned}
 x &= x_1 B_1(t) + x_2 B_2(t) + x_3 B_3(t), \\
 y &= y_1 B_1(t) + y_2 B_2(t) + y_3 B_3(t), \\
 z &= z_1 B_1(t) + z_2 B_2(t) + z_3 B_3(t).
 \end{aligned}
 \tag{B.7}$$

and $t = -1, 0, 1$. Because the direction of tangent line of any function is the derivation of the function, the equations of tangent line and normal plane through the point (x_0, y_0, z_0) can be expressed respectively:

$$\frac{x - x_0}{\frac{dx}{dt} \Big|_{t=t_0}} = \frac{y - y_0}{\frac{dy}{dt} \Big|_{t=t_0}} = \frac{z - z_0}{\frac{dz}{dt} \Big|_{t=t_0}},
 \tag{B.8}$$

and

$$\frac{dx}{dt} \Big|_{t=t_0} (x - x_0) + \frac{dy}{dt} \Big|_{t=t_0} (y - y_0) + \frac{dz}{dt} \Big|_{t=t_0} (z - z_0) = 0.
 \tag{B.9}$$

Once the normal plane is determined, the pore space which cross this plane can obtained. The area of the region connected the point (x_0, y_0, z_0) is the total pixel numbers inside the region and the perimeter is the boundary pixel numbers.

C. PROCEDURES FROM 2-D IMAGES TO PREDICTION OF PERMEABILITY

All programs were written in C/C++, in which the processing image was carried out in Window system and the others in UNIX system. The procedures of all processes from 2-D images to prediction of permeability are described as follows.

C.1. CALCULATION OF POROSITY AND CORRELATION FUNCTION FROM 2-D IMAGES

Input: 2-D binary image with pore (1) and solid (0).

Output: porosity and autocorrelation function.

Procedure: see Figure C.1.

C.2. RECONSTRUCTION OF 3-D PORE STRUCTURE

Input: amplification factor n , size N_x, N_y, N_z , porosity and autocorrelation function.

Output: 3-D binary image with pore (1) and solid (0) $Z(i,j,k)$

Procedure: see Figure C.2.

C.3. SKELETONIZATION

Input: 3-D binary image with pore (1) and solid (0) $Z(i,j,k)$, size N_x, N_y, N_z .

Output: 3-D binary image with skeleton (1) and others (0) $Skeleton(i,j,k)$.

Procedure: Figure C.3.

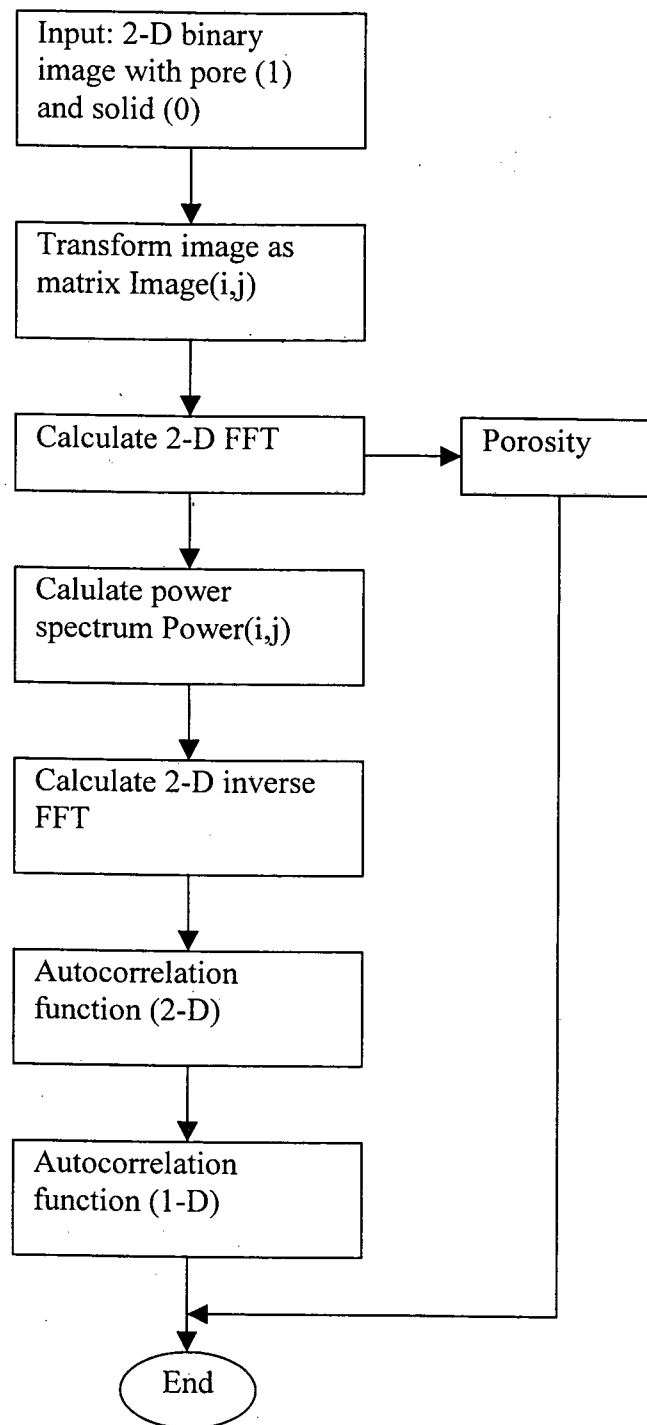


Figure C.1 Procedure of calculating of porosity and autocorrelation function from 2-D images.

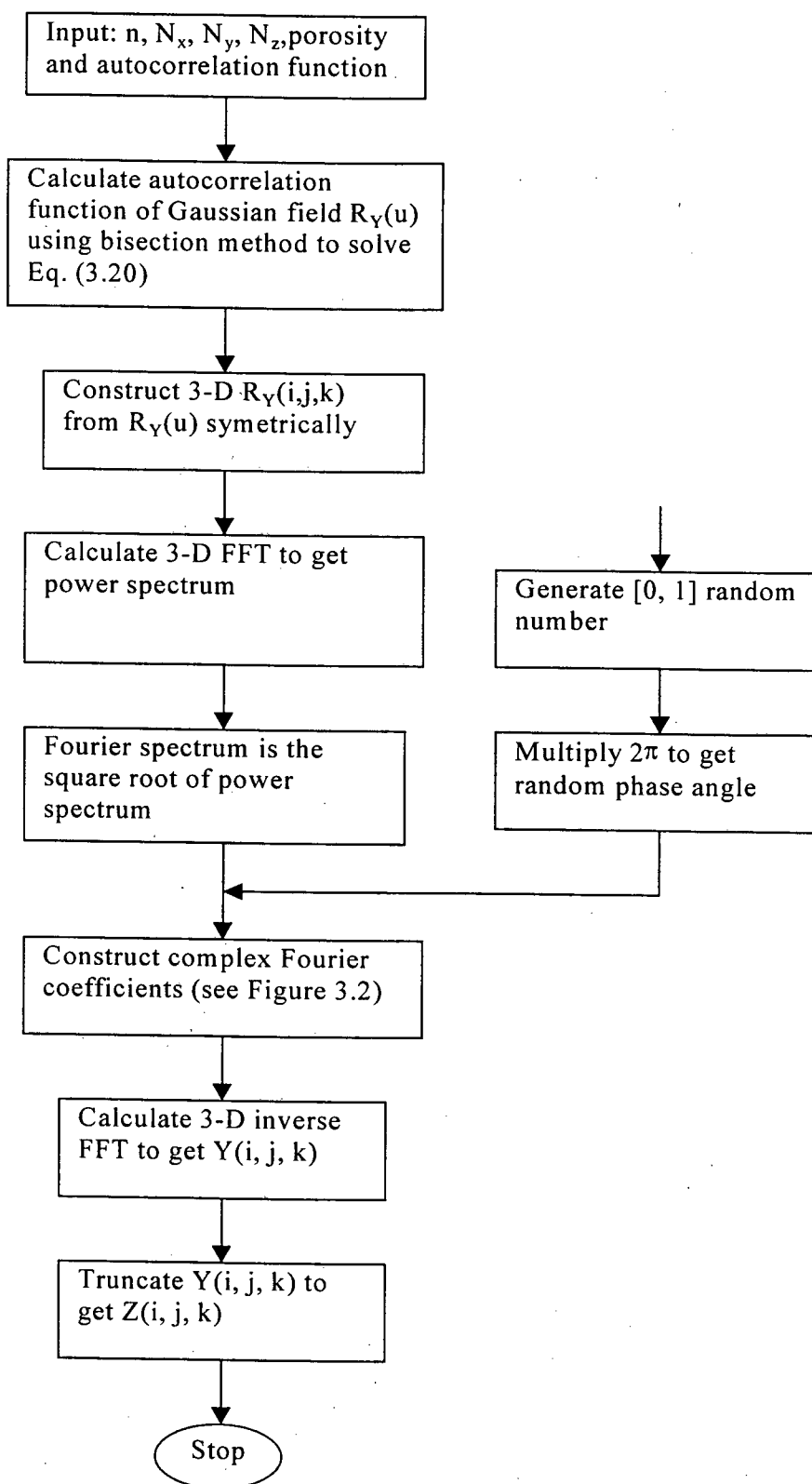


Figure C.2 Procedure of reconstruction of 3-D pore structure.

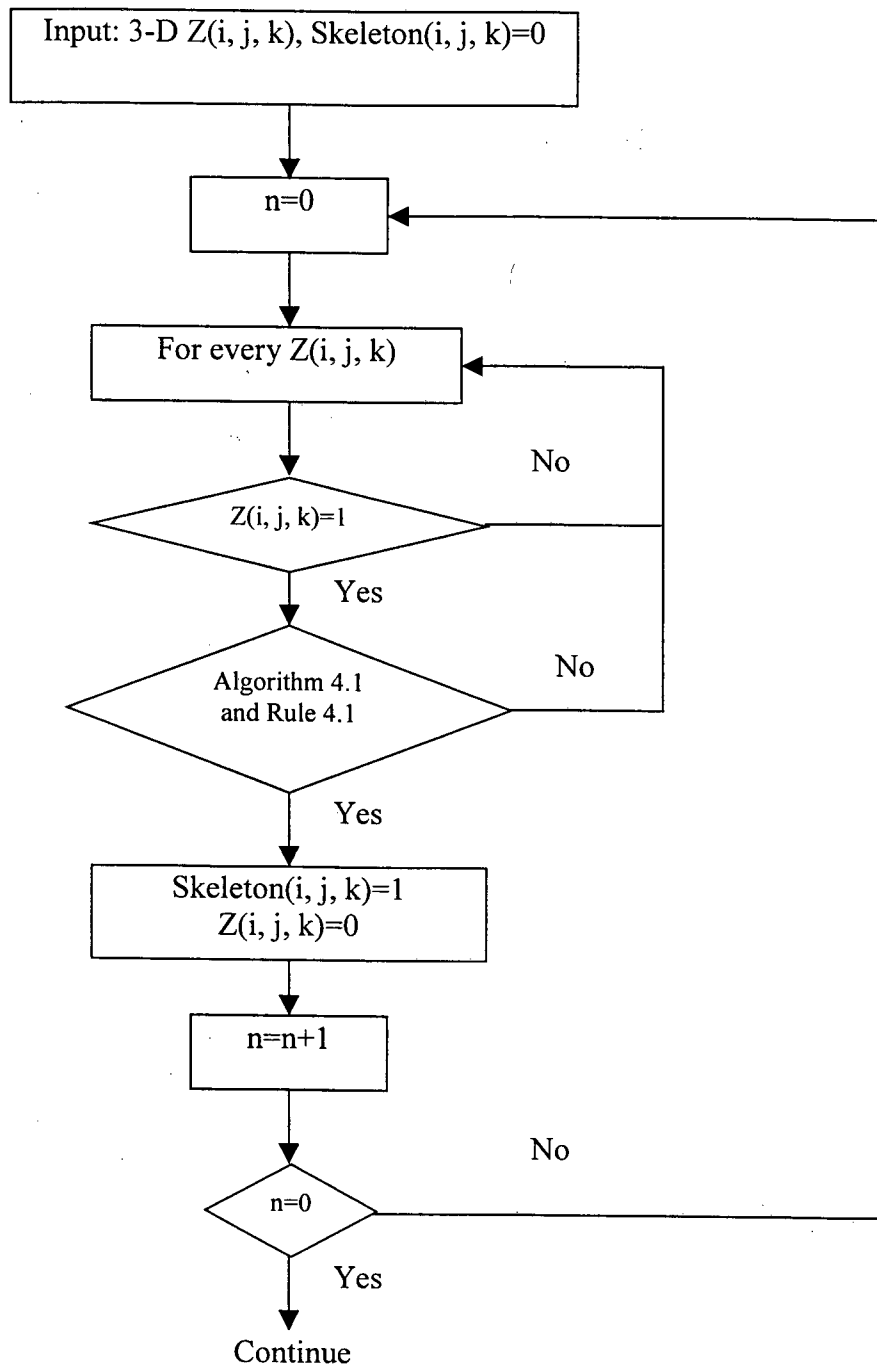


Figure C.3 Procedure of skeletonization.

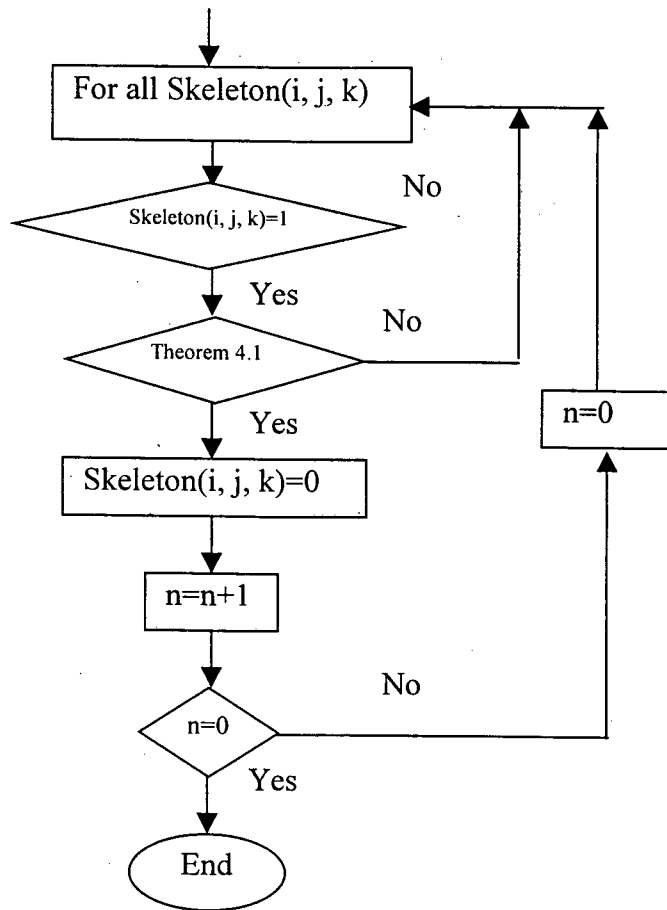


Figure C.3 (continued).

C.4. CLASSIFICATION

Input: 3-D binary image matrix with pore (1) and solid (0) and corresponding skeleton matrix with skeleton (1) and others (0), viscosity of fluid μ , length of each pixel α .

Output: the graph with nodes and links, and conductance of every link.

Procedure: see Figure C.4.

C.5. CALCULATION OF PERMEABILITY

Input: the graph with nodes and links, conductance of every link, relaxation factor β and error ϵ .

Output: permeability.

Procedure: see Figure C.5.

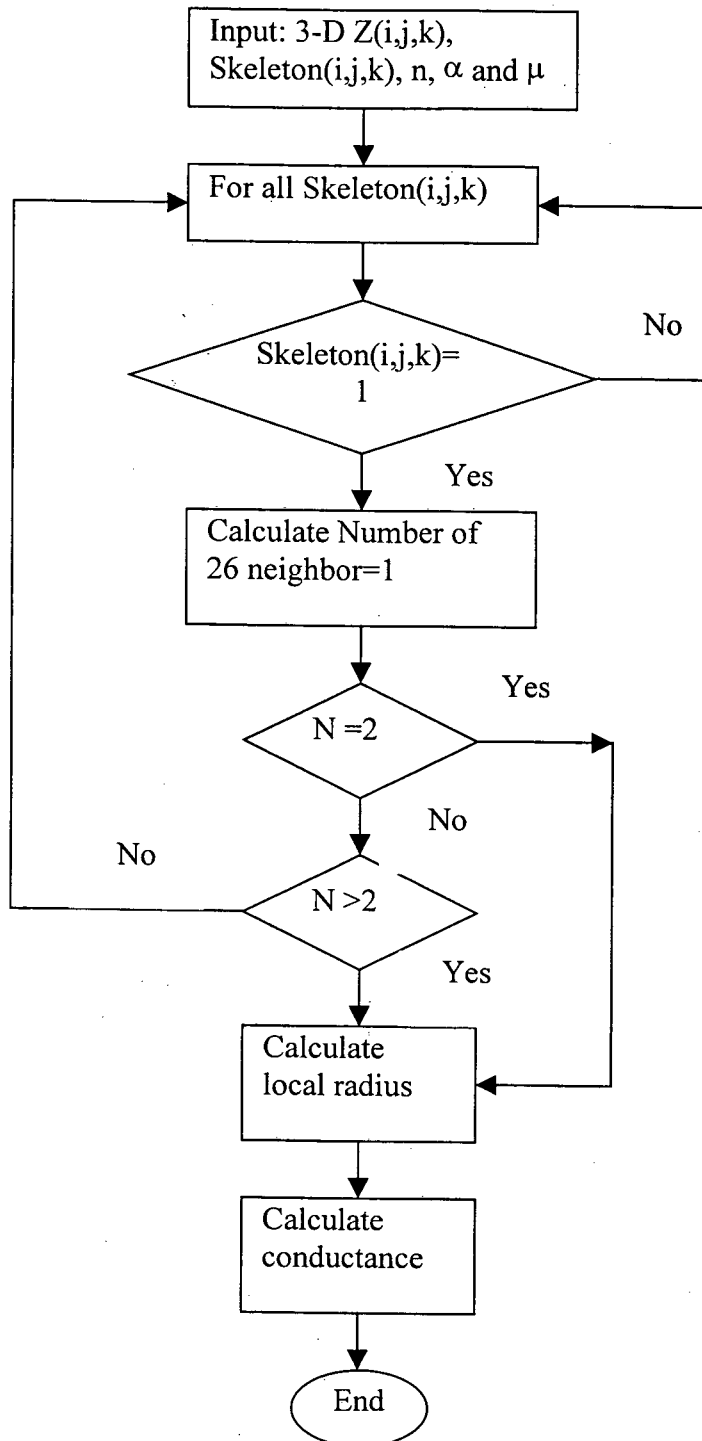


Figure C.4 Procedure of classification of skeleton.

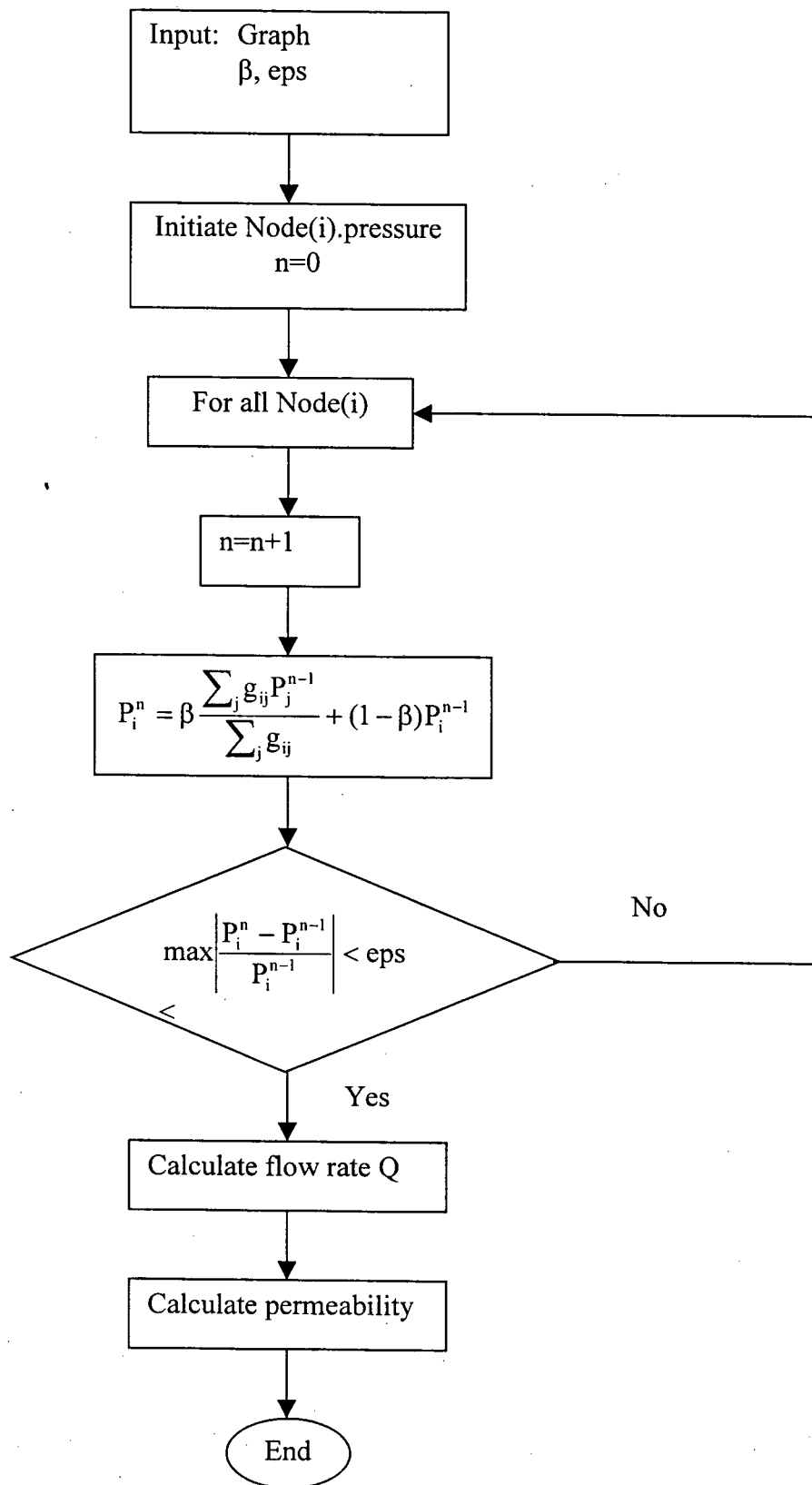


Figure C.5 Procedure of predicting permeability.

REFERENCES

- ADLER, P.M. *Porous Media: Geometry and Transports*, Butterworth-Heinemann, New York, 1992.
- ADLER, P.M., JACQUIN, C.G. AND QUIBLIER, J.A. Flow in simulated porous media, *Int. J. Multiphase Flow*, vol.16, pp.691-712, 1990.
- BAKKE, S. AND ØREN, P.E. 3-D Pore-scale modeling of heterogeneous sandstone reservoir rocks and quantitative analysis of the architecture, geometry and spatial continuity of the pore network, Paper *SPE 35479* presented at the European 3-D Reservoir Modeling Conference, Stavanger, Norway, 1996.
- BEALE, J. <http://www.best.com/~beale/gforge/fft-n.tar.gz>, June 20, 1997.
- BENTZ, D.P. AND MARTYS, N.S. Hydraulic radius and transport in reconstructed model three-dimensional porous media, *Transport in Porous Media*, vol.17, pp.221-238, 1994.
- BERRYMAN, J.G. AND BLAIR, S.C. Use of digital image analysis to estimate fluid permeability of porous materials: application of two-point correlation functions, *J. Appl. Phys.*, vol.60, pp.1930-1938, 1986.
- CENPES/PETROBRÁS, Materials on the images of Berea sandstone and mercury intrusion curves, *Internal Report*, 1995.
- CHATZIS, I. *A Network Approach to Analyse and Model Capillary and Transport Phenomena in Porous Media*, Ph.D. Thesis, University of Waterloo, Ontario, Canada, 1980.

- CHRISTOFIDES, N. *Graph Theory: An Algorithm Approach*, Academic Press, London, New York and San Francisco, 1975.
- DAGAN, Z., WEINBAUM, S. AND PFEFFER, R. An infinite-series solution for the creeping motion through an orifice of finite length, *J. Fluid Mech.*, vol.115, pp.505-523, 1982.
- DAIAN, J.F. in *IDS'92. 8th Int. Drying Symp.* Montreal, 1992.
- DAIAN, J.F., XU, K. AND QUENARD, D. in *Characterization of Porous Solids III*, edited by Rouquerol J F., Rodriguez-Peinoso and K.S.W., New York, 1994
- DULLIEN, F.A.L. *Porous Media - Fluid Transport and Pore Structure*, Academic Press, San Diego, 1992.
- FERNANDES, C.P. *Caracterização Morfotológica de Espaços Porosos: Reconstituição Multiescala e Simulação de Processos de Invasão de Fluidos Não-Molhantes*, Ph. D. thesis, Federal University of Santa Catarina, Florianópolis, Brazil, 1994.
- FERNANDES, C.P., LIANG, Z.R., MAGNANI, F.S. AND PHILIPPI, P.C. Mathematical modeling of porous structures: reconstruction process with Gaussian truncated and multiscale system, *Anais do I Simposio Nacional de Instrumentacao Agropecuaria-I SIAGRO*, pp.233-239, Brasília, 1997.
- FERNANDES, C.P., MAGNANI, F.S., PHILIPPI, P.C. AND DAÏNA, J.F. Multiscale geometrical reconstruction of porous structures, *Physical Review E*, vol.54, pp.1434-1442, 1996.
- FERRÉROL, B. AND ROTHMAN, D.H. Lattice-Boltzmann simulations of flow through fontainebleau sandstone, *Transport in Porous Media*, vol.20, pp.3-20, 1995.
- GONZALEZ, R.C. AND WOODS, R.E. *Digital Image Processing*, Addison-Wesley Publishing Company, 1992.
- HAZLETT, R.D. Simulation of capillary-dominated displacements in microtomographic images of reservoir rocks, *Transport in Porous Media*, vol.20, pp.21-35, 1995.

- HILFER, R. Transport and relaxation phenomena in porous media, *Adv. Chem. Phys.*, vol.92, pp.299, 1996.
- HOSHEN, J. AND KOPELMAN, R. Percolation and cluster distribution. I. cluster multiple labeling technique and critical concentration algorithm. *Physical Review B*. vol.14, pp.3438-3445, 1976.
- IOANNIDIS, M.A. AND CHATZIS, I. Network modeling of pore structure and transport properties of porous media, *Chem. Eng. Sci.*, vol.48, pp.951-972, 1993.
- IOANNIDIS, M.A., KWIECIEN, M.J. AND CHATZIS, I. Computer generation and application of 3-D model porous media: from pore-level geostatistics to the estimation of formation factor, Paper *SPE 30201* presented at the Petroleum Computer Conference, Houston, TX, 1995.
- IOANNIDIS, M.A., KWIECIEN, M.J. AND CHATZIS, I. Statistical analysis of the porous microstructure as a method for estimating reservoir permeability, *J. Pet. Sci. Eng.*, vol.16, pp.251-261, 1996.
- JOSHI, M.Y. *A Class of Stochastic Models for Porous Media*, Ph D thesis, University of Kansas, USA, 1974.
- KAZ, A.J. AND TOMPSON, A.H. Quantitative prediction of permeability in porous rock, *Physical Review B*, vol. 34, pp. 8179-8181, 1986.
- KOPLIK, J. Creeping flow in two-dimensional networks, *J. Fluid Mech.*, vol.119, pp.219-247, 1982.
- KOPLIK, J. Addendum: Creeping flow in two-dimensional networks, *J. Fluid Mech.*, vol. 130, pp. 468-469, 1983.
- KOPLIK, J., LIN, C. AND VERMETTE, M. Conductivity and permeability from microgeometry, *J. Appl. Phys.*, vol.56, pp.3127-3131, 1984.
- KWIECIEN, M.J., MACDONALD, I.F. AND DULLIEN, F.A.L. Three-dimensional reconstruction of porous media from serial section data, *Journal of Microscopy*, vol.159, pp.343-349, 1990.

- LANTUÉJOL, CH. Ergodicity and integral range, *Journal of Microscopy*, vol.161, pp.387-404, 1991.
- LIN, C. AND COHEN, M.H. Quantitative methods for microgeometric modeling, *J. Appl. Phys.*, vol.53, pp.4152-4165, 1982.
- MA, C.M. A 3D fully parallel thinning algorithm for generating medical faces, *Patt. Recog. Lett.*, vol.16, pp.83-87, 1995.
- MA, C.M. On topology preservation in 3D thinning, *CVGIP: Image Understanding*, vol.59, pp.328-339, 1994.
- MAGNANI, F.S. *Determinação das Configurações de Equilíbrio em Meios Porosos Indeformáveis*, Ph. D. thesis, Federal University of Santa Catarina, Florianópolis, Brazil, 1996.
- MALISKA JÚNIOR, C.R. *Coi-LibTM, Classes & Objects for Interfacing-Programming Manual*, version 1.0, 1996.
- MARTYS, N.S. AND. GARBOCZI, E.J. Length scales relating the fluid permeability and electrical conductivity in random two-dimensional model porous media, *Physical Review B*, vol.46, pp.6080-6090, 1992.
- MENDES, N. *Modelos para Previsão da Transferência de Calor e de Umidade em Elementos Porosos de Edificações*, Ph. D. thesis, Federal University of Santa Catarina, Florianópolis, Brazil, 1997.
- PAPOULIS, A. *Probability, Random Variables, and Stochastic Processes*, McGraw-Hill, Inc., New York, 1965.
- PARDO-IGÚZQUIZA, E. AND CHICA-OLMO, M. The Fourier integral method: an efficient spectral method for simulation of random fields, *Mathematical Geology*, vol.25, pp.177-217, 1993.

- PHILIPPI, P.C AND FERNANDES, C.P. Segmentation of colored images of reservoir rocks, *Internal Technical Report*, Federal University of Santa Catarina, Florianópolis, Brazil, 1995.
- PHILIPPI, P.C. AND SOUZA, H.A. Modeling moisture distribution and isothermal transfer in a heterogeneous porous material, *Int. J. Multiphase Flow*, vol.21, pp.667-691, 1995.
- PHILIPPI P.C., YUNES, P.R., FERNANDES, C.P. AND MAGNANI, F.S. The microstructure of porous building materials: study of a cement and lime mortar, *Transport in Porous Media*, vol.14, pp.219-245, 1994.
- PIERITZ, R.A. *Desevolvimento das Técnicas do Gráfico da Linha Mediana e da Binarização por Regiões Conexas Aplicadas à Caracterização Geométrica de Meios Porosos*, MS thesis, Federal University of Santa Catarina, Florianópolis, Brazil, 1994.
- PRESS, W.H., FLANNERY, B.P., TEUKOLSKY, S.A. AND VETTERLING, W.T. *Numerical Recipes – The Art of Scientific Computing*, University of Cambridge Press, Cambridge, pp.818, 1986.
- PRINCE, C.M. AND EHRLICH, R. Analysis of spatial order in sandstones I. basic principles, *Mathematical Geology*, vol.22, pp.333-359, 1990.
- QUENARD, D.A., BENTZ, D.P. AND GARBOCZI, E.J. Capillary condensation, hysteresis, and image analysis, *Drying '92*, pp.253-262, 1992.
- QUIBLIER, J.A. A new three-dimensional modeling technique for studying porous media, *Journal of Colloid and Interface Science*, vol.98, pp.84-102, 1984.
- RESEARCH SYSTEM, INC. *Using IDL Insight*, 1997.
- SAHIMI, M. Flow phenomena in rocks: from continuum models to fractals, percolation, cellular automata, and simulating annealing, *Reviews of Modern Physics*, vol.65, pp.1393-1534, 1993.
- SANNITI DI BAJA, G. Well-shaped, stable, and reversible skeletons from the (3,4)-distance transform, *J. of Visual Communication and Image Representation*, vol.5, pp.107-115, 1994.

- SERRA, J. *Image Analysis and Mathematical Morphology*, Academic Press, New York, 1982.
- SINGLETON, R.C. An algorithm for computing the mixed radix fast Fourier transform, *IEEE Transactions on Audio and Electroacoustics*, vol.AU-17, pp.93-103, 1969.
- THOVERT, J.F., SALLES, J. AND ADLER, P.M. Computerized characterization of the geometry of real porous media: their discretization, analysis and interpretation, *Journal of Microscopy*, vol.170, pp.65-79, 1993.
- XU, K. *Structures Multiechelles: Modeles Pour La Description des Materiaux Poreux et L'estimation de Leurs Proprietes de Transport*, Ph.D. thesis, L'Universite Joseph Fourier, Grenoble, France, 1995.
- YAO, J., FRYKMAN, P., KALAYDJIAN, F., THOVERT, J.F. AND ADLER, P.M. High-order moments of the phase function for real and reconstructed model porous media: a comparison, *Journal of Colloid and Interface Science*, vol.156, pp.478-490, 1993.
- ZHANG, T.Y. AND SUEN, C.Y. A fast parallel algorithm for thinning digital patterns, *Comm. ACM*, vol.27, pp.236-239, 1984.